Laser Ultrasonic Method for Determination of Crystallographic Orientation of Large Grain Metals by Spatially Resolved Acoustic Spectroscopy (SRAS)

by Wenqi Li, Bsc, Msc

Thesis submitted to The University of Nottingham
for the degree of Doctor of Philosophy, July 2012

The University of Nottingham

UNITED KINGDOM · CHINA · MALAYSIA

Abstract

This thesis presents a crystallographic orientation determination technique which is based on a laser ultrasonic method: spatially resolved acoustic spectroscopy (SRAS). Surface acoustic waves (SAW) propagate on a solid surface with a phase velocity that is frequency independent, but which varies with the crystallographic orientation. By comparing the SRAS results with the calculated SAW velocities, the orientation of crystal can be determined.

The SRAS technique allow the SAW velocity to be recorded in two slightly different approaches. According to the formula $v = \lambda f$, the velocity v can be obtained by varying the k-vector (λ) or frequency f of the wave while the another multiplier is fixed. K-SRAS is implemented by firing a laser beam with a fixed intensity modulation frequency through a spatial light modulator (SLM); the SAW velocity is determined by varying the fringe spacing of the SLM image. F-SRAS uses a broadband (sharp pulse) laser, the beam passes through a chrome photomask with fixed fringe spacing, and the peak frequency is used to determine the SAW velocity. Scans are performed on single or multiple-grain titanium alloy, aluminium and nickel samples by both methods. The contrast of the velocity maps give adequate information of grain size and location.

A SAW velocity model is developed according to the elastic constants and mass density of the material. The orientation of crystals can be determined by comparing the SRAS results and the SAW velocity model. The SAW velocities in different propagation directions are measured on nickel, aluminium and titanium α samples with known orientations, and agree well with the predicted velocities from the model. An overlap function is introduced as a search algorithm to link the SRAS results to the SAW velocity model. The results are compared with measurements taken using the Laue back-reflection technique; they gave very close crystallographic orientation with acceptable error within the industrial limit.

At the end of the thesis, consideration is given to further research in the acoustic modelling and data processing algorithms that would improve the technique in the future.

Acknowledgements

I'd like to give a great thank you to Steve Sharples and Matt Clark, my supervisors. During the last four years, I learnt from Steve every single day at work, not only with professional knowledge and research methods, but also from his rigorous approach and attitude to science. He was always there and gave me help whenever I needed with endless patience, and always guided me towards the right way to solve problems. Matt, who offered me the chance to work in the field, supplied valuable ideas and inspiration constantly, with encouragement and great supervision. I feel very lucky in having the opportunity to be supervised by them.

I am grateful to Professor Mike Somekh, who gave me precious advice and suggestions for my PhD and thesis. And also a huge thank you to my colleagues Robert, Richard, Teti, Ahmet and Xuesheng, especially Robert for providing a lot of help for my work.

Thanks to my friends Tal, Kris, Yut and Gary, for sharing experience and responsibility, supporting me through all these years to finish my study in a foreign country. Special thanks to Tal for helping me with my writing and giving me her support at anytime.

I would like to thank Colin with all my heart, for everything he did for me, big and small.

At last I would like to thank my parents, the people who unconditionally support me financially and mentally, so I could work towards my target without concern.

Contents

Chapter 1

Introduction

This thesis presents the technique Spatial Resolved Acoustic Spectroscopy (SRAS), which uses laser generated and detected Surface Acoustic Waves (SAWs) to image the microstructure of materials, for instance titanium, aluminium, nickel and silicon. It is a rapid, non-contact and non-destructive method. The measured SAW phase velocity over the sample surface gives the contrast of grains, and reveals the microstructure of materials and crystallographic orientations, which are significant metrics of material characterisation.

The initial development of the technique and system occurred in earlier years, researched by Steve Sharples and Matt Clark [1]. Recent years' work, presented in this thesis, covers the development of fast SRAS systems, modelling of SAW phase velocity, and orientation determination by SRAS results. Two welled developed techniques are compared against the SRAS technique. SRAS has great potential as a complimentary technique alongside exciting methods, and in some cases to replace current techniques entirely.

1.1   Overview of Thesis

The central contribution of this thesis is orientation determination of crystals based on SRAS imaging. Figure 1.1 illustrates the four main themes of the thesis, along

with the relevant chapters. Two approaches of SRAS are illustrated with experimental results of titanium, aluminium and nickel samples presented. A SAWs velocity model of several materials is computed according to the wave equation and boundary conditions. The overlap function is introduced as a search algorithm to interpret the SRAS results and to indicate crystallographic orientations. Finally, in order to test the performance, SRAS results of single crystal nickel are compared with an X-ray diffraction (XRD) Laue back-reflection (LBR) method. Moreover, SRAS images of multigrain nickel and titanium α samples are obtained; parts of the results are compared with Electron Backscattered Diffraction (EBSD). Assessment of the search algorithm is made based on the nickel single crystal results.
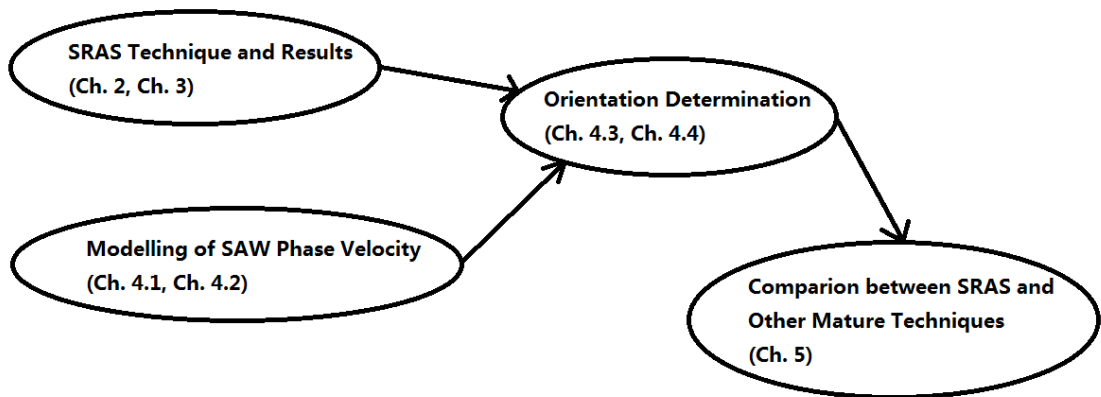
Figure 1.1: Four topics of this thesis with relevant chapters.

A brief description of each chapter is as follows:

- Chapter 1 introduces the background knowledge of the SRAS technique and crystallographic orientation, including the concept of SAWs, laser ultrasonics, crystal structure and two of the existing crystallographic orientation techniques.

- Chapter 2 explains the theory, system construction and sources of error for two approaches using the SRAS technique.

- Chapter 3 illustrates the test results obtained by two SRAS techniques; the imaging ability of these two techniques are presented.

- Chapter 4 describes the foundation of SAWs behaviour and properties. The procedure of modelling of several materials (aluminium, nickel, titanium α and β phase) are shown. A search algorithm is introduced to link the SRAS results with crystal orientations.

- Chapter 5 illustrates the orientation determination results by SRAS, and compares this with two of the mature techniques (XRD-LBR and EBSD). System reliability is investigated.

- Chapter 6 provides a discussion around the considerations and problems of the current technique/system. It also discusses potential areas for future research.

- Chapter 7 summarises the work which has been presented in this thesis.

1.2 Ultrasonics

Since Galileo Galilei (1564–1642) tried to measure the sound frequency by scraping a chisel at different speeds, more and more scientists joined the exploration of acoustic waves. The hearing range of a human being is between 20Hz and 20,000Hz. Any acoustic wave with a frequency above this range is called ultrasound (discovered by Lazzaro Spallanzani in 1790). It was not until World War I that the ultrasonic application (sonar) was introduced for the first time. Sonar emits a series of ultrasound signals with different frequencies under water, and the reflected waves can provide information about distance, shape and state of motion of the target objects, for instance submarines.

An acoustic wave is generated by the particle vibration of a medium, in a gas, liquid or solid. It propagates in four principle modes which are distinguished by the

direction of the particle oscillation; they are transverse waves, longitudinal waves, plate waves and surface waves.

For transverse waves, particles oscillate in the direction which is perpendicular to the wave propagation direction. This causes shear stress when it propagates in elastic materials (i.e., all solids), hence it is know as a shear wave, or a Secondary Wave (S-wave) in seismology. In liquids the interaction stress between the molecules is too weak to transmit a shear force, thus transverse waves cannot propagate, except in the case of visco-elastic liquids. The wave velocity in isotropic media is given by [2]

$$v_t = \sqrt{\frac{E}{2\rho(1+\sigma)}} \tag{1.1}$$

where σ is the Poisson Ratio, ρ is the mass density of medium, E is the Young's Modulus.

If the particles oscillates in parallel to the propagation direction within a medium, it is called a longitudinal wave, which is known as a Primary Wave (P-wave) in seismology, or a compressional wave because the compression leads to the change in local particle density during wave propagation. Unlike transverse waves, longitudinal waves do not only exist in solids but also in gases and liquids. Their velocity in isotropic solids is given by [2]

$$v_l = \sqrt{\frac{E(1-\sigma)}{\rho(1+\sigma)(1-2\sigma)}} \tag{1.2}$$

where σ is the Poisson Ratio, ρ is the mass density of medium, E is the Young's Modulus.

Plate waves, as implied by the name, exist in the thin plate or layer with two parallel surfaces. A wave with an appropriate frequency incident to a plate or layer below a certain thickness, generates particle vibrations at both surfaces and internally within the plate.

SAWs and Pseudo-SAW (PSAW)

Surface waves were first introduced by Lord Rayleigh [3]. Rayleigh researched waves travelling along and parallel to the half-infinite surface of an isotropic medium. These waves contain at least two rapidly damped terms. The motion of particles during propagation follows an elliptical locus, and oscillates in the plane which contains the wave propagation direction and is perpendicular to the material surface, as seen in Figure 1.2. The amplitude of the wave decreases exponentially beneath the free surface, and the penetration depth roughly equals its wavelength. The velocity of the surface wave is slightly slower than the slowest transverse bulk wave; it is frequency independent and exists at any combination of plane and direction on crystals [4] [5].

A. E. H. Love identified another type of surface wave known as Love waves [6]; the displacement of particles oscillates in plane and perpendicular to the wave propagation direction. However the amplitudes do not attenuate with the penetration depth.
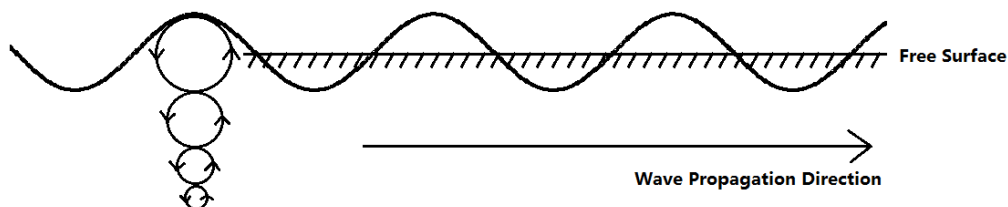
Figure 1.2: Surface wave.

A particular type of surface wave, which travels faster than the slowest transverse bulk wave, can be observed at some directions of certain planes. It is known as a 'Pseudo' Surface Acoustic Waves (PSAWs) or a 'Leaky' waves because it propagates towards the material in a small angle and carries the energy away from the surface. Two terms of the wave are involved; they share the properties as a Rayleigh wave and decay rapidly beneath the surface. There is a small third term which leads the wave tilts down slightly into the material. Because this term has a minor contribution, PSAW generally behaves like a normal SAW over a short

distance and can be detected.

A significant property of cubic crystals is the elastic anisotropy ratio, which is given as [7]

$$\eta = \frac{2C_{44}}{C_{11} - C_{12}} \qquad (1.3)$$

where C_{44}, C_{11} and C_{12} are elastic constants. On isotropic material has $\eta = 1$; any materials with $\eta > 1$ or $\eta < 1$ are anisotropic; the further away the η to 1, the stronger anisotropic the material is. The magnitude of the anisotropic ratio indicates the stiffness along the axis and across the axis, hence the SAW phase velocity of the materials is influenced. Farnell believed PSAW can be observed on plane (001) and (111) of the crystals which has $\eta > 1$, and plane (110) of crystals with $\eta < 1$ [4].

1.3 Non Destructive Testing (NDT)

NDT techniques are widely used to examine the quality of products without damaging the testing material in industrial inspection; in other words, the testing material can be used in the future. These are widely used techniques, especially if the test objects are expensive or are the only existing samples.

1.3.1 Background

The history of NDT goes back many decades. More than one hundred year ago, before Professor Wilhelm Conrad Roentgen (1845-1923) discovered X-rays, people only used oil and powder to inspect the defects on testing materials surfaces (this was a predecessor of penetrate testing which will be mentioned later). Roentgen changed this situation by producing the first industrial radiograph in the world. After World War II, other inspection techniques such as ultrasonic and eddy current testing began to be developed rapidly. The purpose of NDT technology has changed over time, from the basic defect inspection to designing devices that have no defects

over thresholds levels that would cause failure during their useful life.

With the development of the discipline of fracture mechanics in the 1970s, NDT techniques were not only used to detect whether there were defects but also to indicate the size of any flaws. The knowledge of fracture mechanics enables predictions of the growth of cracks under cyclic loading to be calculated, to establish how long a device with a defect can be used.

Typically, NDT techniques are not only locating the defects, but also could indicate some features about defects such as shape, size and orientation.

Now NDT techniques are used as a significant method of inspection in lots of fields including industrial automation, civil engineering, the aerospace industry and the medicinal industry (where the testing objects are nonliving organs).

1.3.2 NDT Techniques

There are a number of NDT methods that are utilised in industry. The most popular methods are:

- Visual Inspection

  Visual inspection involves either examining by eye directly, or the examiner using special tools to get a closer look at the testing object (e.g. magnifying glasses, mirrors, or borescopes). This method is only suitable for the transparent or translucent device, or the one which only have defects on the materials' surface. This is the simplest and cheapest method. However, it is not useful if the cracks are too small to be seen using the human eyes.

- Penetrate Testing

  This inspection method is also used to check for defects on the testing material surface. Firstly, a paint or fluorescent dye is applied to the testing surface and then the excess is removed. Next, a developer is applied—this could be dry, soluble, suspendable or nonaqueous, depending on the roughness of the surface of the material. The developer absorbs fluorescent dye

from the imperfections highlighting those areas so that they can be identified by the human eyes. In addition, ultraviolet light can help to brighten the colour contrasts between the penetrate and developer.

- Magnetic Particle Testing

  Magnetic particle testing requires iron particles and a ferromagnetic material to implement. The iron particles are first wet and spread on the testing material. The testing object is put into a magnetic field which induced by the ferromagnetic material. The iron particles are then drawn to any imperfections indicating their location and shape.

- Electromagnetic or Eddy Current Testing

  In contrast with the inspection methods mention above, Eddy current testing can be used to detect the defects inside the material. The Eddy current, which flows in a circular path at and below the surface of the material is induced by an alternating magnetic field in a conductive material. If the current flow hits the cracks, the material's conductive and permeability properties the current itself can be changed. An amperemeter can be used to detect the current change in the material (i.e. within just a few microamperes).

- Radiography

  Radiography uses penetrating γ or X-ray radiation to examine the imperfections of the testing object. The X-rays are generated by X-ray generator or radioactive isotope, which penetrates through the material onto a film or other imaging media. The resulting image is shown as a shadowgraph in which a defect or fracture can been seen. This method is also used frequently in the medical industry when testing for broken bones and examining tumours.

- Ultrasonic Testing

  This NDT method is accomplished by introducing a high frequency acoustic

wave into the testing structure. By analysing the pulse echo reflected back or transmitted through a material, the structure and other properties of material, such as the structure of layers can be obtained.

- Acoustic Emission Testing

  Short bursts of sound waves are emitted from the cracks inside solid materials when they are stressed. These emissions can be detected by special receivers (as used in ultrasonic testing); allowing the location and dimensions of the cracks to be determined.

1.4 Laser Ultrasonics—SAW

Laser ultrasonics is a non-contact technique, widely used in NDT applications to generate and detect ultrasound for measuring the thickness, defects and characterisation of materials. The following discussion will now focus on SAWs.

SAW devices and their applications have been well reported in the literature for over 40 years. The most common methods reported utilise contact electronics components (e.g. piezoelectric transducer with wedge and comb) [8], while laser generated SAWs have been—since the first reports of their applications [9]—a major branch research in this field.

1.4.1 Generation Mechanism

There are three basic mechanisms for generating ultrasound by laser:

- The Plasma Regime

  A laser beam hits the surface with enough power to melt the material and release plasma onto the surface. The impulse caused by the vapourisation, and generates a force normal to the surface, and the material is deformed. A longitudinal wave and surface wave are generated efficiently and the amplitudes of transverse waves decline after reaching a maximum value [10].

- The Thermoelastic Regime

  When the laser beam is not powerful enough to melt the material, the energy absorption of the surface raises the local temperature. Hence the longitudinal and transverse waves are radiated because of the thermoelastic expansion and thermoelastic pressure in the area. The amplitudes of longitudinal, transverse and surface waves increase linearly [10].

- The Constrained Surface Source

  For the plasma and thermoelastic regimes, a transparent coating is applied on the material surface to enhance the amplitudes of the three types of waves, especially in the direction of the surface normal.

1.4.2   Modes of Laser Operation

There are two modes of laser operation according to the output power: Continuous Wave (CW) operation and pulsed operation. As indicated by the name, the CW mode has a constant output power over time, or the output power is stable in a long time period.

A pulse laser generates intermittent power output at a fixed repetition rate over a certain time scale. Most of the applications require high peak pulse power, which equals the average power divided by the laser repetition rate. It can be implemented by reducing the pulse width or raising the peak power of the laser. Two main types of pulse laser are Q-switched and mode-locked.

Q-switching is named by decreasing the quality factor 'Q' of the laser cavity. The laser operation does not occur but the energy accumulates in the gain medium. After a certain time the laser quickly switches the low Q to a high Q. The energy is released and it generates a short pulse with high peak intensity. Mock-locking is implemented by fixing the phase of all the modes or frequencies in the resonator, and producing a short pulse which can be as short as a few femtosecond.

1.4.3 Optical Detection

Several techniques of laser detection of ultrasound have been developed and improved. They could be used to measure either the surface displacements (e.g. knife-edge detection and Michelson interferometer), or ultrasound frequency (e.g. Fabry-Perot interferometer). Three common detection methods for ultrasound are introduced in this section along with the advantages for each.

Knife-edge Detection

Knife-edge detection is a type of amplitude variation detection. Figure 1.3 illustrates its working theory. The incident laser beam focuses on a spot which is smaller than half of the wavelength. The surface moves up and down due to SAWs, the amplitude of the angular deviation of the reflected beam is proportional to the local slope. A 'knife-edge' is placed on the path to partially block the reflection beam. Hence the intensity variation received by the single diode is converted from the angular displacement.

Knife-edge detection is simple and inexpensive, but testing surfaces must be flat as knife-edge detection is sensitive to the surface roughness.
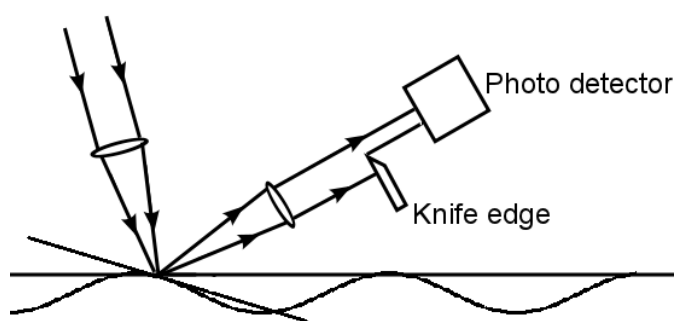

Figure 1.3: Schematic of knife-edge detection.

Michelson Interferometer

The construction of the Michelson interferometer is displayed in Figure 1.4. The incident beam has been split into two and both of them are reflected back to

the photodiode either by the surface or the mirror. In SAWs propagation, the surface motion changes the optical path length of one of the arms of the Michelson interferometer. The optical path difference of the two split beams indicates the phase and amplitude, hence deduces the displacement of the surface.

The Michelson interferometer has high sensitivity in detecting surface displacements of less than an $\mathring{A}$ [11]. It requires lower reflectivity of the sample surface than knife-edge detection, and is the preferred instrument/tool for narrow pulse detection [12].
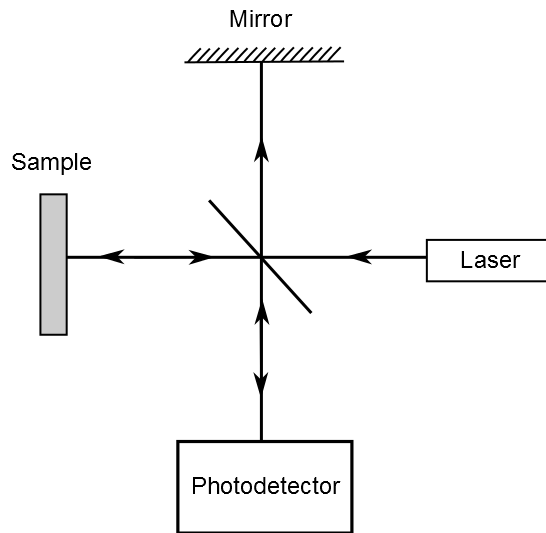
Figure 1.4: Schematic of Michelson Interferometer.

Confocal Fabry-Perot Interferometer (CFPI)

CFPI is described as a two beam time-delay interferometer. As seen in Figure 1.5, two high reflective spherical mirrors with concave surfaces are placed facing each other at a distance d. An incident beam is refracted and reflected repeatedly between two mirrors, causing constructive interference of the reflected beams inside the cavity. The intensity of the transmission beam varies significantly with the small change of input beam frequency.

CFPI has low requirement of surface roughness [13] [14] but the detection bandwidth is limited [15].

Figure 1.5: Schematic of CFPI. Beam 1 and 2 are transmitted beams, 3 and 4 are reflected beams. The distance between two spherical mirrors is d.

1.5 Crystallography

Crystallography studies the arrangement and structure of atoms (or ions) in materials which exhibit long range atomic order. The crystal structure strongly relates to the physical properties of materials. Some materials have the same chemical compositions but different crystal structure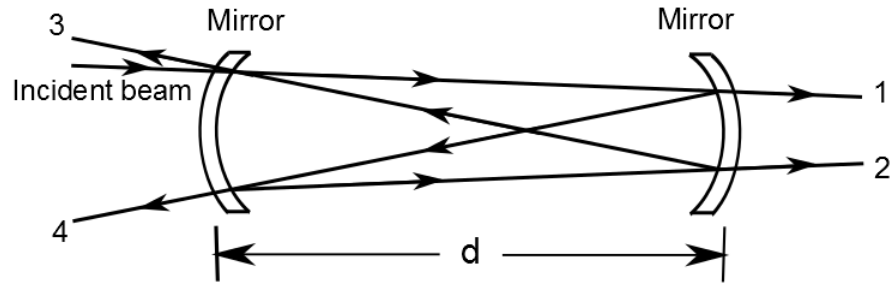s and status (called 'phase') resulting in significant difference between materials. For example, under different temperature and pressure, titanium alloy has phase transitions between α, $\alpha + \beta$ and β; each phase has different levels of performance for tensile strength, plastic property and percentage elongation.

Miller indices provide figures to define the planes and directions in the crystal system. It uses three numbers h, k and l written as $[hkl]$ to note a direction based on the direct lattice vectors, or (hkl) for a plane that is orthogonal to this direction. The notation $\langle hkl \rangle$ describes the directions that are equivalent to $[hkl]$ by symmetry, and the planes noted as $\{hkl\}$ are equivalent to (hkl) similarly. This notations are normally written in integers with lowest terms.

1.5.1 Crystal System

There are seven classes of crystal structures. Materials in the same crystal system share a similar symmetry, which plays a key role in determining the physical prop-

erties of the material. Seven types of crystal structures are given in Table 1.1 with examples.

Crystal System	Simple Example	Length of Axial	Angle between Axial
Triclinic		a ≠ b ≠ c	$\alpha \neq \beta \neq \gamma \neq 90°$
Monoclinic		a ≠ b ≠ c	$\alpha = \gamma = 90°$ $\beta \neq 90°$
Orthorhombic		a ≠ b ≠ c	$\alpha = \beta = \gamma = 90°$
Rhombohedral		a = b = c	$\alpha = \beta = \gamma \neq 90°$
Tetragonal		a = b ≠ c	$\alpha = \beta = \gamma = 90°$
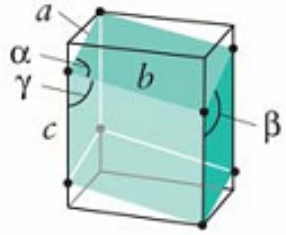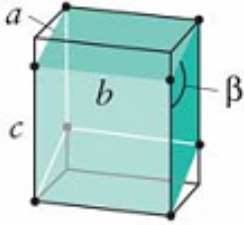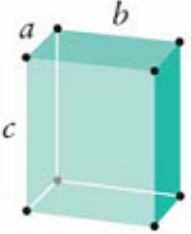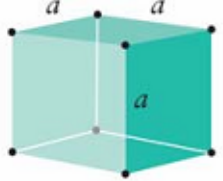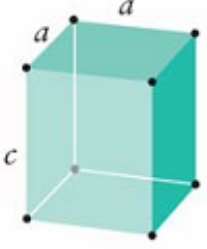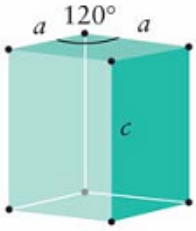
Hexagonal		a= b ≠ c	$\alpha = \beta = 90°$ $\gamma = 120°$
Cubic		a = b = c	$\alpha = \beta = \gamma = 90°$
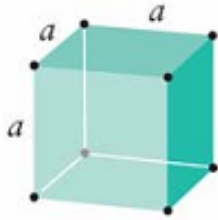
Table 1.1: Seven classes of crystal structures [16].

1.5.2 Characterisation of Crystal Structure

Several techniques were developed for measuring the microstructure of materials, including the size of grains and the orientation of crystals. In this section the XRD-LBR method and EBSD are introduced. These are compared with the SRAS results in later chapters.

X-ray diffraction (XRD) Laue back-reflection (LBR) Method

X-rays are electromagnetic radiation waves with a wavelength of 0.01 to 10nm. They share the same light behaviours as other electromagnetic waves, including reflection, refraction, scattering, interference, diffraction, polarisation and absorption. The distance between atoms and molecules (approximately 1 to 10 $\mathring{A}$) just falls within the X-rays wavelength range and the crystal structure of a material can be determined by X-rays scattering and diffraction.

Bragg's law is defined as

$$2d\sin\theta = n\lambda \qquad (1.4)$$

where d is the interplanar distance of lattice, θ is the scattering angle, λ is the wavelength as can be seen in Figure 1.6, and n is an integer determined by the order given.
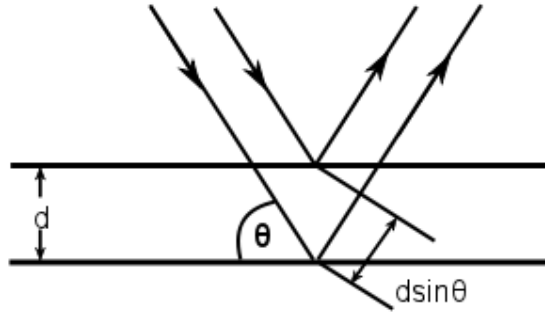
Figure 1.6: Bragg diffraction.

LBR method is an XRD technique named after Max von Laue, the pioneer of the diffraction of X-rays. In this method a (white) incident X-ray beam strikes a single crystal surface orientated perpendicular of the beam. As its d and θ are fixed by the lattice parameters and orientation respectively, several wavelengths from the broad spectrum can be reflected in different orders from the each set of planes satisfying the specifications of Bragg's law. A film is placed between the X-ray source and crystal to record the backwards diffraction, which is called a Laue pattern.

The interpretation of the Laue pattern to the crystal orientation is accomplished by using a Greninger chart [17] manually, or computer software which uses a compatible generated overlay mask [18]. The results are given in primary orientation angles (see Appendix D).

LBR method is a fast way for measuring the orientation of single crystals. Typically the lateral resolution of the system is 2mm in diameter with an error of $\pm 1.5°$ [18].

Electron Backscattered Diffraction (EBSD)

EBSD is a technique using a Scanning Electron Microscope (SEM) to obtain sample crystallographic characteristics. It emits an electrons beam onto a sample surface at a certain angle. Analysis of the diffraction pattern gives information about the crystal orientations, boundaries and disorientation between grains.

EBSD also obeys Bragg's law's Equation 1.4 because of the Wave-particle duality of electrons. The sample is placed at a tilting angle, typically 60°–70° [19] in a SEM chamber, the incident electrons beam interacts with the atoms in the sample and inelasically scatters (the scattered beam keeps the same wavelength as the incident beam). Some of the scattered electrons satisfy the Bragg angle θ when incident on certain plane of crystal, and diffracted to produce large angle cones which are corresponding to the diffraction plane. The image of Kikuchi bands of the electron back scattered diffraction pattern is caught by a fluorescent screen. Several methods were developed in the past to locate the pattern of Kikuchi bands. Burns algorithm [20] and Hough transformation [21] are two reliable translation methods among them. The results are translated to the crystal orientation in the Miller indices. By scanning the sample surface in a grid by electrons beam, the orientation of crystal can be measured at each point across the sample, a map is presented to reveal the crystallographic orientation and microstructure.

Because electrons beams are highly attenuated in gas, this technique must be operated in a vacuum chamber. Due to the high sensitivity of the technique, samples must be sufficiently polished. The spatial resolution of EBSD is decided by SEM conditions, sample and the electron source. Grain size not smaller than 10nm is distinct under optimal conditions with system error of $\pm 0.5°$ [22].

Both XRD and EBSD are useful of microstructure studies and examine the materials in different scale of resolution. Currently EBSD is the most popular technique in crystallographic research.

Chapter 2

Spatially Resolved Acoustic Spectroscopy

2.1 Introduction

Spatially Resolved Acoustic Spectroscopy (SRAS) is a nondestructive testing method which maps the SAWs velocity on a material's surface. The velocity contrast of SAWs reveals the material's microstructure and orientation of crystals. This can also be accomplished by other methods such as EBSD, which gains crystallographic information by impinging electrons onto the sample and analysing diffraction patterns [22]. Alternatively, the Scanning Acoustic Microscope (SAM), a contact technique, analyses the phase shift of a narrow band SAWs signal. Both these methods have disadvantages such as restriction on sample size, or (in the case of the SAM) ambiguity caused by a periodic phase function. SRAS eliminates those concerns. It is based on the spectroscopy technique (perhaps more familiar in optics) and uses the spectral characteristics of acoustic waves.

SRAS is a new technique to image the SAWs velocity over the surface. It is based on the spectroscopy technique but differs because it uses the acoustic characteristics of waves. This method is used to measure the velocity of the SAWs

over individual grains for several types of industrial materials such as aluminium alloys and titanium alloys, and produces a SAW phase velocity map over the sample surface as shown in Figure 2.1. A faster velocity is indicated on the left whilst a slower velocity is indicated on the right, corresponding with two grains at different orientations. SAWs velocity, as a function of intensity of received signal, can be observed via the waveforms on the left and right in the figure.
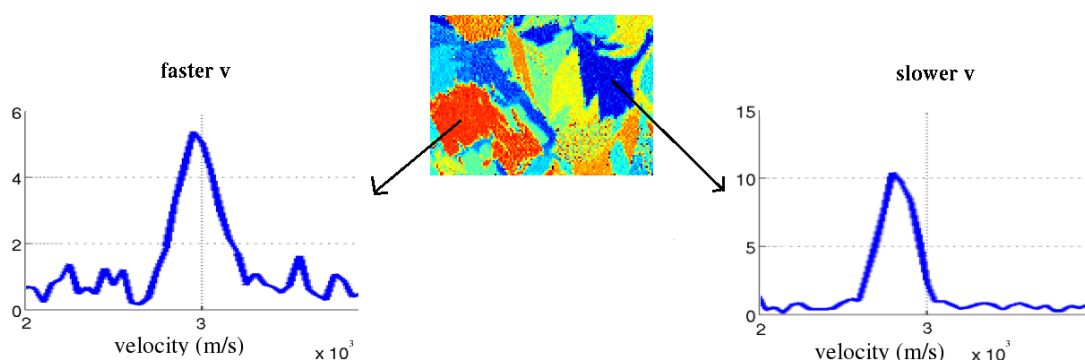
Figure 2.1: SAW velocity difference shows the contrast of two grains.

2.2 K-vector SRAS (k-SRAS)

2.2.1 Theory

The k-SRAS technique and its system have been developed in Applied Optics Group of University of Nottingham for quite a few years [23]. The scheme of k-SRAS is shown in Figure 2.2. A laser source generates a fixed frequency light beam which goes through a Spatial Light Modulator (SLM) and a grating pattern hits the sample material surface. SAWs are excited by excitation laser at the same time and travel along the sample surface to the receiver.
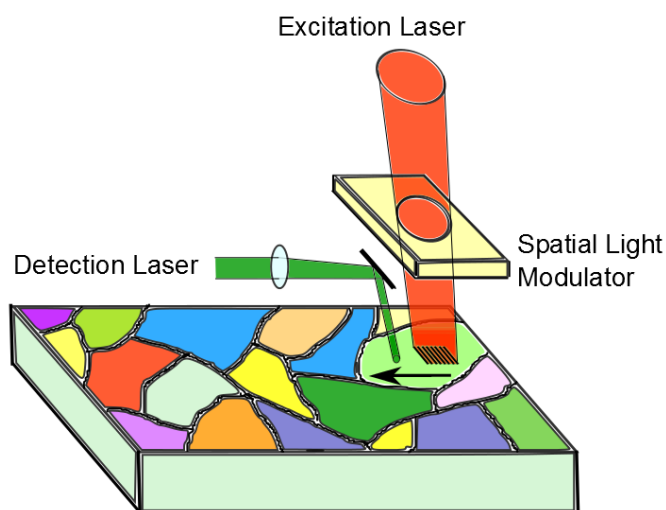
Figure 2.2: Scheme of k-SRAS.

A grating pattern with even spacing is used to generate a SAWs packet which propagates on the sample surface. Figure 2.3 illustrates how each line of the pattern generates SAWs within a short period of time $t1$. The received signal on the right is by adding together all of the SAWs. In reality, SAWs propagate towards both directions. The spacing of grating that is generated by the SLM is changed over a likely range of the SAWs' wavelength.
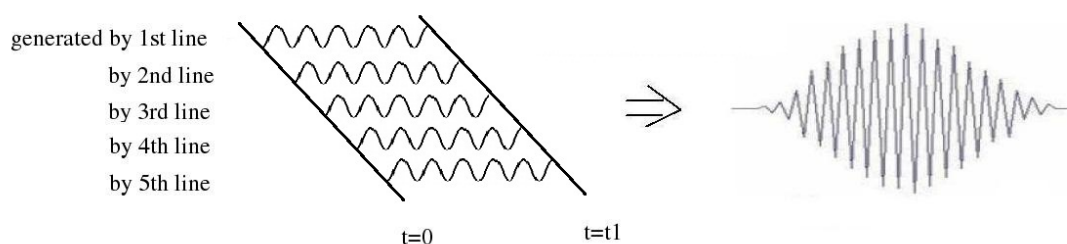
Figure 2.3: The waves packet is generated by fringes in a selected spacing.

Each time when the spacing is changed, a waveform is received by a broadband detector. If the grating spacing matches the SAWs wavelength, the frequency response of the overlapped waves packet, (e.g. as shown in Figure 2.3), at the receiver, is a sharp Gaussian-like wave with large peak. In contrast, when the

spacing distance does not match the wavelength, the frequency response has a bigger bandwidth and a smaller amplitude.

This procedure is illustrated in Figure 2.4. After Fast Fourier Transform (FFT) of these waveforms, the amplitude of frequency responses are plotted as a function of the grating line spacing. A curve similar to a Gaussian wave is consequently formed. The corresponding spacing of the largest amplitude on this curve is located; this spacing distance equals the wavelength of the SAWs which was generated. Because the wave frequency is fixed, the velocity of the wave is calculated using the wavelength and the frequency. Due to the nature of the generation mechanism of laser ultrasound, the calculated velocity is represented in the grain's property under the grating pattern on the sample surface, not at the receiver. The Gaussian curve fit is used at all times to locate the peak value of all curves as the blue line shown in the right of Figure 2.4.
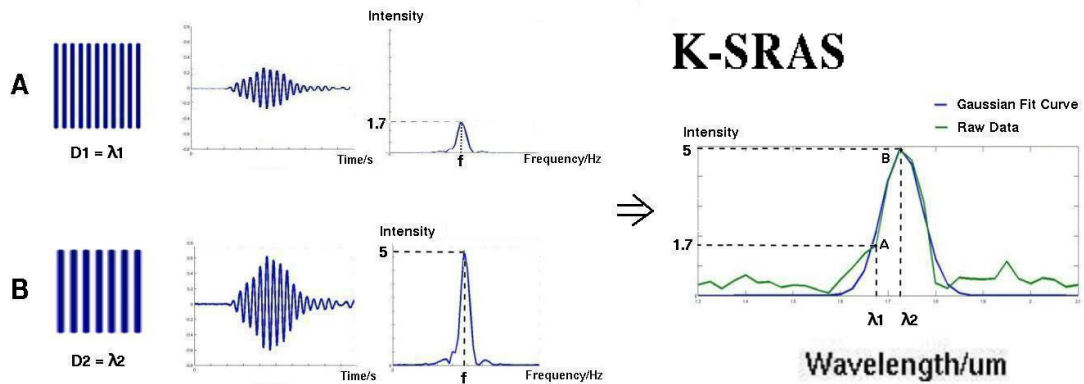
Figure 2.4: This is the theory of k-SRAS: two wave packets are generated by fringe patterns A and B with spacing of D1 and D2, the amplitude of wave's frequency is the largest when the spacing matches the wavelength $\lambda 2$ of SAW.

If a titanium testing sample and an operation frequency of 82MHz is used, (with SAWs velocities approximately ranging between 2800m/s to 3200m/s), according to $\lambda = v/f$, the determined wavelength of SAWs should fall between [34.15μm, 39.02μm]; therefore, the range of scanning fringes spacing should be larger than the interval mentioned above. If the pattern size is 300μm×300μm,

the maximum number of fringes on the pattern is 9. If the pattern size is reduced to 100μm$\times100\mu$m, the resolution is improved. Nevertheless, the Signal to Noise Ratio (SNR) is degenerated because the maximum number of fringes falls to 2. As explained earlier, the frequency response of a received signal has a smaller amplitude and narrower bandwidth if the number of fringes is less. As a result, there is a bigger error margin when the search function is used to find the centre frequency of the curve. In conclusion, the resolution of a velocities image is proportional to the operation frequency and is inversely proportional to the SLM size, though these two factors do interact with each other.

The Figure 2.4 used a square grating pattern as an example. However, in the case of a low SNR, (i.e. due to sample surface roughness), arcs in an even spacing can be used to generate a grating pattern and therefore enhance the SNR. When comparing the two types of SLM patterns in Figure 2.5, there is more energy flow to the detecting points on the curves pattern when the detecting point is at the focus of the arcs. The arcs pattern improves the SNR. However, it is not a true representation of the SAWs' velocity for the direction; the ambiguity of velocity depends on the curvature.

(a)   (b)
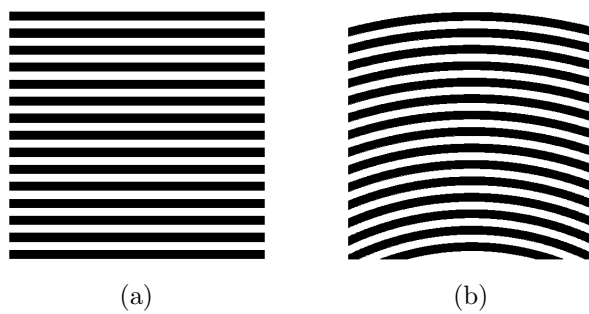
Figure 2.5: Patterns of SLM: lines and arcs.

2.2.2 Instrumentation

The k-SRAS system has major components of a Q-switched laser, SLM, detection unit, oscilloscope and a computer controlled scan stage; the computer connects

to the oscilloscope for data acquisition and processing. The sample is positioned by the scanning stage, which consists of four separate units: XY stage, Z axis stage, rotation stage and tilting stage. The received unit of k-SRAS system is CW Nd:YAG laser with modified knife-edge detector. The schematic and photo of the k-SRAS system are shown in Figure 2.6.
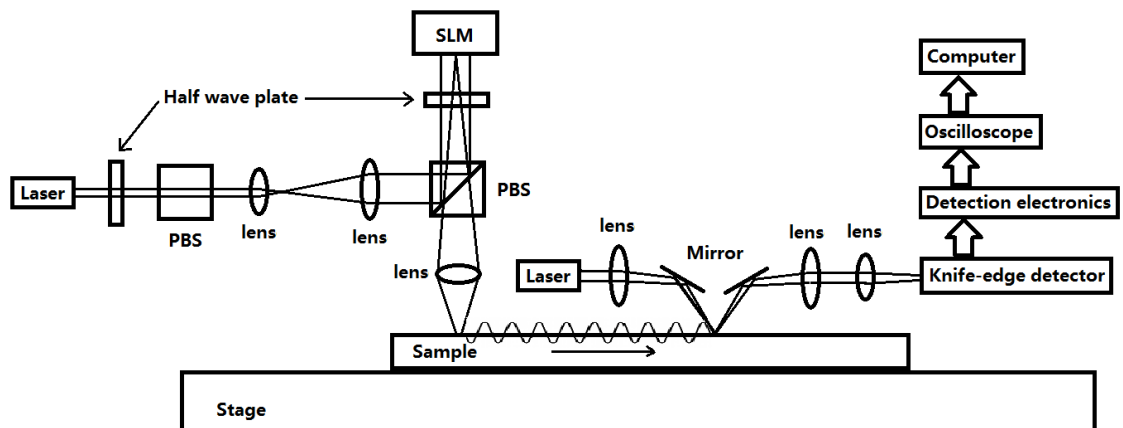
(a)
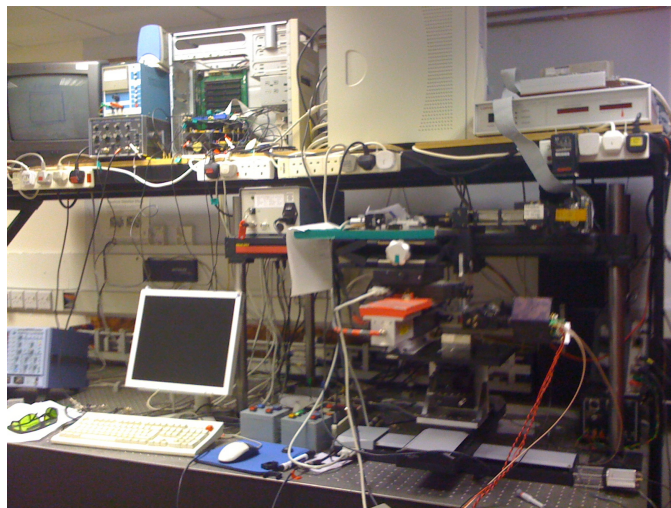
(b)

Figure 2.6: System construction [1] and photo of k-SRAS system.

Excitation Source

The surface acoustic wave is generated by a Q-switched mode locked Nd:YAG laser with a wavelength of 1064nm. The mean output power of the laser is 2W and the peak energy of a single pulse is approximately 0.3MJ [1]. The operation frequencies of the system are set at 82MHz, which is determined by the cavity length of the laser and by multiples of 82MHz (e.g. 164MHz, 328MHz and so on). The repetition rate of the laser is also adjustable within the range of a few hundred hertz to 10kHz; this determines the measurement speed of the instrument. The grating pattern is generated by the SLM and projects on the sample, which is fixed on a computer controlled scan stage.

Signal Detection

The SAWs are detected by a CW Nd:YAG laser with an optical power of 100mW at a wavelength of 532nm. They travel a short distance, around half of the SLM size, on the sample surface and reach the detection point. In order to utilise the optical energy more efficiently, a split photodiode is used in the knife-edge detector rather than the single diode (described in Chapter 1.4.3). The extra diode replaces the knife-edge in this modified version. When the reflected beam is deflected by the oscillation of the SAWs, the intensity of light varies inversely on two diodes, hence the angular displacement of the reflected beam is determined by the difference between the two intensities.

Data Acquisition

A high speed complex amplitude analogue acquisition system is used. After the laser has completed the scanning of the sample material and has calculated the velocity of each pixel, an image of velocities can be plotted by the computer analysing program.

Figure 2.7 shows the measured result on a single point of the sample surface;

the SAWs' amplitude varies with the grating line spacing which corresponds to the SAWs' wavelength. The blue solid line with circles represents the amplitudes of the SAWs' which are derived from the experimental data. The green solid line with crosses describes the Gaussian curve fitted to the experimental data. By finding the largest amplitude of received signals and using the formula $v = \lambda f$, the velocity of a grain (the speed at which the SAWs travel over the individual grains) at a specific testing position is measured for the sample material.
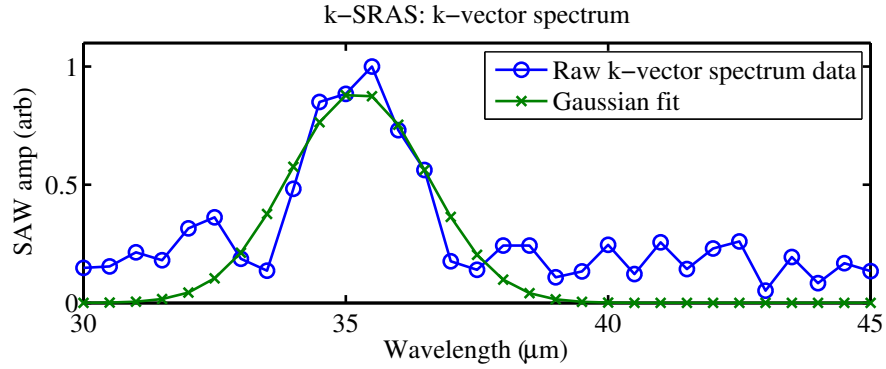
Figure 2.7: SAWs amplitude respect to the grating spacing of SLM.

2.2.3   System Accuracy

The resolution of images of velocities are determined by the step size when the grating pattern moves on the sample surface also the size of the grating patterns and the operation frequency. Most of the time the step size is equal to the SLM pattern size. If the step size is smaller than the SLM size, the velocity of pixels transit more smoothly. However, if step size is larger, some areas are not covered by the SLM pattern during the whole scanning, hence the velocity map does not provide a full and informative representation of the sample surface.

The scanning stage alignment is set at the same horizontal level for the SLM projection and the sample surface. Any defocus of laser beam or tilts of the sample would cause deformation of the SLM pattern and fringe spacing, thus the velocity would be influenced indirectly. The lateral resolution is approximately half of the

SLM size [24].

As seen in Figure 2.8 [24], an isotropic glass sample that is coated with aluminium is scanned by the k-SRAS system and the velocity map is shown. The SAW phase velocity should be uniform across the area. However the velocity range is 2962.5m/s±1.5m/s; the standard deviation of velocity is 0.89m/s corresponding to 0.03%.
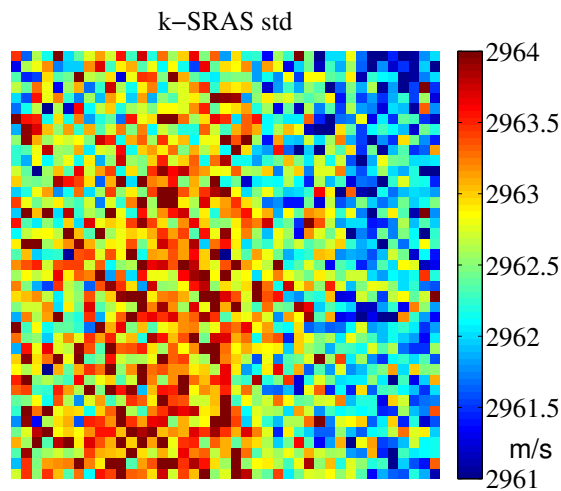
Figure 2.8: Velocity of map of isotropic aluminium coated glass [24]. The image size is 10x10mm, pixel size is 250μm; the standard deviation of velocity is 0.89m/s.

2.3 Frequency SRAS (f-SRAS)

2.3.1 Theory

Another approach of implementation is called f-SRAS, which is implied by its name and implemented by changing the frequency of $v = \lambda f$. A pulsed laser is used as the excitation source in this version of SRAS. Alternatively, the laser could be capable of being modulated by a series of sine waves with different frequencies. Both of these methods are capable of implementing frequency scanning, although the broadband excitation source is generally quicker and is the method used to acquire the experimental results in the current system. A glass mask coated with chrome is used to generate a fringe pattern with fixed spacing instead of SLM.

Each of the fringes generate a series of SAWs which cover a range of frequencies. These are received by the detection laser with a knife-edge detector and only the SAWs whose wavelengths are equal to the fringe spacing are enhanced in intensity.

The grating excitation pattern acts as a filter on the generation of the SAWs and is multiplied with the frequency content of the laser. The effective centre frequency of the grating is determined by the grating period and the local velocity ($v = f\lambda$ again) as shown in Figure 2.9. As the wavelength of the SAWs equals the fringe spacing and its frequency is known, the local velocity is calculated. F-SRAS is potentially faster than the k-SRAS system because the measuring speed of scanning a sample area is the same as the repetition speed of the emission laser in f-SRAS. Unlike in the k-SRAS system, the SLM must be changed several times, which is the same number of times of laser emission, to produce the velocity information at one testing point, the laser only fires once to obtain the frequency information in f-SRAS.
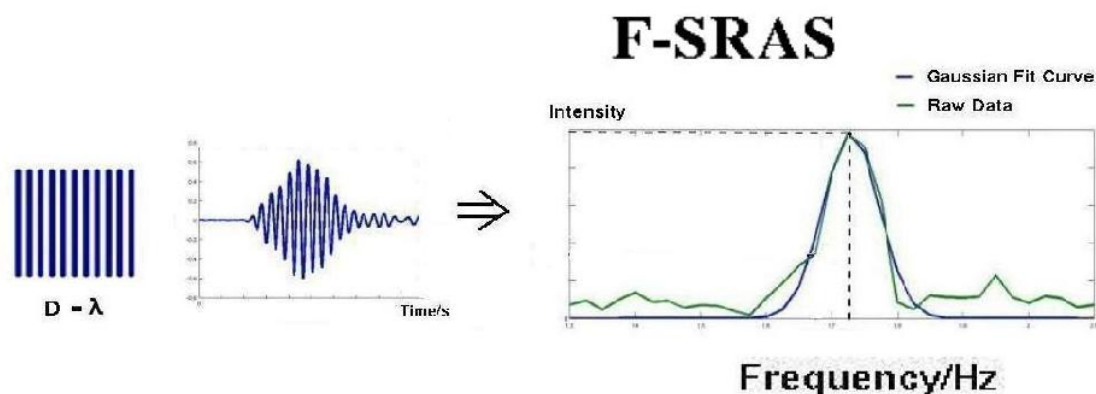
Figure 2.9: Theory of f-SRAS

2.3.2   Instrumentation

The f-SRAS system, in Figure 2.10, has the major components of a Q-switched laser, including an optical mask, a detection unit, an oscilloscope and a computer controlled scan stage; the computer also connects to the oscilloscope for data acquisition and processing. The sample is positioned by the scanning stage, which

consists of XY stage, Z axis stage, rotation stage and tilting stage. The received unit of f-SRAS system is the same as k-SRAS: CW Nd:YAG laser with modified knife-edge detector. The photo of the system is also illustrated in the figure.

(a)

(b)
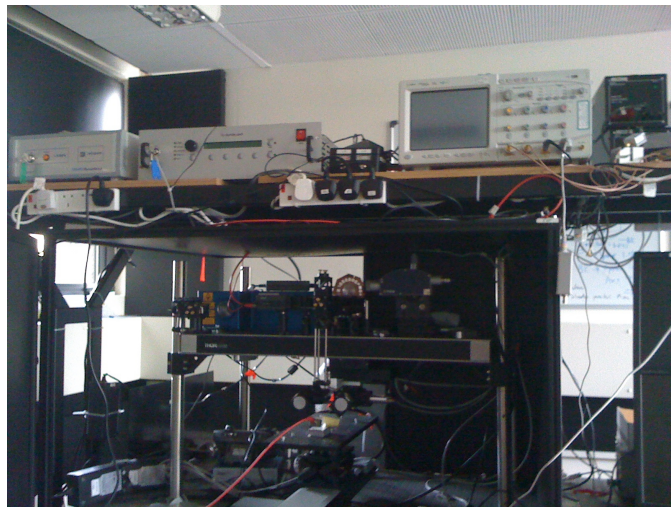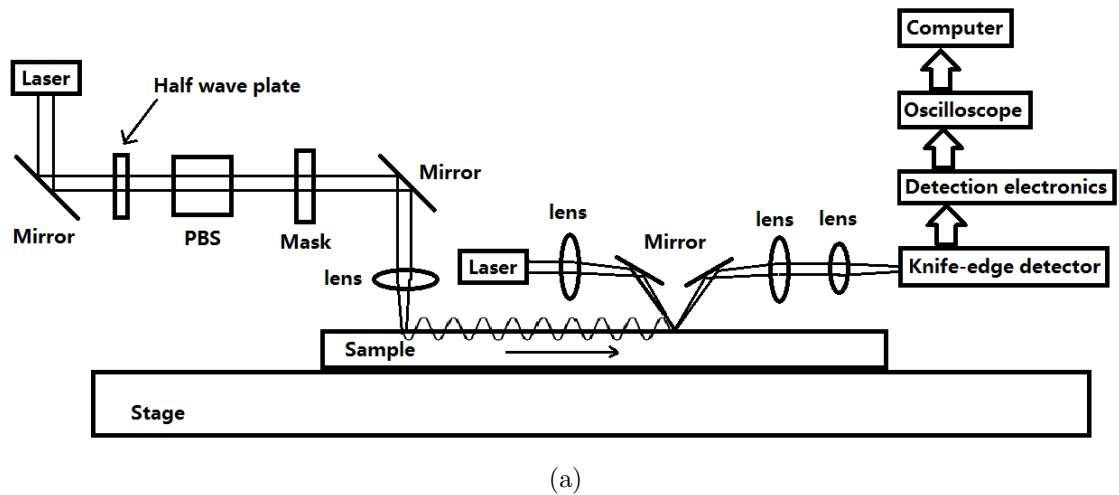
Figure 2.10: Schematic and photo of f-SRAS laser ultrasound system.

Excitation Source

The Q-switch laser signal has a short pulse (<10ns) with 135mJ per pulse and a peak power of 13.5kW. The laser beam is 2mm in diameter, and gives a power density of 8.6W/cm^2 per pulse. It has a wide bandwidth from DC to >100MHz. The

time and frequency response of the emission laser are demonstrated in Figure 2.11; the frequency spectrum in the right hand side of the figure decreases slowly as the frequency increases.
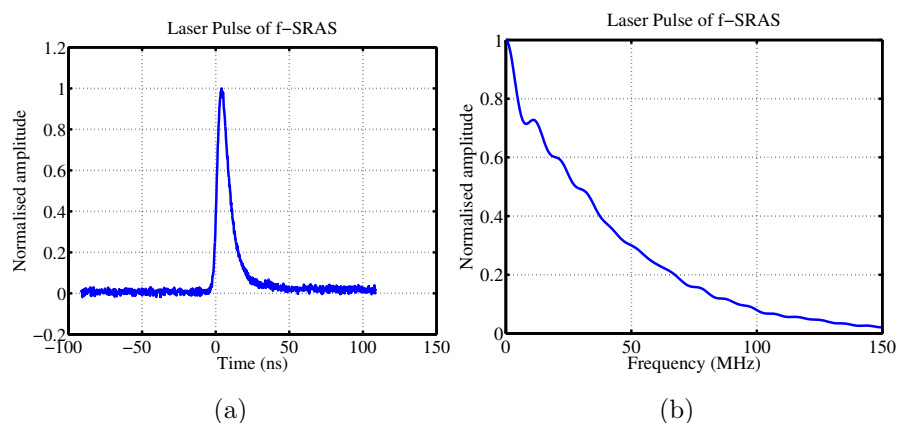
Figure 2.11: Broadband laser signal of f-SRAS system in time and frequency domain.

Mask Design

The pulsed laser beam passes through a mask, which is 8mm by 10mm in size, consisting of a set of stripes, as shown in Figure 2.12. The unblocked light excites SAWs when it is imaged onto the sample surface. In our instrument there are twenty masks that have different curvatures and fringe spacings, to cover a range of different materials and conditions. A smaller distance between the fringes generates SAWs with a shorter wavelength and higher frequency. A straight (rather than focused) grating was used, which had an effective period of 43.5μm on the sample. The patch size was 300μm in diameter—less than 1mm^2 on the sample surface. Since the effective bandwidth of the filtering action of the grating generation is much smaller than the bandwidth of the laser pulse we can make the assumption that the frequency content of the laser is locally flat across the bandwidth of the grating and hence that the peak of the combined frequency response is at the same location as the peak of the grating filter; thus we can determine the local velocity.
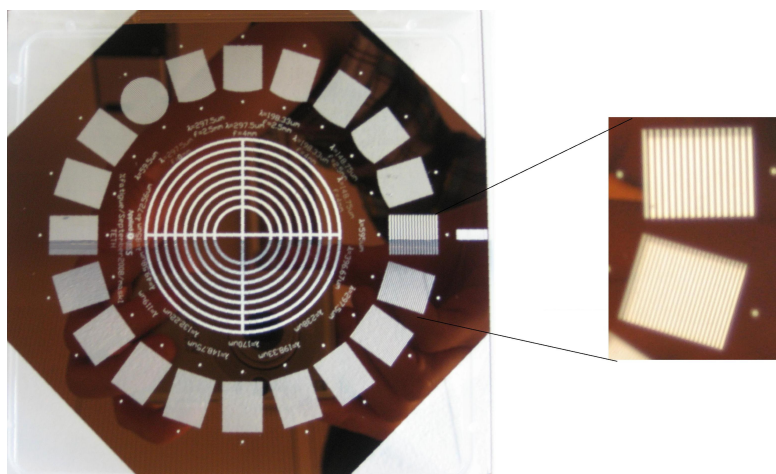
Figure 2.12: Example of optical masks used to generate SAWs. Only one mask is used in each scanning.

Data Acquisition

The oscilloscope recorded the SAWs waveforms every time the laser fired and this data was downloaded to a computer. Because the laser repetition rate was much faster than the reading and writing speed of oscilloscope and computer, this working mode slowed down the system measurement speed. The segmented memory of the scope was utilised (storing the waveforms in a stack) and the scope communicated with the computer only when the memory was full. As a result, waveforms did not have to be transferred individually at single measuring point. Moreover, the waveforms were collected when a single pulse of laser fired, hence a certain numbers of adjacent waveforms could be averaged as a single point measurement to improve the SNR. The disadvantage of this method was the increase in step size (equals the times of average of original step size) which reduced the resolution of the velocity mapping.

Figure 2.13 shows a typical SAWs signal captured by the system. The spacing of the grating determines the wavelength of the SAWs. The top graph is the waveform in a time domain; the FFT is in the bottom graph along with a Gaussian curve (green line with crosses) which has been fitted to the raw FFT data (blue line with

circles). The frequency where the amplitude is the largest indicates the closest value corresponding to the SAWs travelling on the grain. Note that the velocity measurement relates to the sample area under the generation patch, rather than at the detection point or inbetween the generation and detection.
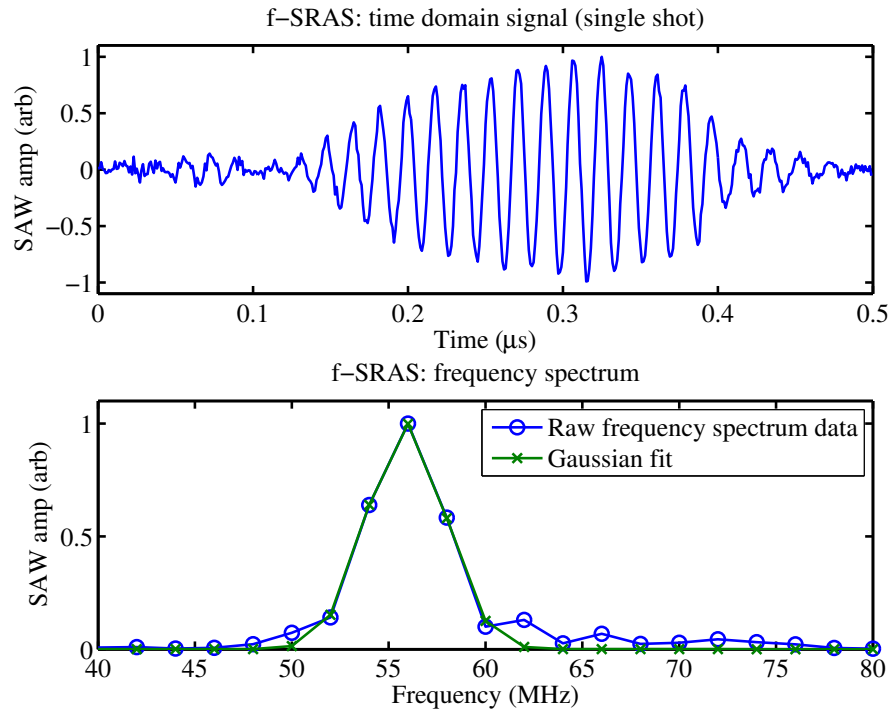
Figure 2.13: Raw data in the time domain (top) and frequency domain (bottom) with Gaussian fit.

2.3.3 System Accuracy

A glass sample which was coated with a thin layer of aluminium at a size of 1×1mm (to improve the SNR of SAWs) was tested. It was an isotropic material and ideal for evaluating the velocity accuracy of the f-SRAS system. Figure 2.14 displays the velocity maps of the ideal sample. It was measured by using a mask with a grating spacing of 64μm—the experimental data was taken at 16 points average.

The velocity varied between 2933m/s to 2938m/s, and gave a standard deviation of 0.89%, which corresponded to 0.03%. It was the same velocity accuracy as the k-SRAS system.
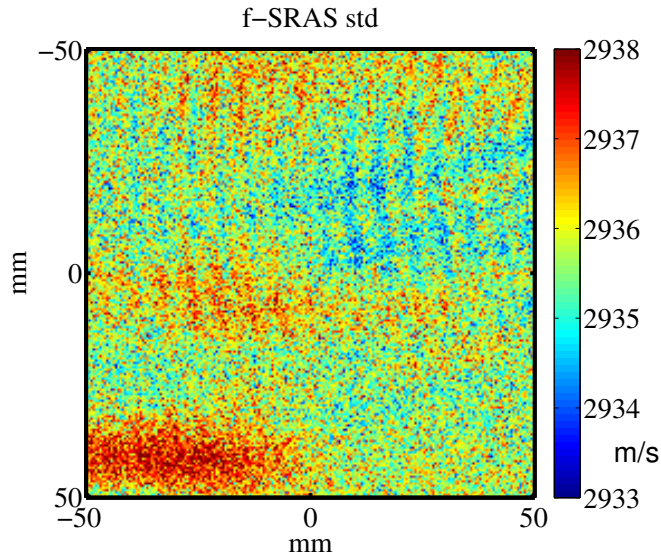
Figure 2.14: Standard deviation test of f-SRAS system under temperature control. Image size is 1×1mm with pixel size of $5 \times 5\mu$m. The grating distance of mask is 64μm, data is 16 points average. Velocity range over the whole area is 2935.5 ± 2.5m/s, the standard deviation is 0.89m/s, corresponds to 0.03% [25].

Since the SAWs velocity was very sensitive to the operation temperature, for instance on aluminium as the temperature decreases the velocity rises by approximately 3.7m/s/°C between 22.5°C and 27.5°C [26]. Figure 2.15 demonstrates how strongly the temperature variation influenced the velocity for the same sample. The velocity decreased gradually along with the scanning order in time; the velocity range over the whole area was 2938 ± 7m/s, the standard deviation was 3.13m/s, corresponding to 0.11%—nearly four times higher compared to the standard deviation under normal operating circumstances 0.03%. The variation of the room temperature is illustrated on the right figure. This rose approximately 2°C during the scanning from 12:00 to 14:30. It caused a velocity decline of approximately 12m/s over the sample surface.

(a)   (b)
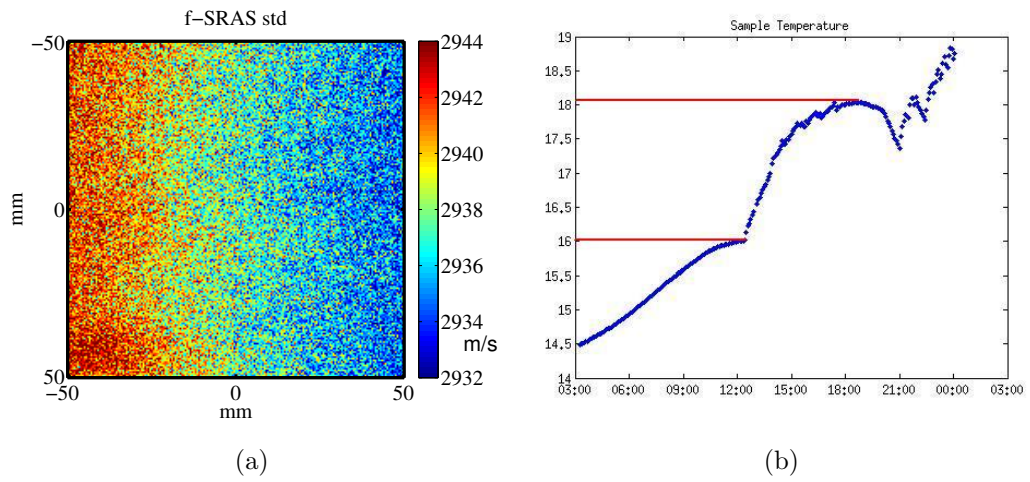
Figure 2.15: Left figure shows the ideal sample velocity map by f-SRAS without temperature control. Image size is 1×1mm with pixel size of 5×5μm. The grating distance of mask is 64μm, data is 16 points average. Temperature change during the experiment period is shown on the right.

Chapter 3

SRAS Results

The surface acoustic wave velocity measurement taken using the SRAS technique is local to the area where the waves are being generated. As the measurement is relatively fast the sample may be scanned and an image built up of the SAW velocity over the sample. The velocity at any point is determined by the material elastic parameters at that point and the resulting images clearly reveal the grain structure. This method is used to measure the velocity of the SAW over individual grains on several industrial materials such as aluminium and titanium alloys. The variations of velocities, which indicate the change in orientations of grains, are presented as a colour map.

The velocity scan results of an aluminium sample and several titanium alloy samples taken by both k-SRAS and f-SRAS are presented in this chapter. The two methods are compared in terms of the images of SAW velocity produced. Images where SAW are propagated in either two or three directions on the same sample are presented, and compared, qualitatively, with EBSD results. Finally, velocity surfaces over 360° of nickel and aluminium single crystals are measured and illustrated.

All the tested samples have a smooth polished surface, due to the sensitivity of knife-edge detector.

3.1 K-SRAS

Figure 3.1 shows the velocity maps of a Ti-685 sample which are acquired using the
k-SRAS system with a laser frequency of 164MHz, with typical SAW wavelengths
of 16–19μm. The top figure presents the velocity variation when SAWs propagate
from left to right, while the bottom one refers to SAWs propagating from bottom
to top. The image size is 84×36mm; the scanning step size (the pixel size) is
250×250μm in each figure. The grains of the sample are distinguished easily by
the velocity contrast. The colour bar presents the velocity from 2700m/s (dark
blue) to 3400m/s (dark red).
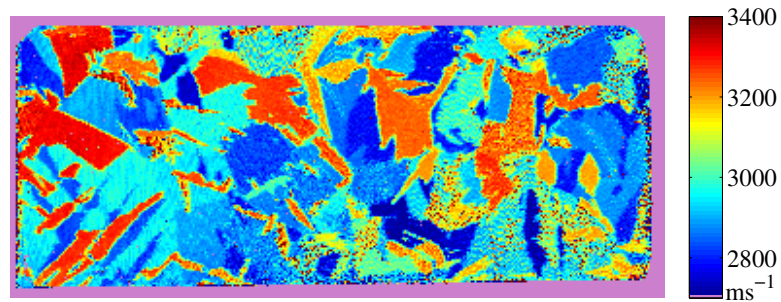
(a) Left to right.
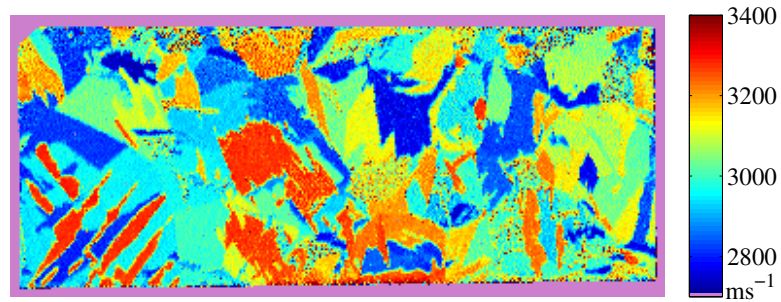
(b) Top to bottom.

Figure 3.1: SAW velocity map of Ti-685: SAWs propagating left to right (top),
and bottom to top (bottom). Image size 84×36mm, pixel size 250×250μm [27].

3.2   F-SRAS

Figure 3.2 shows four velocity maps of the same Ti-635 sample which are acquired using the f-SRAS system. Figure 3.2a and Figure 3.2c are images acquired at a low resolution, the step size is 500μm. It is worthwhile because each scan takes only three minutes to acquire 105×55 pixels; the maximum scan speed is 60 pixels/second, using single shot data for each point (no averaging). The image was acquired before the fast segmented memory data acquisition method—described in section 2.3.2—was implemented; the maximum scan rate of 60 points/second is defined by the maximum number of individual traces per second that the oscilloscope can record. At a slightly higher resolution, a pixel size of 200μm, 15 minutes for one scan is sufficient and the results are shown in Figure 3.2b and Figure 3.2d. The colours in the image represent the SAW velocity in the range 2600m/s (dark blue) to 3400m/s (dark red).

(a) Pixel size: 500μm.   (b) Pixel size: 200μm.

(c) Pixel size: 500μm.   (d) Pixel size: 200μm.
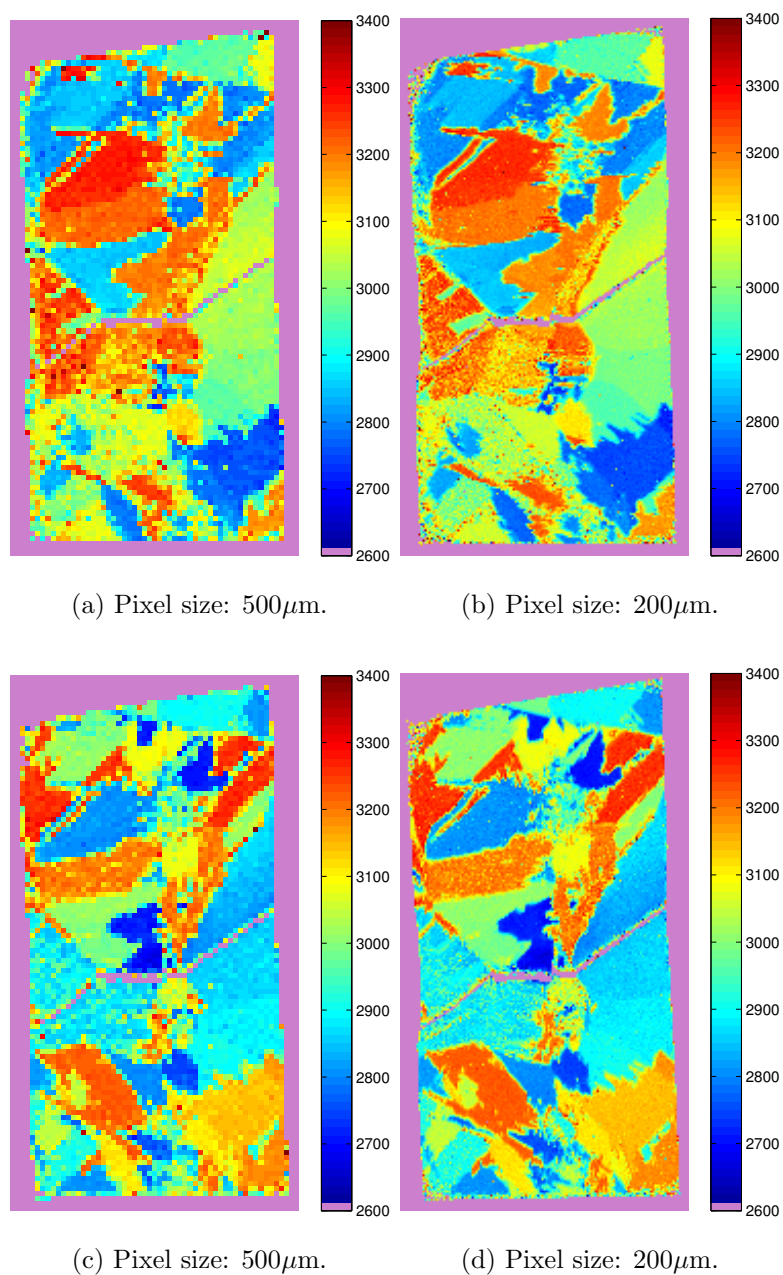
Figure 3.2: SAW velocity map of Ti-635: image size 27.4×52.4mm, pixel size 500×500μm (left), 200×200μm (right). SAWs propagating left to right (top two figures), and propagating bottom to top (bottom two figures) [28]. A 'z' shape crack can be seen across the sample and divides it into two pieces.

Figure 3.3 shows the same sample in a finer step size (50μm), and the scanning speed was improved by utilising the oscilloscope's segmented memory, as described

in section 2.3.2. 40 minutes is needed to obtain each of the velocity maps, which are measured at a scan speed of 238 points/second. The repetition rate of the generation laser is 1kHz and every single pulse results in an acquired trace which corresponds to one velocity measurement. The reduction in the overall scanning rate is due to two factors. The dominant factor is the limitation in the speed of the stages used to scan the sample, and the fact that data is only acquired in one direction; the flyback at the end of each line is dead time. Additionally, there is a delay as the acquired data is transferred from the fast acquisition memory in the oscilloscope to the host PC's memory.

After the scanning speed improvements described above, another bottleneck that was overcome was the processing of the raw data, whereby a Gaussian curve was fitted to the acoustic spectrum to determine the peak frequency. In order to solve this problem, the time trace data were zero-padded prior to performing the FFT (to get the amplitude frequency spectrum), this has the effect of interpolating the spectrum in the frequency domain. The peak of this interpolated spectrum is then found, rather than using Gaussian curve fit, which improves the processing speed significantly.

It should be noted that this different processing technique affects the calculated peak velocity significantly where there is more than one peak in the spectrum. The grain in the square of Figure 3.3a is presented in orange in Figure 3.2a and 3.2b but is a mixture of dark red and cyan in Figure 3.3a. This is because there are two peaks with similar amplitude in the frequency spectrum of those tested points. The 'peak searching' method picked the peak with larger amplitude in Figure 3.3a, whereas the Gaussian curve fit returned an intermediate value of the peaks in Figure 3.2a and 3.2b.

(a) Left to right.

(b) Top to bottom.
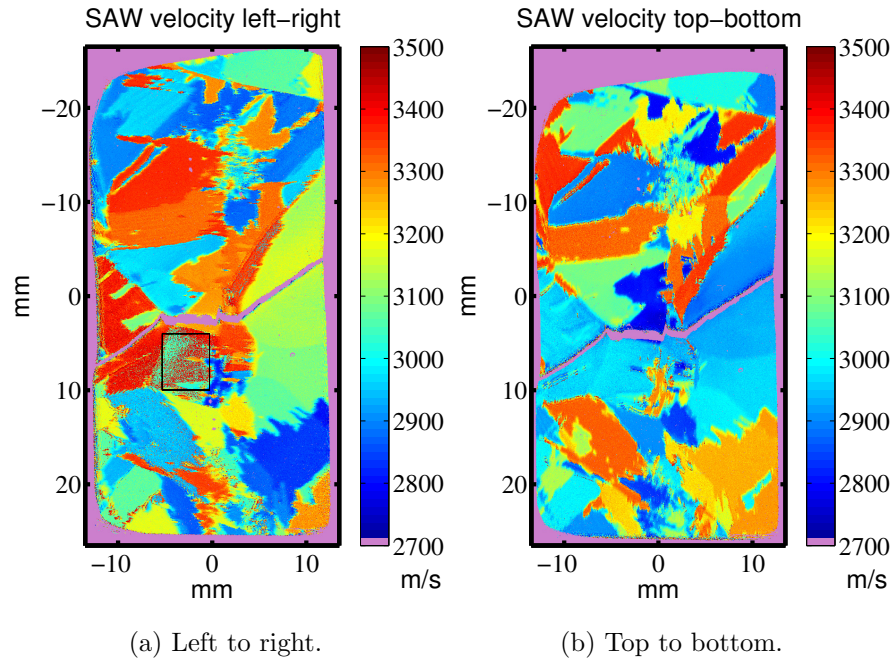
Figure 3.3: SAW velocity map of Ti-635: image size 27.4×52.4mm, pixel size 50×50μm. SAWs propagating left to right (left), and propagating bottom to top (right).

3.3 Data Fusion

A 'velocity vector map' can be obtained by combining the two velocity maps where SAWs are propagating in orthogonal directions. The velocity maps on the right of Figure 3.2 are used here as an example. The resulting velocity vector map shown in Figure 3.4d is compared to the etched picture (Figure 3.4a) and the EBSD orientation image of the same sample, shown in Figure 3.4b. EBSD is a much more established and mature technique—the image provides true crystallographic orientation, whereas the velocity vector map is an approximate approach.

The etched picture gave good contrast of grain boundaries without orientation information. There are a few grain boundaries not distinct in the velocity vector map but obvious in the EBSD figure; two reasons are discussed for this inconsistency as follows. Firstly, the velocities of two neighbouring grains may be

very close, when the grains are almost oriented in the same direction. However, the velocity range—2600m/s to 3400m/s—is significantly larger than the velocity difference on these two grains. For instance in Figure 3.4d, the velocity difference between grain 1 and grain 2 is approximately 20m/s; the difference between grain 3 and grain 4 is around 10m/s. Those differences are a small, but detectable portion—1.25% to 2.5%—of the full 800m/s velocity range. Secondly, it is possible for the velocities in orthogonal directions of two differently oriented grains to be identical. The more directions in which SAWs are propagated, the less likely this coincidence is to occur.

(a) Etched picture.   (b) EBSD.   (d) Velocity vector map.
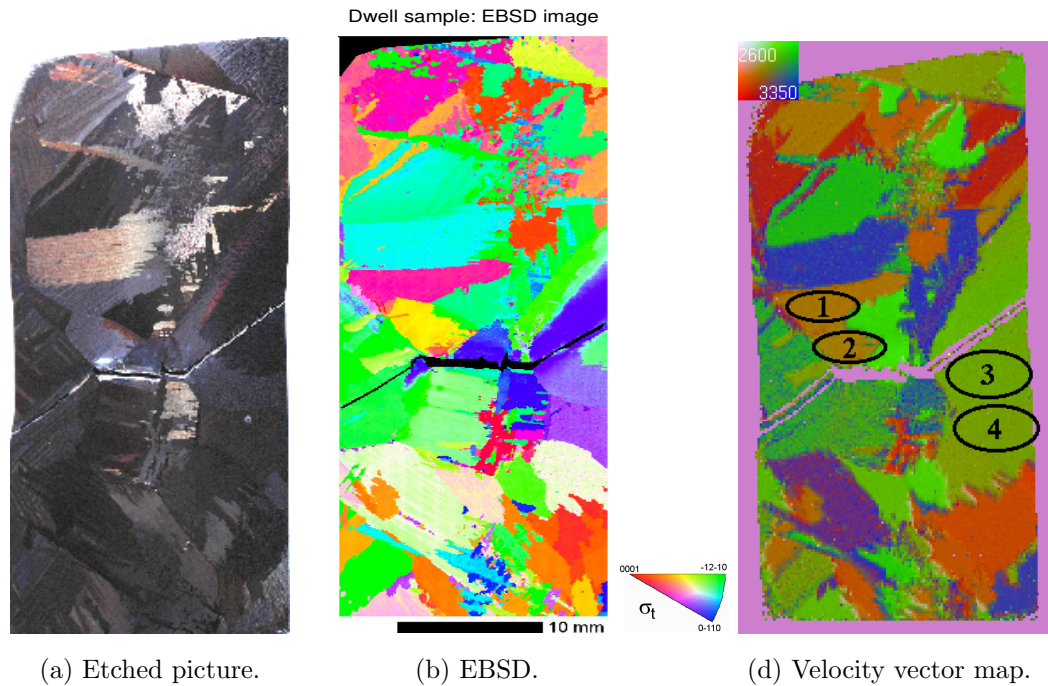
Figure 3.4: Close fit between etched picture (left), EBSD image (middle) and f-SRAS velocity vector map (right) on Ti-635.

Figure 3.5 shows the velocity maps of a Ti-685 sample obtained from propagating SAWs in three directions, separated by 60°, instead of two orthogonal directions. This method reduces the ambiguity of grain boundaries compared to the two directions velocity vector map. This vector map is presented by mapping to RGB (red, green, blue) colour space after normalising the velocity range be-

tween 2600m/s to 3300m/s. For example, for the basal plane SAWs travel at a relatively fast speed (approximately 3300m/s for this material) on all directions, the RGB value is close to [1,1,1]—white, for example the grain at the top of the sample—stands for [>=3300m/s, >=3300m/s, >=3300m/s] on three directions. If the colour is red, green or blue, it means the SAWs are slow on one direction but faster in the other two.
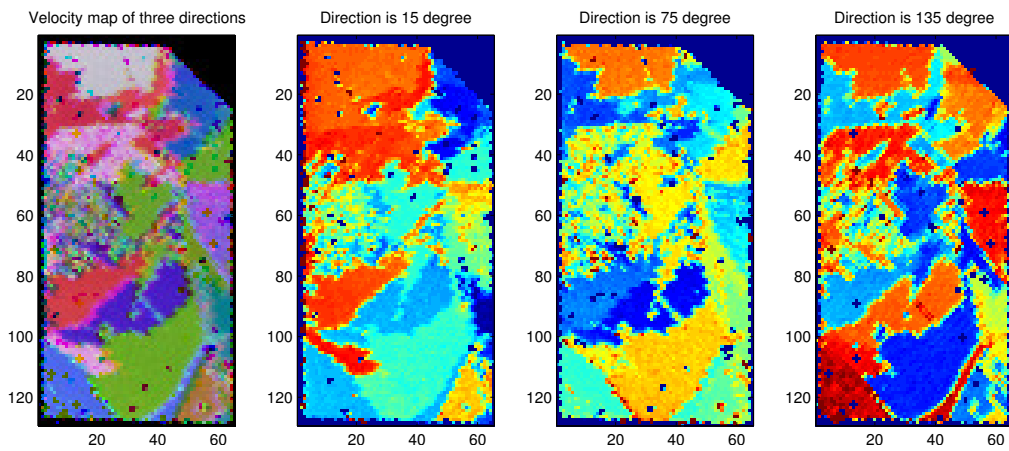
Figure 3.5: Velocity vector map of Ti-685 when SAWs propagate on three directions: 15°, 75° and 135°. Image size 30×18mm, pixel size 200μm. The vector map is presented by mapping to RGB colour after normalised in the velocity range 2600m/s to 3300m/s.

3.3.1 Scattered Distribution

Certain combinations of velocities of SAWs propagating in orthogonal directions are possible only in specific orientations on materials with hexagonal crystal structures. For example, if the velocities are both fast, it must be the basal plane (001). Any other combination of velocities—one slow and one fast—correspond to an orientation between the basal plane and plane (100). A scattered distribution is considered to reveal the relationship between orientation and SAW velocity of 2 directions in materials with hexagonal crystal structures.

Two k-SRAS images of a Ti-685 sample where the SAWs are propagated orthogonally are selected to perform this method, as illustrated in Figure 3.6. Bigger

grains will have more sample dots to form a cluster, as shown in Figure 3.6b. Two clusters of sample dots are chosen to find the corresponding grains. The bottom cluster of spots, shown in Figure 3.6b, corresponds to the grains where the SAWs are fast in one direction but slow in another; the top cluster corresponds to the grains where the SAWs are slow in both directions. If we use the points within each of the two clusters as masks for the original velocity data, we can discriminate and highlight the grains that these refer to, this is shown in Figure 3.6c and Figure 3.6d.

However we note that there are fewer obvious clusters in the scattered distribution than there are individual grains of unique orientation. This implies that the velocity information of only two orthogonal directions can only be used to determine certain special situations where the combinations of the two velocities are unique.

(a) Velocity maps on two orthogonal directions.

(b) Scattered distribution.

(c) The grains correspond to cluster A.

(d) The grains correspond to cluster B are added.
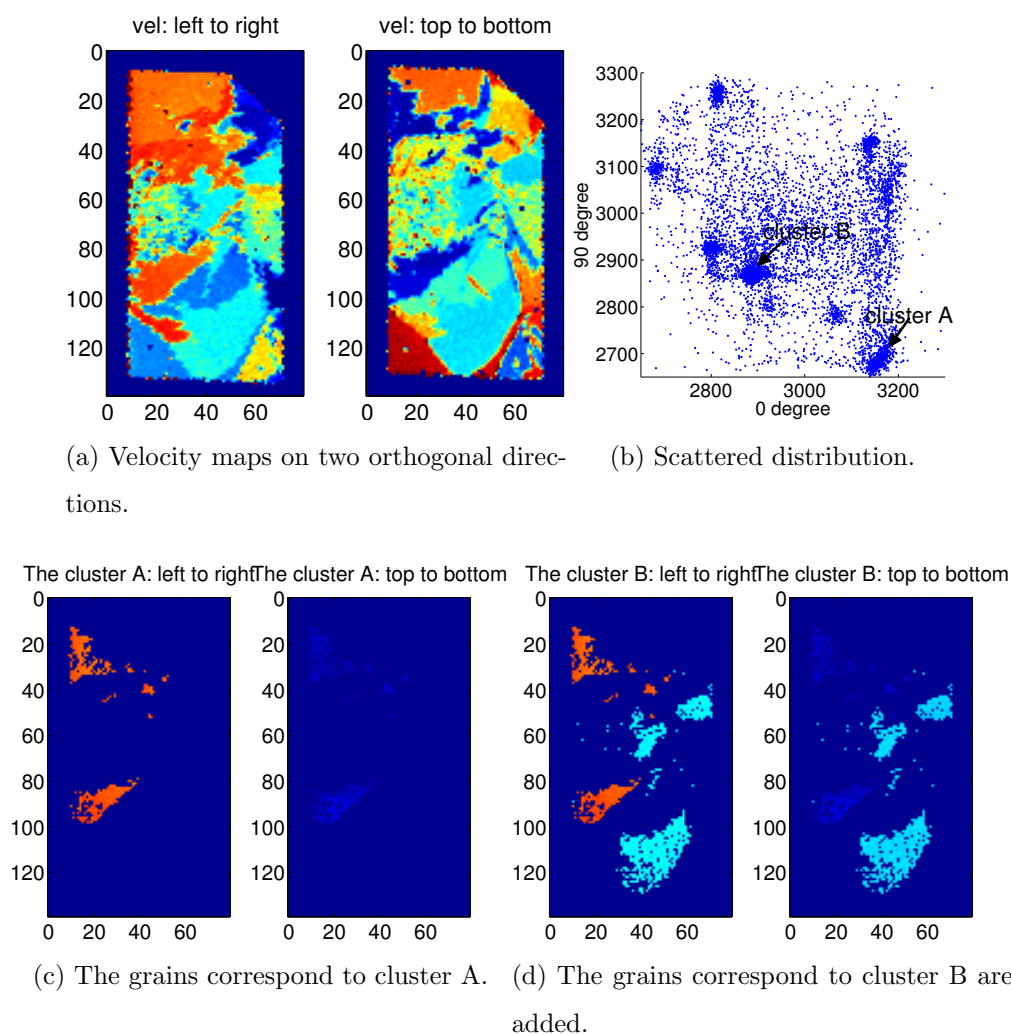
Figure 3.6: Scatter map of two directions velocities.

3.4 Comparison of K-SRAS and F-SRAS

In Figure 3.7 and Figure 3.8, Ti-6246 k-SRAS results are compared with f-SRAS results, which represent the velocity of SAWs propagating in two directions. The k-SRAS results were acquired at a fixed frequency of 164MHz (typical wavelengths 16–19μm) and f-SRAS at a fixed wavelength of 74.4μm (typical frequencies 35–41MHz). Figure 3.7 shows SAWs propagating from left to right, Figure 3.8 shows SAWs propagating from bottom to top. All the SRAS images are scanned at a

step size 250μm.
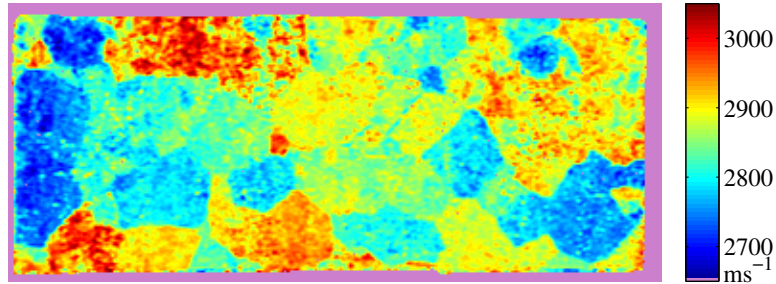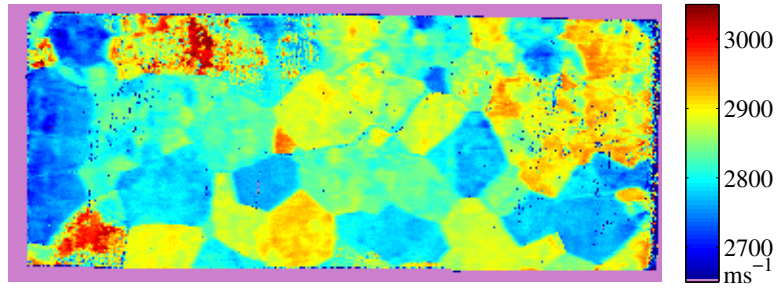
(a) K-SRAS.

(b) F-SRAS.

Figure 3.7: SAW velocity map of Ti-6246: k-SRAS (top) vs f-SRAS (bottom), SAWs propagating left to right. Image size 85×36mm, pixel size 250×250μm [27].

The spatial resolution of both variations of the SRAS technique is determined by the size of the grating pattern on the sample surface. As the two experimental setups (f-SRAS and k-SRAS) had very different grating sizes, the k-SRAS images have had a spatial low pass filter applied. This has been done to match the spatial resolution of the two sets of the results. Apart from differences in spatial resolution, both of the techniques have almost the same velocity distribution. The colour bars in the figures define the different SAW velocities, which for this alloy vary from 2650m/s (dark blue) to 3050m/s (dark red).
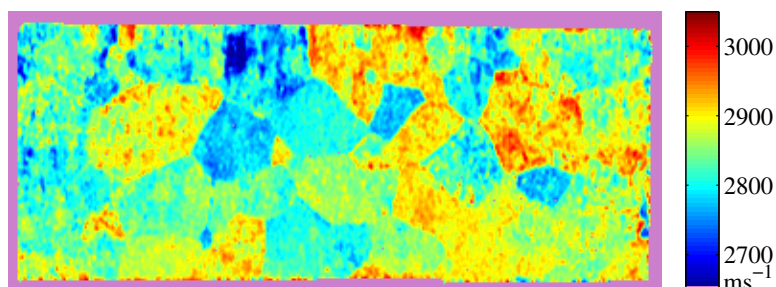
(a) K-SRAS.
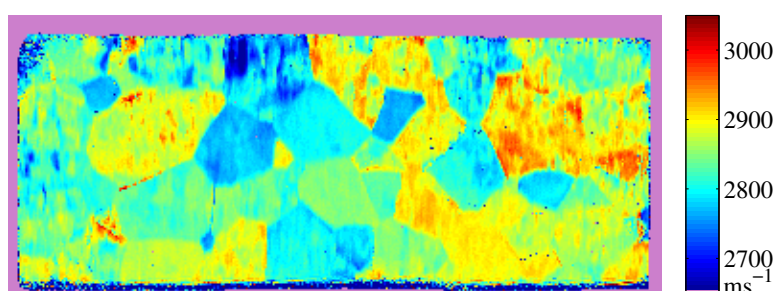
(b) F-SRAS.

Figure 3.8: SAW velocity map of Ti-6246: k-SRAS (top) vs f-SRAS (bottom), SAWs propagating bottom to top. Image size 85×36mm, pixel size $250\times250\mu$m [27].

The time required to scan a 341×145 pixel image of a 85×36mm sample using the k-SRAS technique is 75 minutes, which gives a scanning speed about 11 pixels/second. The same image acquired using f-SRAS takes 100 minutes, which is 9 pixels/second (including overheads for fly-back during raster scanning). Although in this case k-SRAS is marginally faster than f-SRAS, it should be noted that only two averages at each testing point were used when the k-SRAS data was collected, whereas 64 averages were used for f-SRAS.
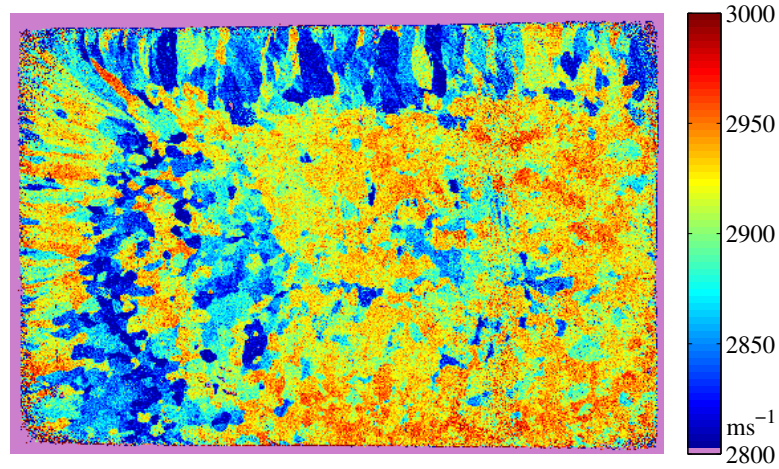
(a) K-SRAS.
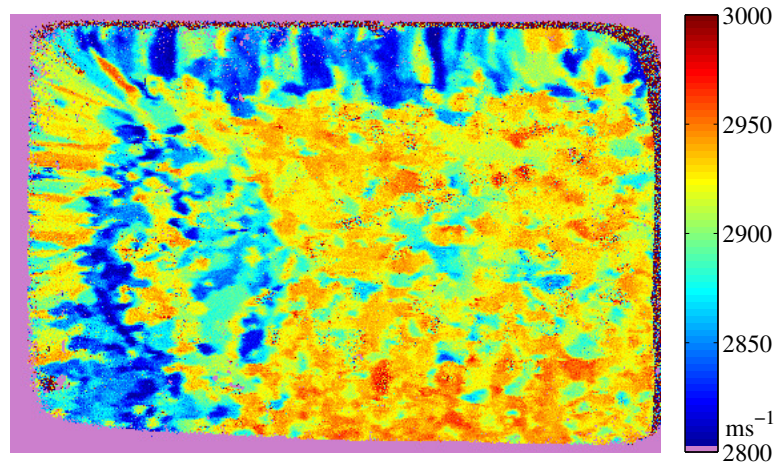
(b) F-SRAS.

Figure 3.9: SAW velocity map of aluminium: k-SRAS (top) vs f-SRAS (bottom), SAWs propagating left to right. Image size 61×41mm, pixel size 125×125μm [27].

SRAS can also be used on a material which has smaller grains, such as the 61×41mm aluminium sample shown in Figure 3.9 and Figure 3.10. The velocity at each point on this sample is calculated from a single laser shot for those images acquired using the f-SRAS technique. This means only one waveform has been collected at each sample point, with no data averaging. The acquisition time of each f-SRAS figure is more than 21 times faster than the time required for the equivalent k-SRAS image after the segmented memory technique was implemented.
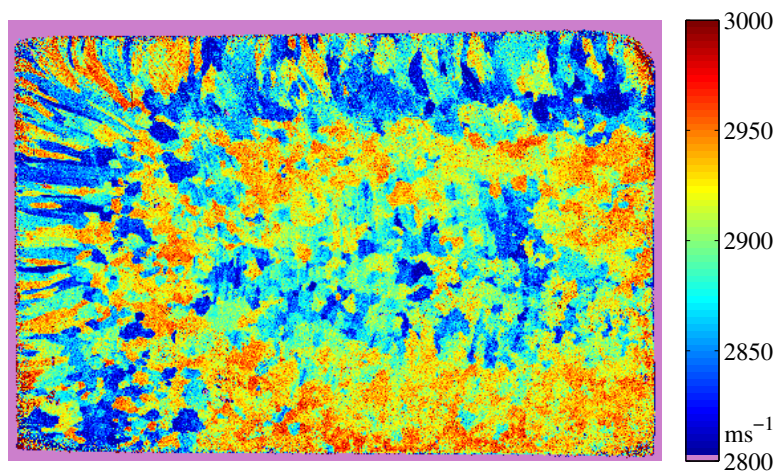
(a) *K*-SRAS.
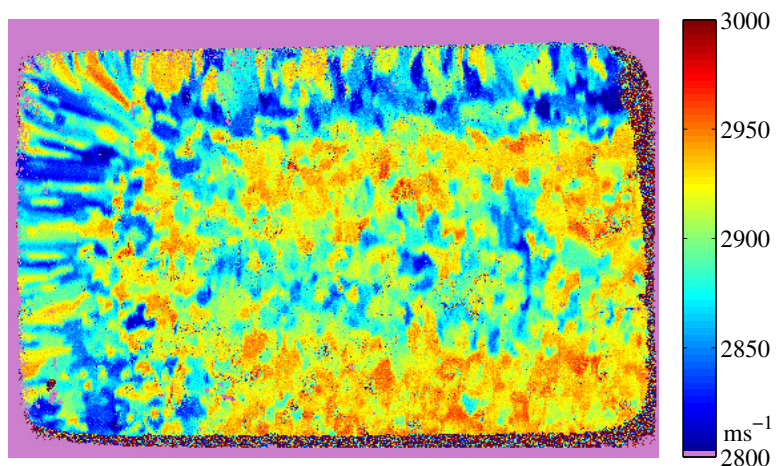
(b) F-SRAS.

Figure 3.10: SAW velocity map of aluminium: *k*-SRAS (top) vs f-SRAS (bottom), SAWs propagating bottom to top. Image size 61×41mm, pixel size 125×125μm [27].

3.5   SAW Velocity Results on a Single Grain

On single crystals, SRAS scans reveal the SAW velocity variation over 360° of propagation direction. Figure 3.11 presents such scan results of single crystal nickel and aluminium samples with known orientation.

The scans are taken on a random spot on the sample and starts with the SAWs

propagating in an arbitrary direction. A measurement is performed every time the sample is rotated by a certain interval, which is 5° on the nickel crystal (using the k-SRAS technique), and 1° on the aluminium crystal (using f-SRAS). The figures in the top row are presented as polar velocity spectra surface plots, whereby the radial distance from the centre of the square represents the SAW velocity in the direction of the radius. The colour indicates the intensity level of the received signal, where red is the strongest and blue represents the weakest; the scale of the images represents velocities varying from 0m/s in the centre of the square to 4000m/s in the centre of each edge. The recorded acoustic spectra are clearly visible.

Another way to present the experimental data of SRAS on single crystal is a velocity surface, which is plotted with the radius proportional to v. A Gaussian curve fit is applied to the velocity surface spectrum to determine the velocity with the largest signal component in every SAW propagation direction. These peak velocities are plotted as a velocity surface, shown in the bottom two figures.

The four figures represent the SAW velocity variation on one plane of two media in two different ways. Aluminium is a more highly isotropic material than nickel; its velocity change on this plane is 2972.5±12.5m/s, which is more than 10 times smaller than the velocity variation of nickel which is 2900±150m/s. Because the results of both media are demonstrated in the same scale, the aluminium results look considerably more circular.

(a) Nickel by k-SRAS.

(b) Aluminium by f-SRAS.

(c) Nickel by k-SRAS.

(d) Aluminium by f-SRAS.
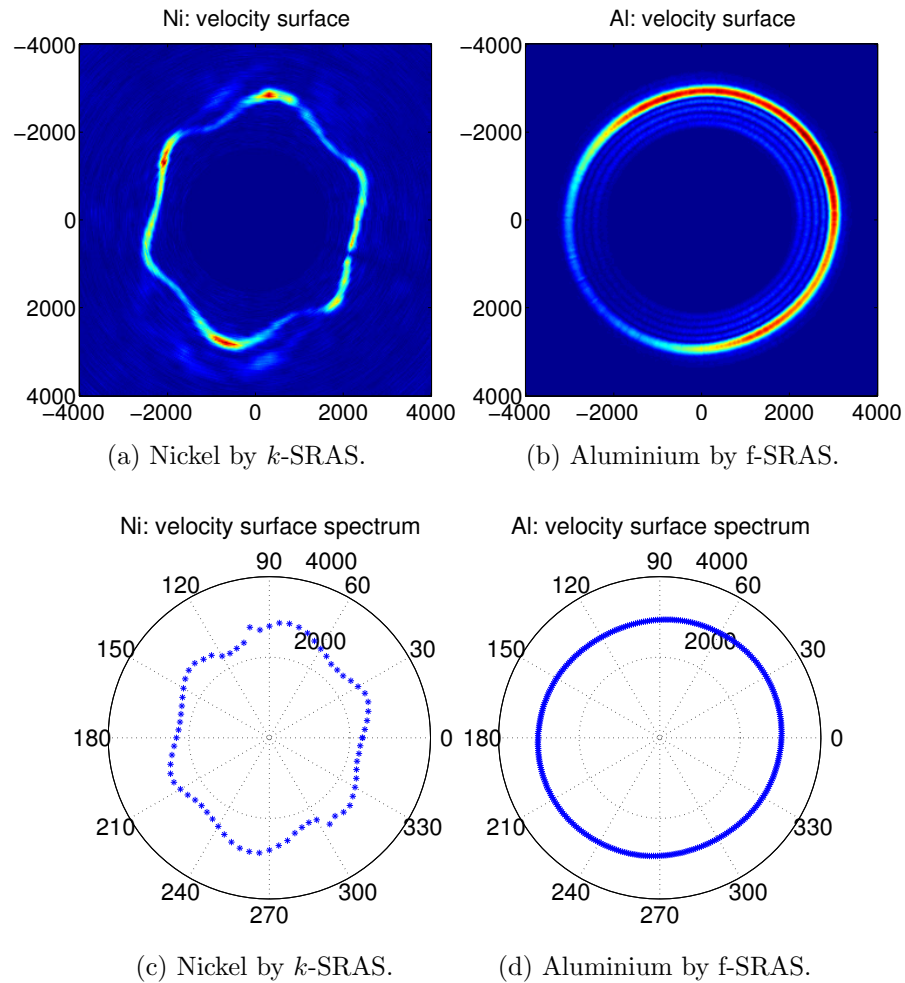
Figure 3.11: SAW velocity surface spectrum (top) and velocity surface (bottom) of single crystal nickel (left) and aluminium (right) and both are on plane (001) and in polar plots. The measurements are taken by k-SRAS and f-SRAS system respectively.

3.6 Discussion

The two variations of the SRAS technique—frequency spectrum SRAS and k-vector SRAS—have been compared in terms of their imaging capabilities. They are found to be broadly equivalent, once allowances have been made for differences in the spatial resolution due to the different sizes of the generation fringe patterns used.

The SAW velocity data acquired can be used to discern grains of different orientations, and it has been shown that by fusing velocity data from two or more propagation directions into vector or RGB colour maps, a significant amount of ambiguity about whether two arbitrary grains have the same orientation or not can be removed. A study of a scattered distribution of SAW velocities of a polycrystalline hexagonal titanium alloy has shown that certain combinations of velocities in orthogonal directions are unique enough to define grains of specific orientations—but that in many cases, more than two directions are required. Finally, the velocity and velocity surfaces of two materials with very different anisotropy factors are examined, using velocity data recorded in many different directions using the SRAS technique.

Chapter 4

Determining the Orientation from SRAS

In this chapter I will link the SAW velocity measurement that SRAS gives to the orientation of the crystal using the relation between SAW phase velocity, crystallographic orientations and the elastic constants of the medium as illustrated in Figure 4.1. They are complementary to each other; the third element can be deduced if the other two factors are known. In other words, based on the known elastic constants, the SAW velocity at the defined crystal cut and angle can be calculated. Furthermore, a model can be built if it covers the SAW velocity information of all crystallographic orientations. For convenience the Miller indices here are all noted as decimals between 0 and 1 rather than integers.

I will start by stating the wave equation for the general case before explaining the simplified case for an isotropic medium and then solving the general case. The solution developed has involved firstly solving the so-called forward problem of determining the SAW velocity from the elastic constants for a given orientation, and secondly solving the inverse problem of determining the orientation from SAW velocity measurements.
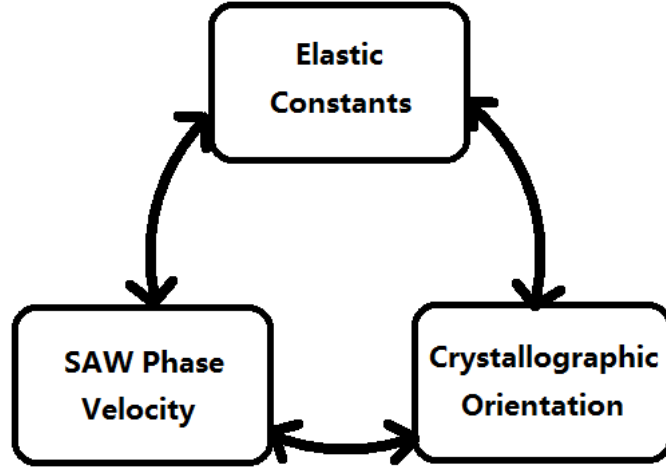
Figure 4.1: SAW phase velocity, crystallographic orientations and the elastic constants of the medium are related to and depend on each other.

The forward problem can be solved analytically (Chapter 4.1), however the inverse problem is ill conditioned and analytically intractable except for some trivial special cases. The technique developed here is to determine the orientation by fitting the measured data to the forward problem (Chapter 4.3 and Chapter 4.4); this technique is experimentally validated in Chapter 5.

4.1 Forward Model

4.1.1 The Wave Equation

In order to deduce the SAW velocity at a given orientation, it is necessary to solve the elastic wave equation with appropriate boundary conditions. As illustrated in Figure 4.2, x_1, x_2 and x_3 are three axes of Cartesian coordination system. When an elastic wave propagates in the medium, on the surface whose normal to the axis x_i has force exerted along the direction x_j, noted as T_{ij}. Thus, the equation of motion in medium is [29]

$$\rho \frac{\partial^2 u_j}{\partial t^2} = \frac{\partial T_{ij}}{\partial x_i}, \ (i, j = 1, 2, 3) \tag{4.1}$$

where ρ is the mass density of the media and u_i is the displacement along x_i direction.
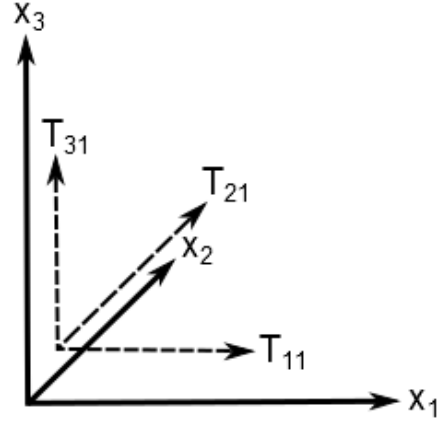
Figure 4.2: Stress and SAW in Cartesian coordination system. T_{11}, T_{21} and T_{31} are the stresses on the planes $x_1 = 0$, $x_2 = 0$, $x_3 = 0$, along the direction of x_1 axis. SAW propagates in the surface whose normal parallels to x_3 and $x_3 = 0$.

According to the tensor expression of Hooke's law, in the elastic medium stress T_{ij} and strain S_{kl} have the linear relationship

$$T_{ij} = c_{ijkl}S_{kl}, \ (i, j, k, l = 1, 2, 3) \tag{4.2}$$

where c_{ijkl} is the stiffness tensor containing the elastic constants. In anisotropic media, the stress of any certain direction is not only related to the strain of this direction, but also related to the strains in other directions.

At the same time, the relationship between S_{kl} and u_k is

$$S_{kl} = \frac{\partial u_k}{\partial x_l}, \ (k, l = 1, 2, 3). \tag{4.3}$$

Then substituting Equation 4.2 and 4.3 into Equation 4.1, gives

$$\rho\frac{\partial^2 u_j}{\partial t^2} = c_{ijkl}\frac{\partial^2 u_k}{\partial x_i \partial x_l}, \ (i, j, k, l = 1, 2, 3) \tag{4.4}$$

which is the wave equation for anisotropic elastic media.

In the following sections the distribution of waves on an isotropic medium will be used to explain the general principles and then the analysis will be extended to anisotropic media.

Figure 4.3 shows the coordinate system used to examining the propagation of SAWs on the infinite half space. These definitions go in the equation.
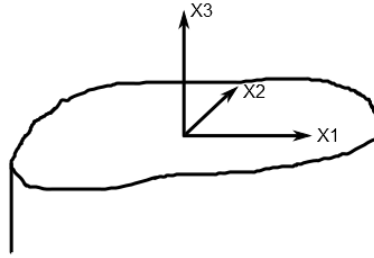
Figure 4.3: Definition of coordination system and the free surface.

The solution of wave equation 4.4 is

$$u_i = \alpha_i \exp\left\{ j\left[\omega t - \beta(l_1 x_1 + l_2 x_2 + l_3 x_3)\right]\right\}, \; (i = 1, 2, 3) \tag{4.5}$$

where l_1, l_2 and l_3 are the direction cosines of the propagation vectors, $\omega = 2\pi f$ is the angular frequency, $\beta = 2\pi/\lambda$ is the wave-number, and α_i are the eigenvectors of the corresponding eigenvalue. The solution defines the particle displacement and the wave type, whereas the eigenvectors are associated with the eigenvalues corresponding to the phase velocity of the wave.

Substituting Equation 4.5 into Equation 4.4, gives

$$\beta^2 c_{ijkl} l_i l_j \alpha_k - \rho \omega^2 \alpha_l = 0.$$

By dividing by β^2 on both sides of the above equation, it becomes

$$(c_{ijkl} l_i l_j - \rho v^2 \delta_{ik})\alpha_k = 0, \; (i, j, k, l = 1, 2, 3) \tag{4.6}$$

where $v^2 = \omega^2/\beta^2$, and $\delta_{ik} = \begin{cases} 1, \text{ when } i = k; \\ 0, \text{ when } i \neq k. \end{cases}$ According to the Equation 4.6, the phase velocity and particle displacement can be calculated for arbitrary directions (l_1, l_2, l_3) if the elastic constants c_{ijkl} are known.

Equation 4.6 has a nontrivial solution when its determinant is equal to zero:

$$\left| c_{ijkl} l_i l_j - \rho v^2 \delta_{ik} \right| = 0, \ (i, j, k, l = 1, 2, 3). \tag{4.7}$$

If one considers SAWs only here the propagation is confined to the directions in the plane which contain l_1 and l_2. The velocity of propagation of the SAWs is dependant on the values l_1 and l_2 which define the direction of propagation in the plane. In order to show the main features of Rayleigh waves the isotropic case where the propagation velocity does not depend on direction will be examined.

4.1.2   SAW on Isotropic Materials

In an isotropic material the elastic constants are [30]

$$\begin{bmatrix} c_{11} & c_{12} & c_{12} & 0 & 0 & 0 \\ c_{12} & c_{11} & c_{12} & 0 & 0 & 0 \\ c_{12} & c_{12} & c_{11} & 0 & 0 & 0 \\ 0 & 0 & 0 & c_{44} & 0 & 0 \\ 0 & 0 & 0 & 0 & c_{44} & 0 \\ 0 & 0 & 0 & 0 & 0 & c_{44} \end{bmatrix}$$

where $c_{44} = \frac{1}{2}(c_{11} - c_{12})$.

Assuming the SAW propagates along x_1 axis, hence $l_1 = 1$, $l_2 = 0$; substituting

c_{ijkl}, l_1 and l_2 into Equation 4.7 gives

$$\begin{vmatrix} \Gamma_{11} - \rho v^2 & \Gamma_{12} & \Gamma_{13} \\ \Gamma_{21} & \Gamma_{22} - \rho v^2 & \Gamma_{23} \\ \Gamma_{31} & \Gamma_{32} & \Gamma_{33} - \rho v^2 \end{vmatrix} = 0 \qquad (4.8)$$

where

$$\Gamma_{11} = c_{11} + c_{44}l_3^2,$$
$$\Gamma_{22} = c_{44}(1 + l_3^2),$$
$$\Gamma_{33} = c_{44} + c_{11}l_3^2,$$
$$\Gamma_{13} = \Gamma_{31} = (c_{11} - c_{44})l_3,$$
$$\Gamma_{12} = \Gamma_{21} = \Gamma_{23} = \Gamma_{32} = 0.$$

The determinant of Equation 4.7 after transformation is

$$(c_{44}l_3^2 + c_{44} - \rho v^2)^2(c_{11}l_3^2 + c_{11} - \rho v^2) = 0. \qquad (4.9)$$

The above is a cubic equation in l_3^2, therefore, there are three roots of l_3^2; Equation 4.9 gives six roots of l_3:

$$\begin{aligned} l_3^{(1)} &= -i(1 - v^2/v_t^2)^{1/2}, & l_3^{(4)} &= i(1 - v^2/v_t^2)^{1/2}, \\ l_3^{(2)} &= -i(1 - v^2/v_t^2)^{1/2}, & l_3^{(5)} &= i(1 - v^2/v_t^2)^{1/2}, \\ l_3^{(3)} &= -i(1 - v^2/v_l^2)^{1/2}, & l_3^{(6)} &= i(1 - v^2/v_l^2)^{1/2} \end{aligned} \qquad (4.10)$$

where $v_t = \sqrt{c_{44}/\rho}$ and $v_l = \sqrt{c_{11}/\rho}$, being the velocities of transverse and longitudinal bulk waves respectively in an isotropic medium.

According to the characteristics of SAWs inside the medium where $x_3 \to -\infty$, the particle displacement must be zero. Three of the roots in Equation 4.10, l_3^4, l_3^5 and l_3^6, result in the displacements of waves approaching infinity when $x_3 \to -\infty$ after being substituted into Equation 4.5. Therefore, those roots which have positive imaginary parts are discarded.

Substituting the three roots with negative imaginary parts into Equation 4.6, each root has a set of corresponding normalised eigenvectors such that

$$
\begin{aligned}
&\alpha_1^{(1)} = 0, \quad \alpha_1^{(2)} = i(v_t/v)(1 - v^2/v_t^2)^{1/2}, \quad \alpha_1^{(3)} = v_l/v, \\
&\alpha_2^{(1)} = 1, \quad \alpha_2^{(2)} = 0, \qquad\qquad\qquad\qquad \alpha_2^{(3)} = 0, \\
&\alpha_3^{(1)} = 0, \quad \alpha_3^{(2)} = v_t/v, \qquad\qquad\qquad\quad \alpha_3^{(3)} = -i(v_l/v)(1 - v^2/v_l^2)^{1/2}.
\end{aligned}
\tag{4.11}
$$

Furthermore, the solutions of the wave equation must also satisfy the boundary conditions, therefore, no traction exists at $x_3 = 0$,

$$
T_{3j} = c_{3jkl}\partial u_k/\partial x_l = 0, \text{ for } j = 1, 2, 3.
\tag{4.12}
$$

This boundary condition in Equation 4.12 limits the available solutions to the wave equation 4.4 to solutions corresponding to SAWs. However, based on the linear differential equation, the solution will be

$$
u_i = \sum_{n=1}^{3} C_n \alpha_i^{(n)} \exp[-j\beta l_3^{(n)} x_3]\exp[j(\omega t - \beta l_1 x_1)]
\tag{4.13}
$$

where C_n are the weighting factors, which satisfy both the determinant of the wave equation (4.4) and the boundary conditions (4.12).

By substituting the solution 4.13 and the elastic constants of the isotropic media into Equation 4.12, three equations are given as

$$
\begin{aligned}
&(\alpha_3^{(2)} + \alpha_1^{(2)} l_3^{(2)})C_2 + (\alpha_3^{(3)} + \alpha_1^{(3)} l_3^{(3)})C_3 = 0 \\
&l_3^{(1)} C_1 = 0 \\
&(c_{11}\alpha_3^{(2)} l_3^{(2)} + c_{12}\alpha_1^{(2)})C_2 + (c_{11}\alpha_3^{(3)} l_3^{(3)} + c_{12}\alpha_1^{(3)})C_3 = 0.
\end{aligned}
\tag{4.14}
$$

If the determinant of the system of linear equations 4.14 has a nontrivial solution,

its determinant must equal zero:

$$
\begin{vmatrix}
0 & \alpha_3^{(2)} + \alpha_1^{(2)}l_3^{(2)} & \alpha_3^{(3)} + \alpha_1^{(3)}l_3^{(3)} \\
l_3^{(1)} & 0 & 0 \\
0 & c_{11}\alpha_3^{(2)}l_3^{(2)} + c_{12}\alpha_1^{(2)} & c_{11}\alpha_3^{(3)}l_3^{(3)} + c_{12}\alpha_1^{(3)}
\end{vmatrix}
$$
$$
= l^{(1)}\left[(\alpha_3^{(2)} + \alpha_1^{(2)}l_3^{(2)})(c_{11}\alpha_3^{(3)}l_3^{(3)} + c_{12}\alpha_1^{(3)}) - (\alpha_3^{(3)} + \alpha_1^{(3)}l_3^{(3)})(c_{11}\alpha_3^{(2)}l_3^{(2)} + c_{12}\alpha_1^{(2)})\right]
$$
$$
= 0.
$$
$$(4.15)$$

Two solutions of 4.15 are derived after substituting 4.10 and 4.11 into it, and are given by

$$
l_3^{(1)} = i(1 - v^2/v_t^2)^{1/2} = 0 \tag{4.16}
$$

where $v = v_t$, and $C_2 = C_3 = 0$. The displacements of this solution are parallel to the free surface, the amplitude of the wave is constant and does not vary with the depth beneath the surface, hence it is defined as a transverse bulk wave. Also,

$$
\left[2 - (v/v_t)^2\right]^2 = 4\left[1 - (v/v_t)^2\right]^{1/2}\left[1 - (v/v_l)^2\right]^{1/2} \tag{4.17}
$$

where v is solved so that C_2, C_3 are then deduced by Equation 4.15; hence, the displacements are:

$$
u_1 = C\left[\exp(j\beta l_3^{(3)}x_3) - A\exp(j\beta l_3^{(2)}x_3)\right]\exp\left[j\beta(x_1 - vt)\right]
$$
$$
u_2 = 0
$$
$$
u_3 = -jC\left[1 - v^2/v_t^2\right]^{1/2}\left[\exp(j\beta l_3^{(3)}x_3) - \tfrac{1}{A}\exp(j\beta l_3^{(2)}x_3)\right]\exp\left[j\beta(x_1 - vt)\right]
$$
$$(4.18)$$

where $A = (1 - v^2/v_l^2)^{1/4}(1 - v^2/v_t^2)^{1/4}$. The solution of Equation 4.18 is a wave which propagates along the half space boundary and is known as a Rayleigh wave [31]. The particle displacement of the Rayleigh wave is made up of two components: one is parallel to the wave propagation direction x_1, and the other is perpendicular to the free surface with a phase difference $90°$ to the first com-

ponent. For this reason the particle movement is elliptical; the amplitude of the displacements decrease exponentially with the depth of the free surface. The variation of the displacements of vertical (red line) and longitudinal (blue line) waves are presented in Figure 4.4. The energy of the SAW is predominantly concentrated within a range of 1–2 SAW wavelengths below the free surface.
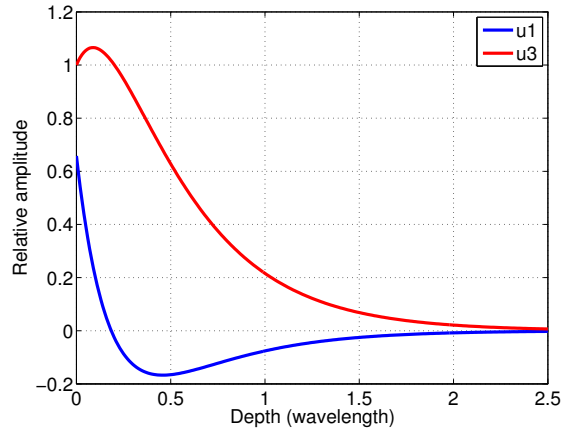
Figure 4.4: The displacements of vertical (u_3) and longitudinal (u_1) waves decrease exponentially with the depth beneath the free surface.

4.1.3 SAW on Anisotropic Materials

Due to the nature of anisotropic media the SAW phase velocity is dependent on the medium composition, and both crystal plane and angle. The procedure for solving the SAW phase velocity is similar to that used for isotropic materials, but of course the variables when solving for anisotropic materials are more complicated. Beginning again from Equation 4.8,

$$\Gamma_{ik} = c_{i1k1}l_1^2 + c_{i2k2}l_2^2 + c_{i3k3}l_3^3 + (c_{i2k3} + c_{i3k2})l_2l_3 + (c_{i1k3} + c_{i3k1})l_1l_3 \\ + (c_{i1k2} + c_{i2k1})l_1l_2, \ (i, k = 1, 2, 3) \tag{4.19}$$

Because Γ_{ik} has symmetry where $\Gamma_{23} = \Gamma_{32}$, $\Gamma_{13} = \Gamma_{31}$ and $\Gamma_{12} = \Gamma_{21}$, they can be expressed according to their crystal systems as follows:

1. Cubic

$$\Gamma_{11} = c_{11}l_1^2 + c_{44}l_2^2 + c_{44}l_3^2$$
$$\Gamma_{22} = c_{44}l_1^2 + c_{11}l_2^2 + c_{44}l_3^2$$
$$\Gamma_{33} = c_{44}l_1^2 + c_{44}l_2^2 + c_{11}l_3^2$$
$$\Gamma_{12} = (c_{12} + c_{44})l_2l_3$$
$$\Gamma_{13} = (c_{12} + c_{44})l_1l_3$$
$$\Gamma_{23} = (c_{12} + c_{44})l_1l_2$$

2. Hexagonal

$$\Gamma_{11} = c_{11}l_1^2 + c_{66}l_2^2 + c_{44}l_3^2$$
$$\Gamma_{22} = c_{66}l_1^2 + c_{11}l_2^2 + c_{44}l_3^2$$
$$\Gamma_{33} = c_{44}l_1^2 + c_{44}l_2^2 + c_{33}l_3^2$$
$$\Gamma_{12} = (c_{13} + c_{44})l_2l_3$$
$$\Gamma_{13} = (c_{13} + c_{44})l_1l_3$$
$$\Gamma_{23} = (c_{11} - c_{66})l_1l_2$$

3. Tetragonal

$$\Gamma_{11} = c_{11}l_1^2 + c_{66}l_2^2 + c_{44}l_3^2$$
$$\Gamma_{22} = c_{66}l_1^2 - c_{11}l_2^2 + c_{44}l_3^2$$
$$\Gamma_{33} = c_{44}l_1^2 + c_{44}l_2^2 + c_{33}l_3^2$$
$$\Gamma_{12} = (c_{13} + c_{44})l_2l_3$$
$$\Gamma_{13} = (c_{13} + c_{44})l_1l_3$$
$$\Gamma_{23} = (c_{12} + c_{66})l_1l_2$$

4. Triclinic

$$\Gamma_{11} = c_{11}l_1^2 + c_{66}l_2^2 + c_{44}l_3^2 + 2c_{14}l_2l_3$$
$$\Gamma_{22} = c_{66}l_1^2 + c_{11}l_2^2 + c_{44}l_3^2 - 2c_{14}l_2l_3$$
$$\Gamma_{33} = c_{44}l_1^2 - c_{44}l_2^2 + c_{33}l_3^2$$
$$\Gamma_{12} = (c_{13} + c_{44})l_2l_3 + c_{14}(l_1^2 - l_2^2)$$
$$\Gamma_{13} = (c_{13} + c_{44})l_1l_3 + 2c_{14}l_1l_2$$
$$\Gamma_{23} = (c_{11} - c_{66})l_1l_2 + 2c_{14}l_1l_3$$

5. Orthorhombic

$$\Gamma_{11} = c_{11}l_1^2 + c_{66}l_2^2 + c_{55}l_3^2$$
$$\Gamma_{22} = c_{66}l_1^2 + c_{22}l_2^2 + c_{44}l_3^2$$
$$\Gamma_{33} = c_{56}l_1^2 + c_{44}l_2^2 + c_{33}l_3^2$$
$$\Gamma_{12} = (c_{23} + c_{44})l_2l_3$$
$$\Gamma_{13} = (c_{13} + c_{44})l_1l_3$$
$$\Gamma_{23} = (c_{12} + c_{65})l_1l_2$$

l_1 and l_2 are defined by the direction of propagation. The Equation 4.8 may be considered as a cubic equation with variable l_3^2 and parameter v^2, and therefore for each v^2 there are six roots of 4.8. For anisotropic media, they are generally complex roots given by

$$Re[l_3^{(1)}] \pm jIm[l_3^{(1)}]$$
$$Re[l_3^{(2)}] \pm jIm[l_3^{(2)}]$$
$$Re[l_3^{(3)}] \pm jIm[l_3^{(3)}].$$

In a similar fashion to the case of isotropic media, although in this case the roots have a negative imaginary part and decay into the material

$$l_3^{(1)} = Re[l_3^{(1)}] - jIm[l_3^{(1)}]$$
$$l_3^{(2)} = Re[l_3^{(2)}] - jIm[l_3^{(2)}]$$
$$l_3^{(3)} = Re[l_3^{(3)}] - jIm[l_3^{(3)}]$$

match the boundary conditions. Substituting the three roots into Equation 4.6, the eigenvectors of each root $\alpha_i^{(n)}$, $(i, n = 1, 2, 3)$ can be found.

Additionally, the solution must satisfy the boundary conditions 4.12. Again nontrivial solutions exist, thus the determinant of the coefficient is given by

$$d_{mn} = c_{m3kl}\alpha_k^{(n)}l_l^{(n)} = 0, \text{ with } l_1^{(n)} \equiv l_1, \; l_2^{(n)} \equiv l_2. \tag{4.20}$$

The displacements along the three Cartesian axes can be calculated when you have a known: velocity, three lower-half space roots, and its corresponding eigenvectors and weighting factors being

$$u_i = \sum_{n=1}^{3} C_n \alpha_i^{(n)} \exp[-j\beta l_3^{(n)} x_3] \exp[j(\omega t - \beta l_1 x_1 - \beta l_2 x_2)] \tag{4.21}$$

Farnell [4] illustrated how to use iterative search procedures to achieve an appropriate v value using a computer algorithm. The SAW phase velocity is varied to find the value of v which satisfies the Equation 4.20.

Even though the determinant can be complex in order to satisfy the boundary conditions it is necessary for both real and imaginary parts to approach zero simultaneously. It is now believed [4] [5] that this can be achieved in all combinations of planes and propagation directions. In some cases other modes also exist where the determinant does not vanish but becomes small. In these cases, as described by Farnell [4], the wave attenuates along the direction of propagation and is not a true surface wave. However, if the attenuation is small the behaviour can appear like a normal surface wave. These waves are called PSAWs and exist on specific planes and directions.

4.1.4   Calculation of 'Dominant' Modes

To determine the measured velocity the magnitude of the determinant (Equation 4.20) is plotted against possible velocities. The approximate formula of Rayleigh

wave velocities on isotropic media is given [31] as

$$v = \frac{0.87 + 1.12\sigma}{1 + \sigma} v_t \tag{4.22}$$

where σ is the Poisson's ratio of the material and v_t is the velocity of the transverse bulk wave. This formula gives a useful indication of the velocity searching range of isotropic and anisotropic media and it can be adjusted according to the specific conditions of different materials. As the Poisson's ratio varies between 0–0.5, the phase velocity varies from $0.87v_t$ to $0.96v_t$. Therefore, the velocity searching range has to be larger than this. The minima of the curve when the determinant equals or approaches zero represent the possible wave modes.

A curve of magnitude of determinant (Equation 4.20) vs. velocity is plotted in Figure 4.5; the location of the troughs of the curve indicate the SAW velocities, which lead the determinant infinitesimally close to zero and satisfy the boundary conditions. The three minima shown in Figure 4.5 correspond to the wave 'modes' which might exist. The determinant value is calculated at approximately every 7m/s; larger intervals may cause the absence of troughs, hence miss possible wave modes.
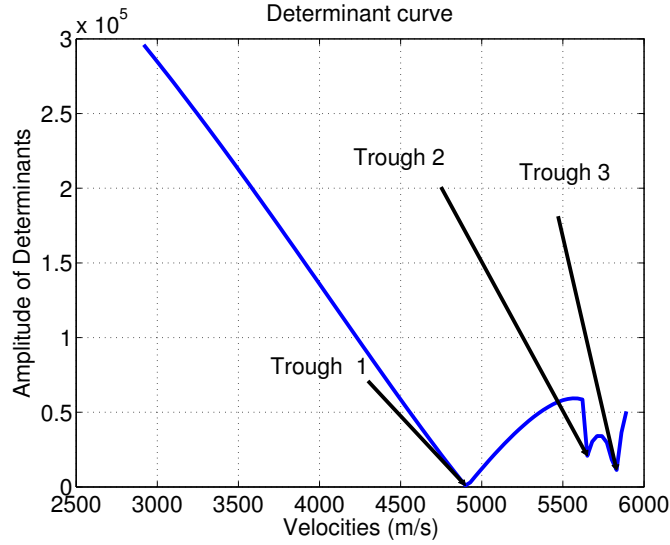
Figure 4.5: Curve of determinants vs. velocities of arbitrary direction on plane (001) of silicon with $\rho = 2.328\text{gm/cm}^3$, $c_{11} = 165\text{GPa}$, $c_{12} = 64\text{GPa}$ and $c_{44} = 79.2\text{GPa}$ [32].

The displacements along three Cartesian axes are calculated by Equation 4.21. For an arbitrary angle on a free surface the vertical displacement is along the x_3 axis and the longitudinal and transverse displacements are the sum of the projections of the displacements along x_1 and x_2 axes respectively. The displacements of those directions establish the wave mode oscillation pattern and define the wave type.

In our SRAS systems, the Rayleigh waves are generated efficiently by thermoelastic expansion [13], hence, when considering surface wave generation, the displacements on the longitudinal and vertical directions are the most significant. The knife-edge detector which is implemented in both SRAS systems, translates the slope of surface to the spatial displacement and so it is sensitive to the out-of-plane displacements of SAW. Even though only the displacement along the x_3 axis is detectable by the knife-edge detector, the laser generated force in the longitudinal direction is significant for driving the wave propagation. In the model, by considering the displacements in these two directions, the mode is ranked according to

$$\vec{u}_{\text{total displacement}} = \vec{u}_{\text{vertical}} + \vec{u}_{\text{longitudinal}} \tag{4.23}$$

which defines the 'dominant' mode or the one that is most likely observed.

Figure 4.6 shows an example of multiple modes calculation on silicon (001) plane. The top left figure displays four modes located within the velocity searching range. Not all the wave modes are continuous, for example, one mode in this figure only appears at particular angles. It may be because the mode disappears and is not present between those angles, or that the interval of the determinant curve calculation is not small enough and so the minimum was missed. The modes are named according to the velocity at each angle, and are presented in different colours from lowest to higher velocities by blue, green, red and cyan respectively. The slowest mode, which is the true SAW, agrees with Farnell's research in Figure 4.6d [4].

The top middle figure shows the displacement versus the angle and mode order. The mode which has largest displacement according to the second figure is plotted as in the top right graph; it is defined as the 'dominant' mode, which is the wave mode most likely to be observed. It is noteworthy to mention that the unit of calculated velocity in this thesis is m/s, which does not correspond to the unit of elastic constants GPa and density gm/cm^3, which are the units given by some references herein.

(a) Possible modes.   (b) Displacements of modes.   (c) The 'dominant' mode.

(d) Farnell's result.
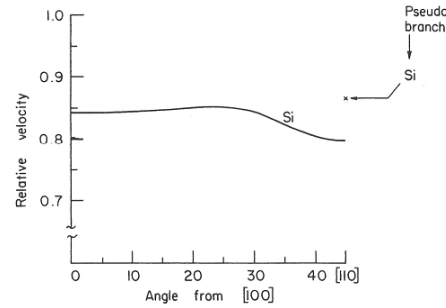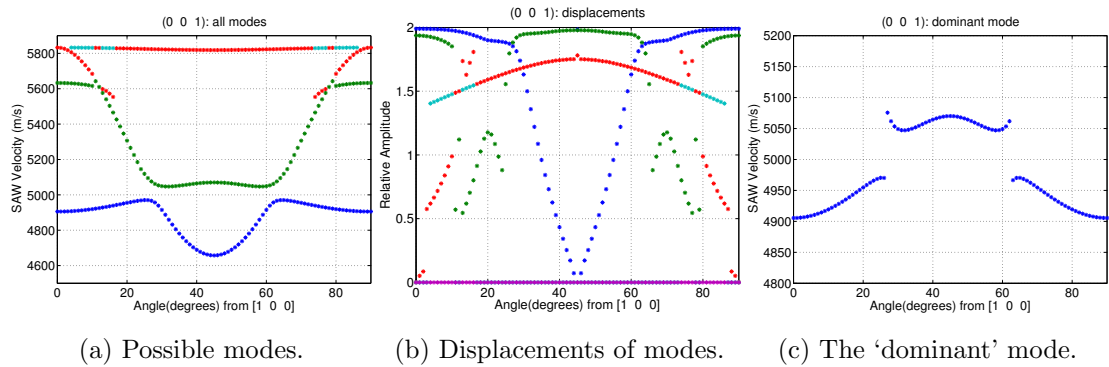
Figure 4.6: Calculated modes (top left) and its corresponding displacements (top middle) on plane (001) of silicon. The top right graph displayed the SAW mode which has the largest displacements. Bottom figure is the calculated velocity curve by Farnell [4].

PSAWs appear at certain angles of particular crystal planes on the free surface of anisotropic materials. They propagate along the surface medium, which then gradually degenerates into a bulk wave and penetrates into the depth of the medium. In the above calculations, because the 'dominant' modes are ranked according to the largest displacements, which are the sum of vertical and longitudinal terms, PSAWs are regarded as primary if their displacement is larger than the SAW's, as at the angles between 28° and 63° in Figure 4.6c.

4.1.5 Rotation of Coordination System
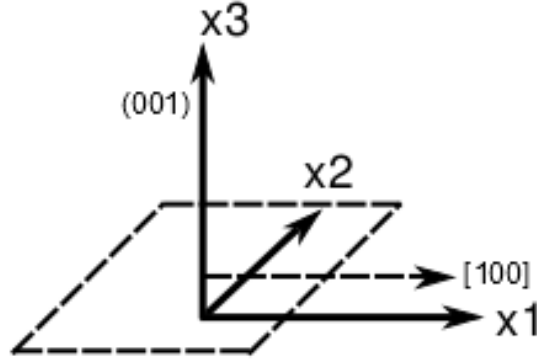
Figure 4.7: Rotation of plane and reference direction in the coordination system.

Section 4.1.4 has described how to calculate SAW phase velocities on plane (001), where the primitive vectors are parallel to the axes of the coordinate system as demonstrated in Figure 4.7. The model is based on the left-hand Cartesian coordination system. For the case of an arbitrary plane, the elastic constants are rotated about the rotation matrix from plane (001) to the desired plane before the iterative search procedures:

$$c_{\text{desired}} = c_{\text{reference}} \times R^{\mathsf{T}} \tag{4.24}$$

where R is the rotation matrix (see Appendix C), and both c_{desired} and $c_{\text{reference}}$ are 4th-order tensors. The reference direction [100] on plane (001) is also processed using this method. For example, the rotation matrix of plane (110) is

$$R = \begin{bmatrix} \frac{1}{2} & -\frac{1}{2} & \frac{1}{\sqrt{2}} \\ -\frac{1}{2} & \frac{1}{2} & \frac{1}{\sqrt{2}} \\ -\frac{1}{\sqrt{2}} & -\frac{1}{\sqrt{2}} & 0 \end{bmatrix}$$

Thus:

$$P_{(110)} = (0 \ \ 0 \ \ 1) \times R^\mathsf{T} = (0 \ \ 0 \ \ 1) \times \begin{bmatrix} \frac{1}{2} & -\frac{1}{2} & -\frac{1}{\sqrt{2}} \\ -\frac{1}{2} & \frac{1}{2} & -\frac{1}{\sqrt{2}} \\ \frac{1}{\sqrt{2}} & \frac{1}{\sqrt{2}} & 0 \end{bmatrix} = (1 \ \ 1 \ \ 0)$$

and the reference vector on plane (110) is

$$V_{(110)} = V_{\text{reference}} \times R^\mathsf{T} = [1 \ \ 0 \ \ 0] \times \begin{bmatrix} \frac{1}{2} & -\frac{1}{2} & -\frac{1}{\sqrt{2}} \\ -\frac{1}{2} & \frac{1}{2} & -\frac{1}{\sqrt{2}} \\ \frac{1}{\sqrt{2}} & \frac{1}{\sqrt{2}} & 0 \end{bmatrix} = \begin{bmatrix} \frac{1}{2} & -\frac{1}{2} & -\frac{1}{\sqrt{2}} \end{bmatrix}.$$

This rotation method makes plane (001) rotate to the desired plane normal via the shortest path. The model allows one to calculate the velocity surface of planes as a function of orientation determined by the normal to the plane and a reference direction within the plane.

4.1.6 Symmetry of Cubic System

Because of the structural symmetry of cubic crystals, a plot of SAW velocities on plane (hkl) may be rotated by a determinable angle to give that of a mirror of plane (khl). The velocity surfaces of the two planes do not share a common plane of symmetry and so can not been superimposed.

Assumes plane (hkl) has reference direction noted as

$$\begin{aligned} V_{(hkl)} &= V_{\text{reference}} \times R_{hkl}^\mathsf{T} \\ &= [1 \ \ 0 \ \ 0] \times R_{hkl}^\mathsf{T} \\ &= \begin{bmatrix} k^2 \times (1 - \cos\theta) + \cos\theta & -kh \times (1 - \cos\theta) & -h \times \sin\theta \end{bmatrix} \end{aligned}$$

where $\theta = \angle([001], [hkl])$. The reference direction of plane (khl) is similarly avail-

able

$$V_{(khl)} = \left[h^2 \times (1 - \cos\phi) + \cos\phi \quad - kh \times (1 - \cos\phi) \quad - k \times \sin\phi \right]$$

where $\phi = \angle([001], [khl])$ and $\theta = \phi$. If plane (khl) rotates via the shortest route to the position of plane (hkl), its new reference direction V'_{khl}, which must be parallel to plane (hkl) is

$$
\begin{aligned}
V'_{(khl)} &= V_{(khl)} \times (R'_{khl})^{\mathsf{T}} \\
&= \left[h^2 \times (1 - \cos\phi) + \cos\phi \quad - kh \times (1 - \cos\phi) \quad - k \times \sin\phi \right] \times (R'_{khl})^{\mathsf{T}}
\end{aligned}
$$

where $\psi = \angle([khl], [hkl])$. The angle between V_{hkl} and V'_{khl} is always

$$\delta = \arcsin(V_{(hkl)} \cdot V'_{(khl)}) = 90°$$

where both h and k are positive real numbers with $h < k$, the angle δ will be negative. Consequently, the velocity surface of plane (hkl) and (khl) ($l = 1$ in the model) will be identical if the mirror reflection of latter is rotated 90° counter-clockwise.

An example of planes (0.25 0.1 1) and (0.1 0.25 1), of the face centred cubic lattice of nickel, are given in Figure 4.8. Plane (0.1 0.25 1) has been flipped and rotation 90°, and matches plane (0.25 0.1 1) in Figure 4.8c.

(a) Plane (0.25 0.1 1).   (b) Plane (0.1 0.25 1).   (c) Planes overlap after one is rotated and flipped.
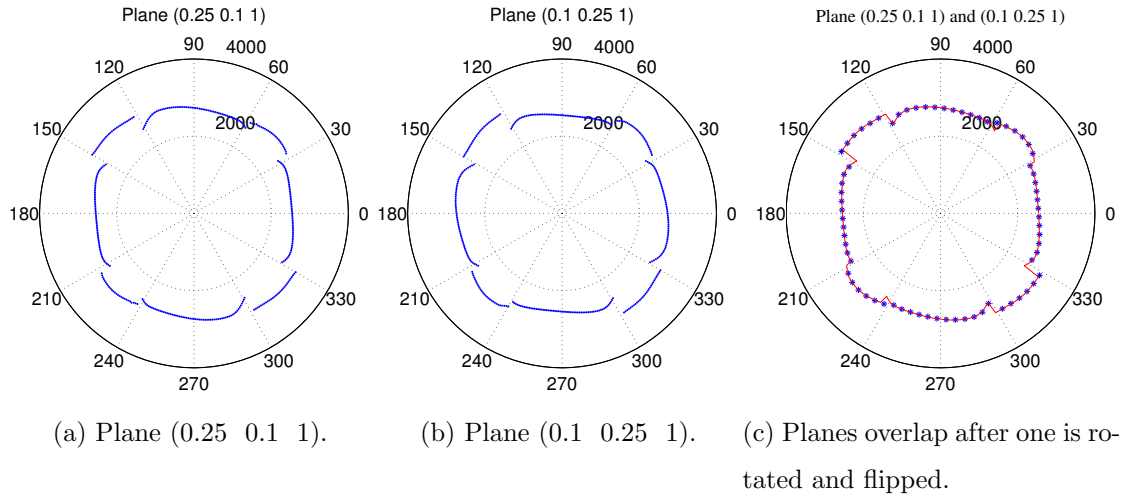
Figure 4.8: SAW on plane (0.25 0.1 1) and (0.1 0.25 1) of nickel are on the left; plane (0.1 0.25 1) has been flipped and rotation 90°, and matches plane (0.25 0.1 1). They are calculated based on the elastic constants $c_{11} = 247$GPa, $c_{12} = 153$GPa, $c_{44} = 122$GPa and $\rho = 8.912$gm/cm^3 [32].

4.2 SAW Model of Specific Materials

4.2.1 Cubic Structure

Because of the symmetry of the cubic crystal structure, only 1/48 of planes of a sphere are needed to describe all the SAW velocity surfaces of a cubic crystal, and the remaining planes are repetitions of this information. The planes have normals in the area between [001], [011], [101] and [111], which is shown as dots in Figure 4.9. In other words, only the planes (hkl) and (khl) (h, $k \in [0, 1]$, and $l = 1$) are calculated; the symmetry relationship between these two types of planes was shown in the previous section. The angle between adjacent planes is approximately 2.25° and the velocities on each plane are calculated at one degree intervals.
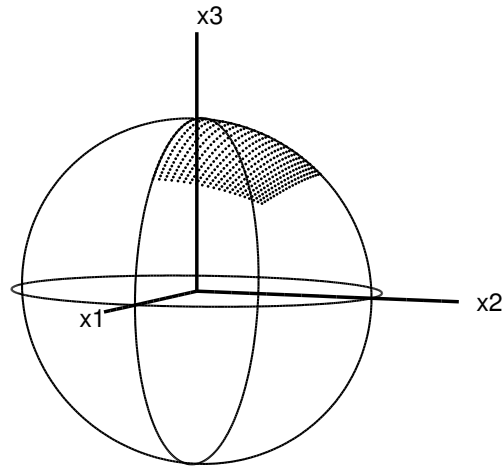
Figure 4.9: The area with dots is where the normal of the calculated planes are.

4.2.2   Aluminium

Aluminium is a face-centred cubic crystal. Aluminium has the advantage of light weight, also high specific strength, better than some alloys of steel, and it has become one of the most commonly used metals in industry. In the manufacturing and aviation industries, aluminium is often an excellent structural material. The parameters of aluminium used for the model are $c_{11} = 107.3$GPa, $c_{12} = 60.9$GPa, $c_{44} = 28.3$GPa and $\rho = 2.699$gm/cm^3 [33].

SAW on typical planes : (001), (011) and (111)

The previous section demonstrated that the modes of SAWs are calculated by searching the troughs of the determinant curve. The method to determine the 'dominant' mode was also explained (determined by the largest displacement of the sum of longitudinal and vertical displacements).

On the (001) plane of single aluminium crystal, SAWs have 4-fold symmetry, hence Figure 4.10a shows the calculated SAW 'dominant' mode versus angles between 0° and 90° with respect to the reference direction [100]; in other words, 0° is the direction of vector [100]; 45° represents the direction [110] which is 45° counterclockwise from direction [100] on plane (001). The PSAW of plane (001) first

occurs at the angle which is approximately 35° rotation from the reference direction [100] (0°) and last observed at 56°. From 35°, SAWs gradually become bulk waves and the displacements of the longitudinal and vertical directions decrease significantly towards zero at 45°. Simultaneously, PSAWs arise as it has a SAW-like oscillation pattern even though its propagation direction is not parallel to the free-surface but tilts down by a small angle into the medium. At 45°, PSAWs have no displacement component in the transverse direction, and the ellipse is only in the sagittal plane. The 'dominant' mode aluminium on planes (011) (Figure 4.10b) and (111) (Figure 4.10c) appear as a continuous curve without mode hopping. All the velocity curves agree with Farnell (the bottom three figures in Figure 4.10) [4].

(a) (001).   (b) (011).   (c) (111).

(d) (001).   (e) (011).   (f) (111).
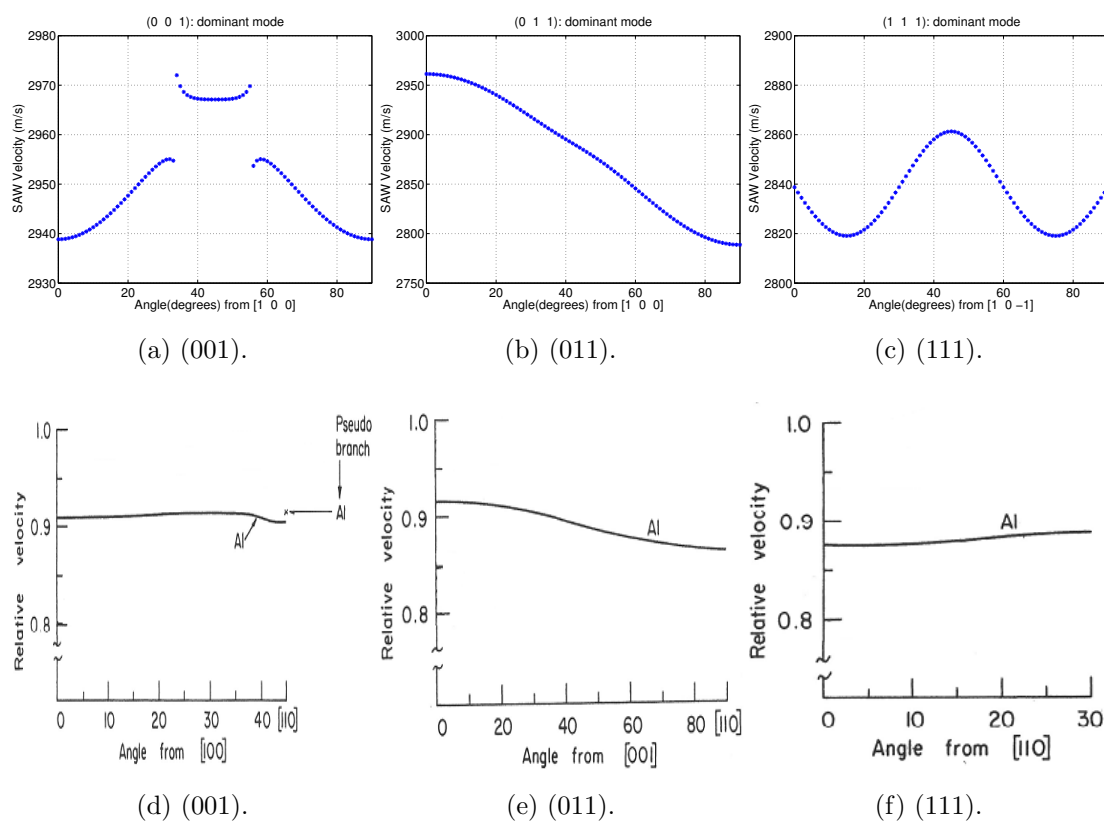
Figure 4.10: Top three figures are the calculated SAW on plane (001), (011) and (111) of aluminium. The bottom three figures are the calculated velocity curve by Farnell [4]. On top plane (111) 30° is the direction equivalents to the 0° of Farnell's result.

Modelling of Aluminium

In the 3D space, because the SAW velocity is influenced by the stress and strain indirectly, the SAW travels at different velocities on different planes along the same direction. Here in the SAW model, we used two dimensions to express the plane, one dimension for the direction on the plane, and one dimension to present the SAW velocities.

Figure 4.11 demonstrates the model for aluminium. The 'dominant' mode of SAW on each plane, whose normal is in the area between [001], [101] and [111], are shown as the ordinate varies from plane (101) to (001), with the abscissa being from plane (101) to (111); each plane has 11.25° with its adjacent one. The calculation procedure for the SAW velocity model is as follows:

1. Defines the plane by its Miller index.

2. Calculates the 4th-order stiffness tensor corresponding to the defined plane.

3. Defines the SAW propagation direction in the defined plane.

4. Calculates the 'dominant mode ' according to the determinant curve corresponding to the defined plane and direction.

5. Repeats the previous step on all propagation directions of the defined plane.

6. The velocity surface is obtained for the defined plane.

7. Repeats from the first step for all planes.

Although only half of the total distinct planes are shown, the planes that make up the other half of the model have mirror symmetry, except for a 90° rotation as explained in previous section. It should be noted that the shape of SAW varies gradually between the adjacent planes. The velocity surface is demonstrated in magnitude, i.e. the radii are proportional to velocity—which is also represented by segment colour, with red (longer) segments for faster phase velocity and blue

segments representing slower (shorter) ones. It can be seen that velocity surfaces of aluminium look almost like a circle as the velocities are not normalised although the velocity variation can be more easily recognised by the colour change with angle. The PSAW appear as continuous clusters with faster velocity than pure SAW, and can be observed on some planes such as (0.25 0.25 1).

The wave modes at each angle are determined by the troughs of the determinant curve which is calculated by the approximate velocity. There is the chance that if the interval of velocities are not small enough, the trough, which locates the mode, is missed. This can causes the absence of velocity at certain angles of some planes, for instance on plane (0.75 0.25 1) and (0.75 0.5 1).
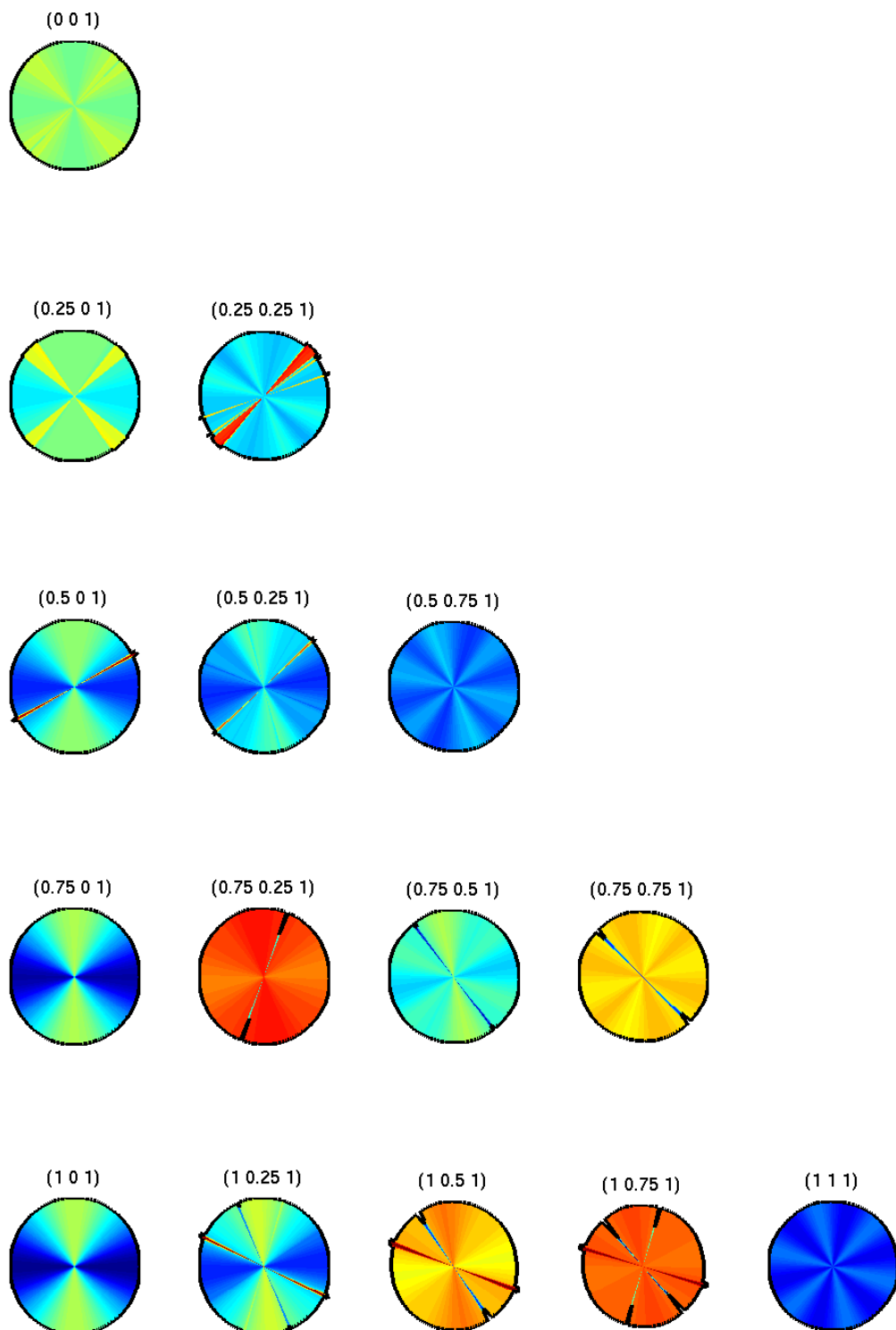
Figure 4.11: SAW velocity surface on planes whose normal is in the area between [001], [101] and [111] of aluminium.

4.2.3 Nickel

Nickel is a face-centred cubic crystal. Because of its good plasticity and corrosion resistance, nickel and its alloys are widely used in chemical engineering, electronic engineering and aeronautical manufacture. Nickel-based alloys are classified in certain applications as either superalloys, corrosion-resisting alloys or shape memory alloys.

Knowledge of the precise orientation of single nickel or nickel-based alloy crystals is essential for engineering control. For example, a nickel-based-superalloy which is used in applications such as high pressure turbine blades, requires high creep endurance in high temperature operating environments up to 1600°C [34]. Anisotropic control of the materials enhances their performance, with subsequent benefits such as more efficient fuel consumption. The model is calculated based on the elastic constants of single nickel crystal, $c_{11} = 247$GPa, $c_{12} = 153$GPa, $c_{44} = 122$GPa and $\rho = 8.912$gm/cm^3 [32].

SAW on typical planes : (001), (011) and (111)

As nickel is a cubic crystal and in the same category of having an anisotropic ratio $\eta > 1$, the velocity surface behaviour on all planes follows the same pattern as aluminium, hence the model is calculated at the same area as aluminium. SAW and PSAW (if it presents) of typical planes (001), (011) and (111) are plotted as a function of angle in Figure 4.12. The PSAW of plane (001) occurs at an angle which is at approximately 23° from the reference [100] direction (0°) is evident upto 67°. The 'dominant' mode of planes (011) (Figure 4.12b) and (111) (Figure 4.12c) appear as a continuous curve without mode hopping. The behaviour found here— including SAW and PSAW behaviour, roots pattern, manner of weighting factors and displacements—of typical planes (001), (101) and (111) are in agreement with Farnell in the bottom three figures in Figure 4.12 [4].

(a) (001).   (b) (011).   (c) (111).

(d) (001).   (e) (011).   (f) (111).
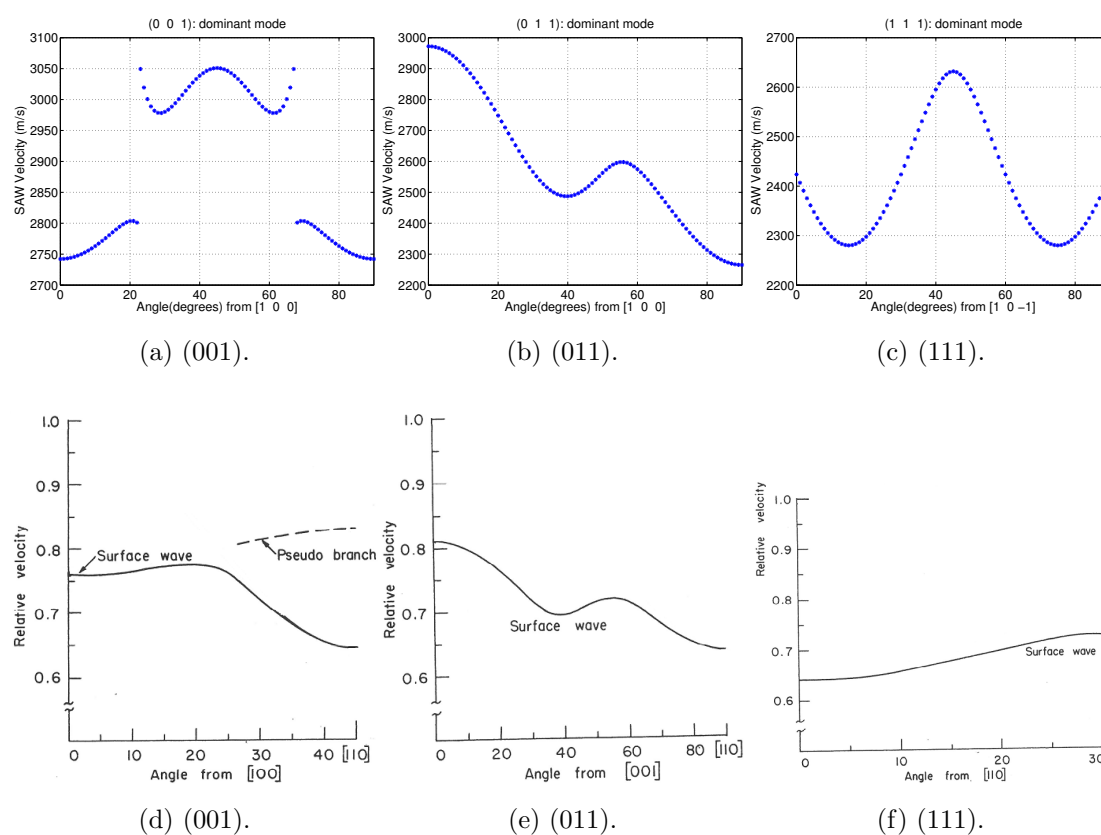
Figure 4.12: Top three figures are the calculated SAW on plane (001), (011) and (111) of nickel. The bottom three figures are the calculated velocity curve by Farnell [4]. On top plane (111) 30° is the direction equivalents to the 0° of Farnell's result.

Modelling of Nickel

Comparing the velocity surface of nickel with aluminium on typical planes, the results show a similar trend with regard to waves behaviour. The difference between these two materials is the anisotropic ratio—the variation of SAW phase velocity of all the planes of aluminium is approximately 2900m/s to 3200m/s, and in nickel it is approximately 2200m/s to 3400m/s.

Figure 4.13 illustrates the SAW velocity ('dominant' mode) of nickel. The velocity surface are not only demonstrated in magnitude (with magnitude represented by both length and colour), with red representing faster phase velocities and blue

representing slower one. The 'dominant' mode of SAWs on each plane whose normal is in the area between [001], [101] and [111] are shown as ordinate from plane (101) to (001), with abscissa is presenting from plane (101) to (111). Each plane has 11.25° with its adjacent one. It can be seen that the shape of SAWs varies gradually between the adjacent planes. The planes $(k\,h\,1)$ have mirror symmetry with the half planes $(h\,k\,1)$ (shown in the figure, except at 90° rotation as explained in previous section).

However, on nickel it is possible for more modes to exist than on aluminium, hence the behaviour of the waves is more complex. Because of this more mode jumping is observed on the velocity surface of nickel. The PSAW, which appear as a continuous clusters in a faster velocity than pure SAW, can be observed on some planes such as (001) and (0.25 0 1), and disappear as the planes gradually rotate from (001) towards (101) and (111). It is more obvious than those which were observed on aluminium as the plane rotates from (001) towards (101) and (111).
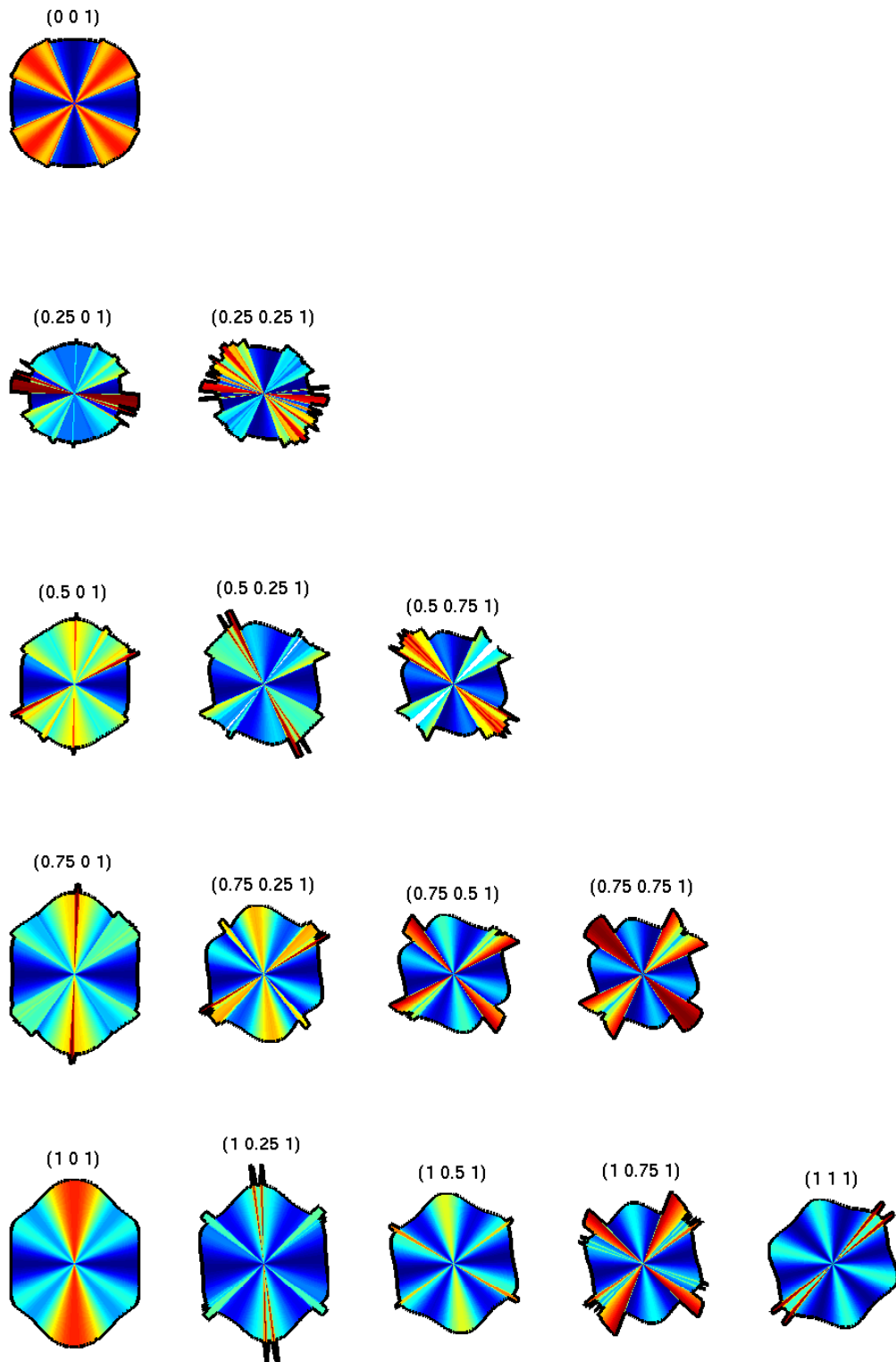
Figure 4.13: SAW velocity surface on planes whose normal is in the area between [001], [101] and [111] of nickel.

4.2.4   Titanium β

Titanium is named after the Greek god 'Titan' because of its high strength, ductility, heat resistance and corrosion resistance. Because of these properties titanium and its alloys are commonly utilised in space and aeronautics engineering. Due to its ubiquitous use in aircraft, naval hulls, spacecraft and missiles, the evaluation of its structure and characteristics is in high demand.

Titanium experiences phase transition during the annealing procedure, at 882°C it changes from α (hexagonal) to β (cubic) structure [35]. The parameters of titanium β used in the model are $c_{11} = 97.7$GPa, $c_{12} = 82.7$GPa, $c_{44} = 37.5$GPa and $\rho = 4.581$gm/cm^3 [36].

SAW on typical planes : (001), (011) and (111)

The anisotropy ratio η of titanium β is 5 resulting in the SAW phase velocity varying across a bigger range than aluminium on all planes. The wave modes are more complicated than aluminium and nickel. Figure 4.14 shows the SAW velocity of planes (001), and (011) as a function of propagation angle.

(a) (001).   (b) (011).
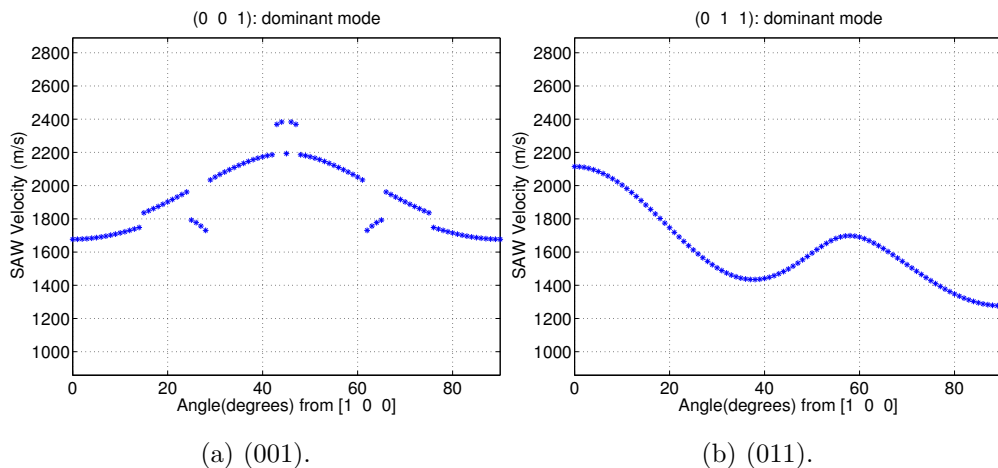
Figure 4.14: SAW on plane (001) and (011) of titanium β.

In Figure 4.14a, there are two modes 'dominant' in alternation between 0°

and 28° alternately, where only one continuous pure SAW appears during the same angles as with nickel and aluminium. The 'dominant' mode between 0° and 14°, and between 25° and 28° is a pure SAW. Between 15° and 24° is a mode which satisfies the boundary conditions with an increasing transverse component despite its propagating direction not being parallel to the surface. The PSAW arises between 29° to 61°. SAWs on the titanium (011) plane have a similar curve variation as aluminium and nickel. The 'dominant' mode in Figure 4.14b is a pure SAW and becomes Rayleigh wave at 0° and 90°.
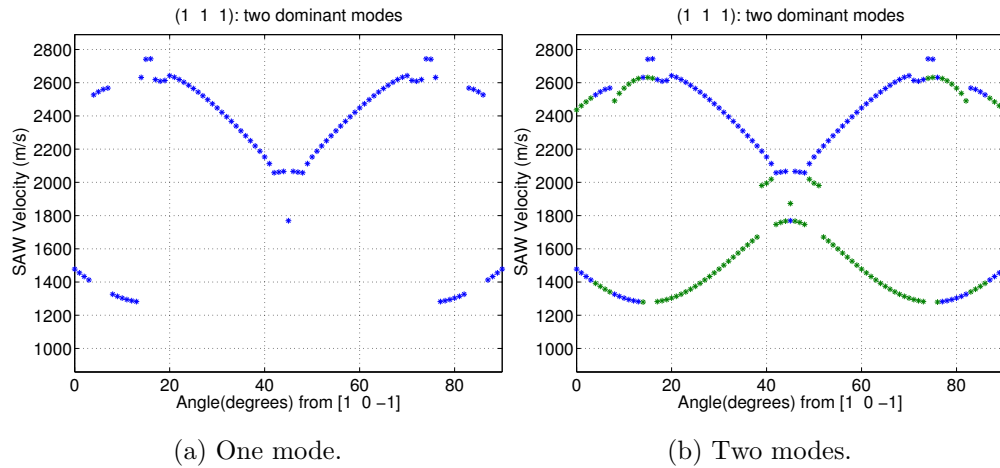
(a) One mode.   (b) Two modes.

Figure 4.15: SAW on plane (111) of titanium β.

Figure 4.15 illustrates the SAW on plane (111) of titanium β. The left figure shows the 'dominant' mode with largest displacement, which might be two discontinuous modes, as a function of angle. The two 'dominant' modes are shown in Figure 4.15b. The slower curve is a SAW and the faster one represents a PSAW. The colour indicates the order of the magnitude of displacements; blue and green are first 'dominant' and second 'dominant' modes respectively. Because SAW and PSAW appear alternately, it is very likely that the displacements are very close numerically in the sagittal plane; and that these two waves would be observed simultaneously in a medium with a large η [4]. The PSAW branch has mode jumping to the adjacent mode at angles (near15° and 40°), however it still follows

the particle motion pattern of PSAW. At 45°, the PSAW degenerates into a bulk wave and the SAW becomes 'dominant' (depicted in blue) and the isolated green point at this angle is the bulk wave.

Modelling of Titanium β

The Figure 4.16 illustrates the model of titanium is β phase. The 'dominant' mode of SAWs on each plane, whose normal are in the area between [001], [101] and [111], are shown as ordinates from plane (101) to (001), with abscissa presented from plane (101) to (111). Each plane differs by 11.25° from its adjacent planes. There are significant variations of wave modes on most of the planes. As the planes rotate from (001) towards plane (111), PSAW and SAW gradually become significant and can be observed simultaneously on the some planes, for instance (111). This figure only shows the 'dominant' wave mode on each plane, the criterion for observation of SAW and PSAW evidently requires further investigation.
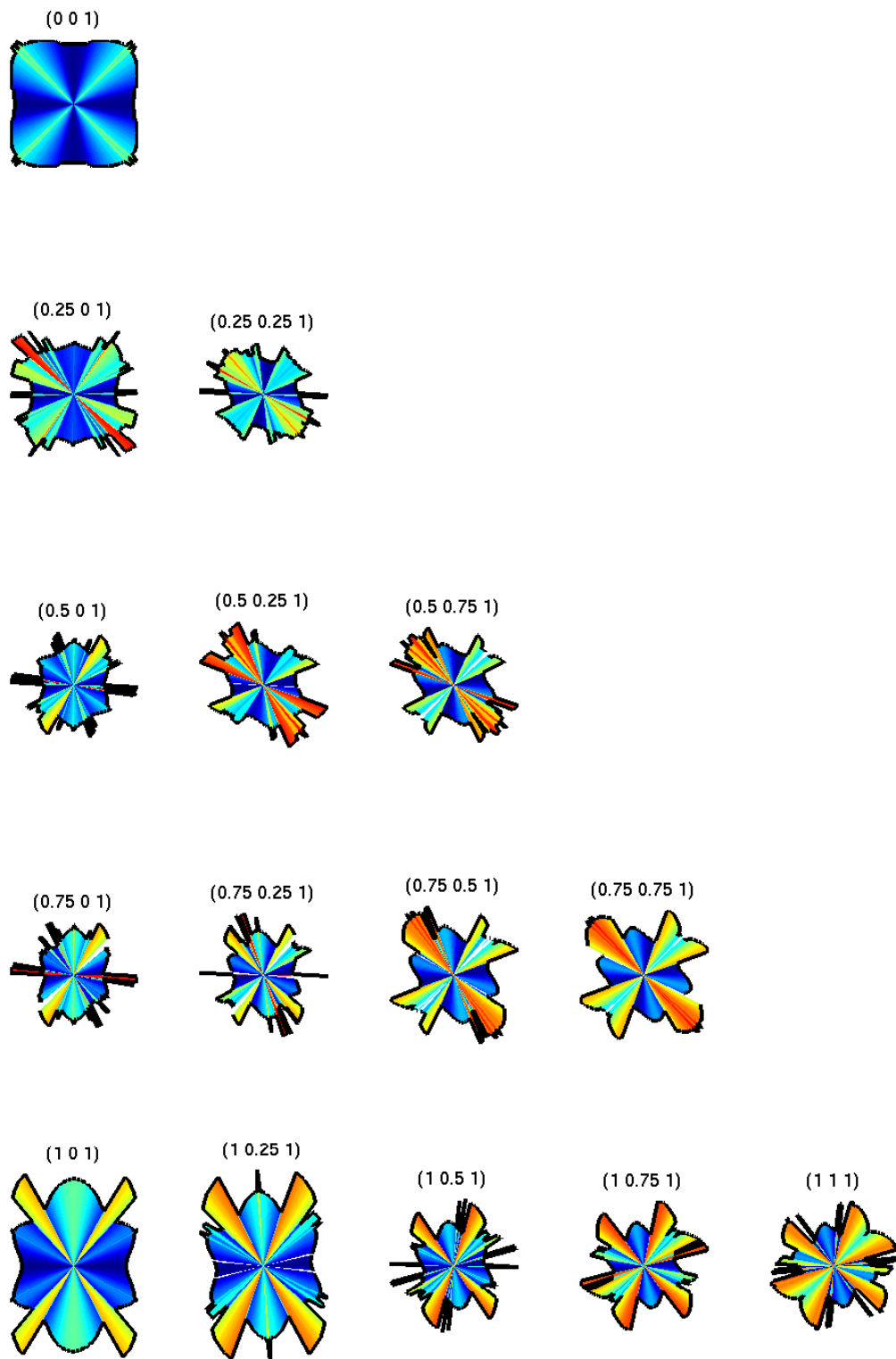
Figure 4.16: SAW velocity surface on planes whose normal is in the area between [001], [101] and [111] of titanium β.

4.2.5 Hexagonal Structure

Several different notations of the coordination system are in use for hexagonal crystals in different circumstances. Figure 4.17a illustrates the coordination system which is used in the model described herein; six directions, [100], [010], [-110], [-100], [0-10] and [1-10], rotated counterclockwise on basal plane (001) are demonstrated. Because of the symmetry of the hexagonal crystal structure, only 1/24 of planes of a sphere are needed, all others being repetitious information. The modelled planes, whose normals are in the area between [001], [010] and [100], are as shown in Figure 4.17b. The angle between adjacent planes is 2.5° and the velocities on each plane are calculated at one degree intervals.

(a) Coordinate system.   (b) Calculated area.
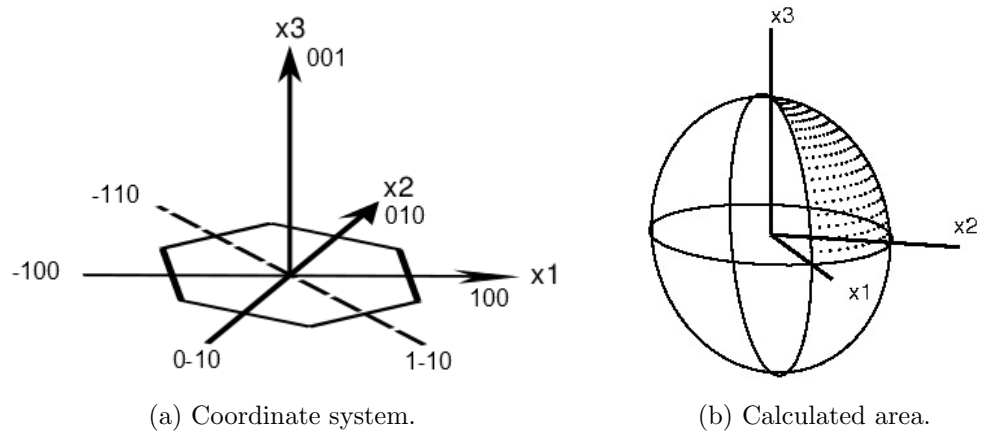
Figure 4.17: Definition of coordinate system of hexagonal crystals is shown in the left figure with six directions on basal plane (001). The right hand side of the figure shows the area where the normal of the calculated planes are.

4.2.6 Titanium α

The structure of titanium exists in two phases, the cubic titanium β, and the hexagonal alpha phase. The alpha phase is more stable at ambient conditions and the beta phase is formed by annealing alpha titanium above 882°C [35]. α titanium has a hexagonal structure, and the model is calculated based on the elastic constants $c_{11} = 163.6$GPa, $c_{12} = 92.3$GPa, $c_{13} = 67.92$GPa, $c_{33} = 185.2$GPa,

$c_{44} = 47.05\text{GPa}$ and mass density $\rho = 4.429\text{gm/cm}^3$ [37].

SAW on typical planes : (001) and (100)

(a) (001).   (b) (100).
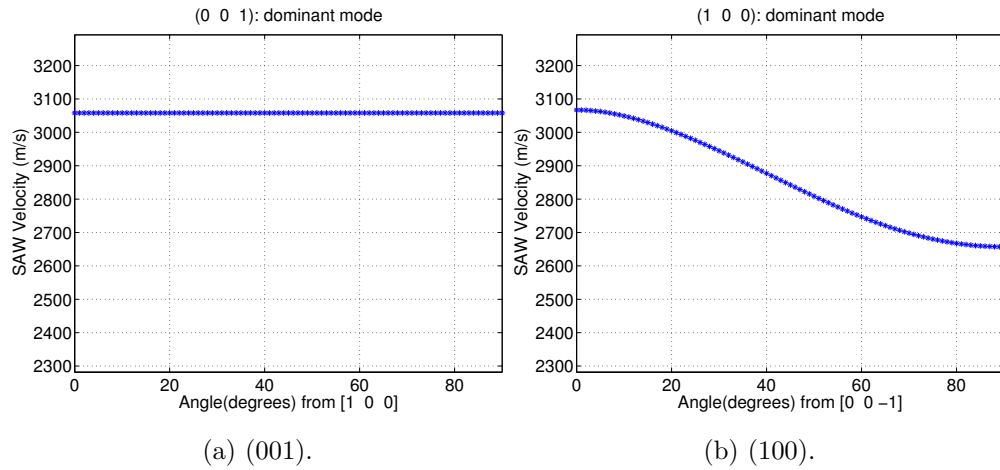
Figure 4.18: SAW on plane (001) and (100) of titanium α.

SAWs on the basal plane (001) of hexagonal crystals is isotropic and can be seen in Figure 4.18a, that the SAW phase velocity is a constant (3058m/s at all angles). Due to the unique SAW velocity behaviour on this plane the SAW can not be used to determine the information about the angle on this plane. The (100) plane of titanium α has 2-fold symmetry; the 'dominant' mode in Figure 4.18b is continuous pure SAW and rotates from reference direction [00-1] towards [010] (90°) with a corresponding velocity decrease.

Model of Titanium α

The calculated model of titanium α is displayed in Figure 4.19. The 'dominant' mode of the SAW on each plane, whose normal is located in the area between [001], [110] and [100], are shown with the abscissa from plane (100) to (110), and with ordinate from plane (100) to (001). Each plane has 7.5° with its adjacent plane from plane (100) to (110) and 20° from plane (100) to (001). The planes of the other half of model have mirror symmetry excepts 90° rotation as explained in the

previous section. In summary, SAWs on the basal plane are isotropic and all the other planes have 2-fold symmetry.

4.2.7   Summary

The SAW velocity models of four materials—aluminium, nickel, Ti-β and Ti-α— are presented in this section. The velocity surface on several planes of each material are shown. Because of the symmetry of each crystal family, those planes which have redundant (i.e., identical) information are excluded in the model. The 'dominant' mode on each plane is determined by considering the wave modes which are generated most efficiently i.e., with the largest overall displacement, which is the sum of displacements on the longitudinal and vertical directions. The velocity surface of the dominant modes are presented in the model. It is notable that certain combinations of orientation and direction on certain materials result in more than one observable mode.
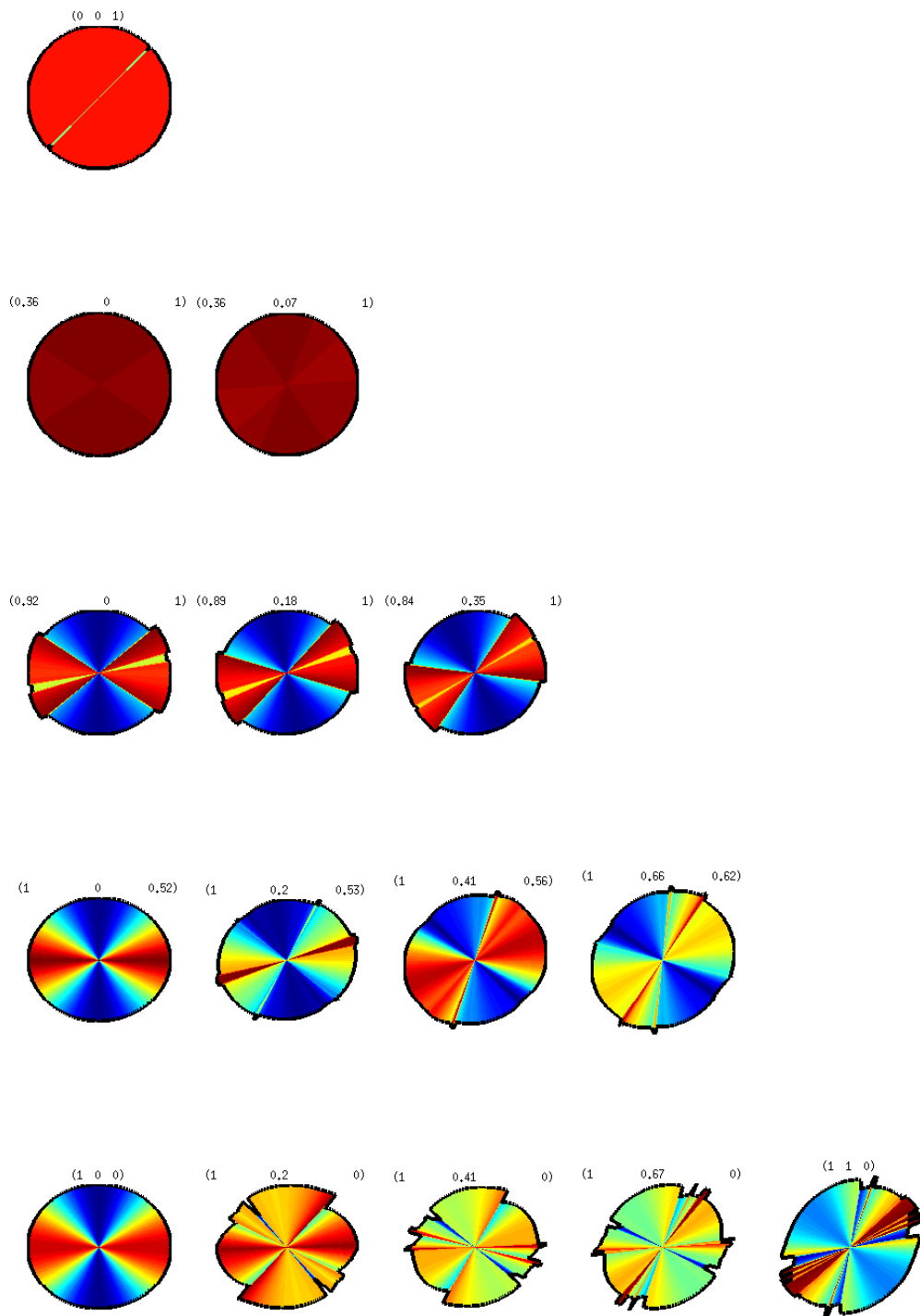
Figure 4.19: SAW velocity surface on planes whose normal is in the area between [001], [110] and [100] of titanium α.

4.3 Inversion: Overlap Function

Chapter 3.5 shows how SRAS works experimentally either measuring A_k or A_f, in both cases this can be converted to $A(v)$, which is the spectrum at a particular direction on a velocity surface spectrum. It is assumed the plane orientation noted as (hkl) and the direction on the plane is θ, with (hkl) and θ are known. If a mode exists with a velocity $v(h, k, l, \theta)$ then $A(v)$ should have a maximum present at $v(h, k, l, \theta)$.

In a real experiment $A(v)$ is measured at each point on the sample but orientation and direction are unknown. The challenge then is to determine orientation and direction from $A(v)$. A brief examination of the 'forward' problem (determining v_{model} from known orientation and direction) will demonstrate that inverting this would be extremely challenging and most likely ill-conditioned (due to the redundancy resulting from the symmetry). In addition to the analytical challenge of inversion and ill-conditioning there is a practical problem,

$$((hkl),\, \theta) \rightarrow \text{velocity}$$

but there is no unique mapping velocity $\rightarrow$ $((hkl),\, \theta)$. However, for a set of $v'(h, k, l, \theta)$ (a velocity surface with unknown orientation and direction) there might be a mapping $v(\theta) \rightarrow (hkl)$ finding an analytical technique to map $v(\theta)$—combining a multitude of velocity measurements—poses additional complexity.

As a consequence of this complexity (and potential non-invertibility) I have developed a semi analytical inversion technique that can robustly find orientation and direction as a function of $v'(h, k, l, \theta)$ where $v(\theta)$ is sufficiently anisotropic. It can also identify when $v(\theta)$ is insufficiently anisotropic or isotropic.

The different approaches investigated to determine this merit function are discussed below. The two methods discussed are both overlap functions, but different calculations of the merit function utilised. In order to distinguish these methods they are named method I and method II.

4.3.1 Method I: Use Experimental Data in Velocity Surface Spectrum and Model Velocities with Displacements

Figure 4.20 is the experimental data $A(\phi, v)$ represents the signal strength with regard to propagation directions ϕ and possible velocity v over a certain range with the displayed signal strength proportional to a colour spectrum i.e., a colour map (where red is the highest and blue for the lowest signal level recorded). This merit function is customised for the SRAS scanning results.

The experiment begins at an arbitrary direction on the sample surface and moves through the angles of direction stepwise. In the data presented here the step size is $5°$. The overlap function is calculated by comparing the measured velocity versus values from the precalculated model. The final orientation is determined as the plane and direction where the maximum of the figure of merit of the overlap function is located.

In order to determine the orientation, the following procedure was implemented: the model velocity and displacements are defined as $v(h, k, l, \theta)$ (black dots in Figure 4.20), where the plane is defined by its (hkl) parameters, and θ is the angle on the plane. The experimental data $A(\phi, v)$ is shown as a velocity surface spectrum in Figure 4.20. The calculated velocity $v(h, k, l, \theta)$ is used as an index, hence, the value where it is overlapped by $v(h, k, l, \theta)$ on the velocity surface spectrum is $A(\phi, v_{(h,k,l,\theta)})$. The figure of merit is the sum of $A(\phi, v_{(h,k,l,\theta)})$ at each (hkl) and θ calculated. Therefore, by repeating the calculation on all planes and all directions, the largest value for the figure of merit after normalisation indicates the best match

$$F(h, k, l, \theta) = \sum_{\phi=0}^{\phi=\frac{n-1}{n}\pi} A(\phi, v_{(h,k,l,(\phi-\theta))}), \ (n = 1,\ 2,\ 3,\ ...) \qquad (4.25)$$

where n represents the number of evenly spaced velocity measurements used to determine the velocity.
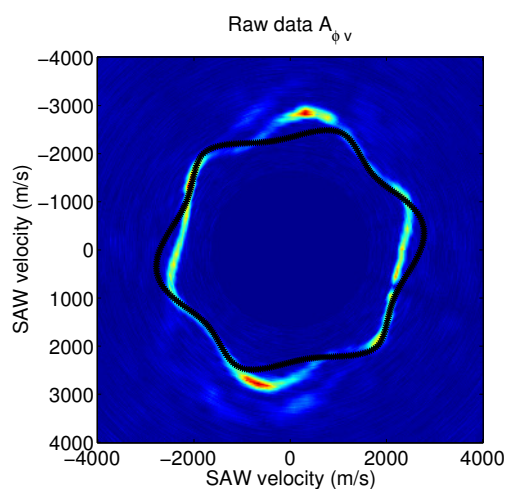
Figure 4.20: Experimental data $A(\phi, v)$ is shown on the left, and the calculated velocity model $v(h, k, l, \theta)$ is plotted as black dots. The calculated velocity is used as index, and the value underneath it is $A(\phi, v_{(h,k,l,\theta)})$.

Each figure in Figure 4.21 demonstrates the calculation performed at one angle on one plane; the left three figures show incorrect combinations of angle and plane (i.e., those not being maximum figures of merit); the right hand figure shows the combination of angle and plane with the highest figure of merit and therefore represents the result of the overlap function. The merit function is simply the sum of the amplitude under the black asterisks on those graphs and is given under each graph. It can be seen in this figure, $F(h, k, l, \theta)$ is larger when the model better fits the velocity surface spectrum.
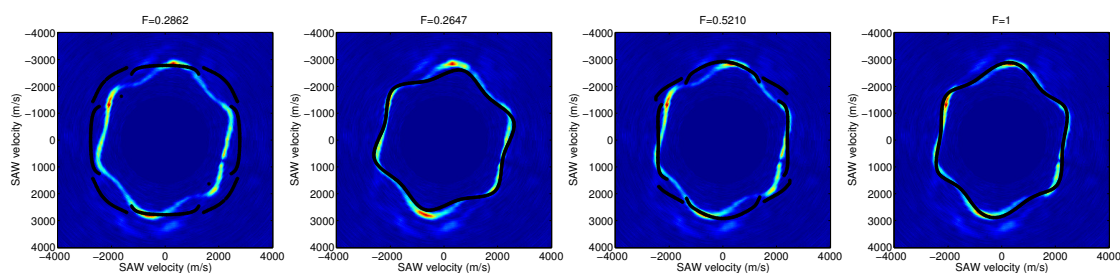
(a) $F(0\,0\,1\,0)$=0.2862 (b) $F(1\,1\,1\,0)$=0.2647 (c) $F(0.45\,0\,1\,0)$=0.5210 (d) $F(0.85\,0.3\,1\,15)$=1

Figure 4.21: Curve fitting procedure. From left to right are the normalised figure of merits of three different angles on different planes. The normalised value of F indicates how well the model fits to the experimental velocity surface spectrum. Left three are not the matched results but the right one is.

The inversion technique presented here is a facile method to search through orientation and direction to maximise the merit function. This is illustrated in Figure 4.22, where the correct output model plane (asterisks) by the overlap function is shown against the experimental data. Calculations of the figure of merits show the unknown nickel sample is plane (0.85 0.3 1) with a 15° rotation from reference direction [1 -0.1 -0.82]. For convenience fractions are used rather than integers to present Miller indices here.
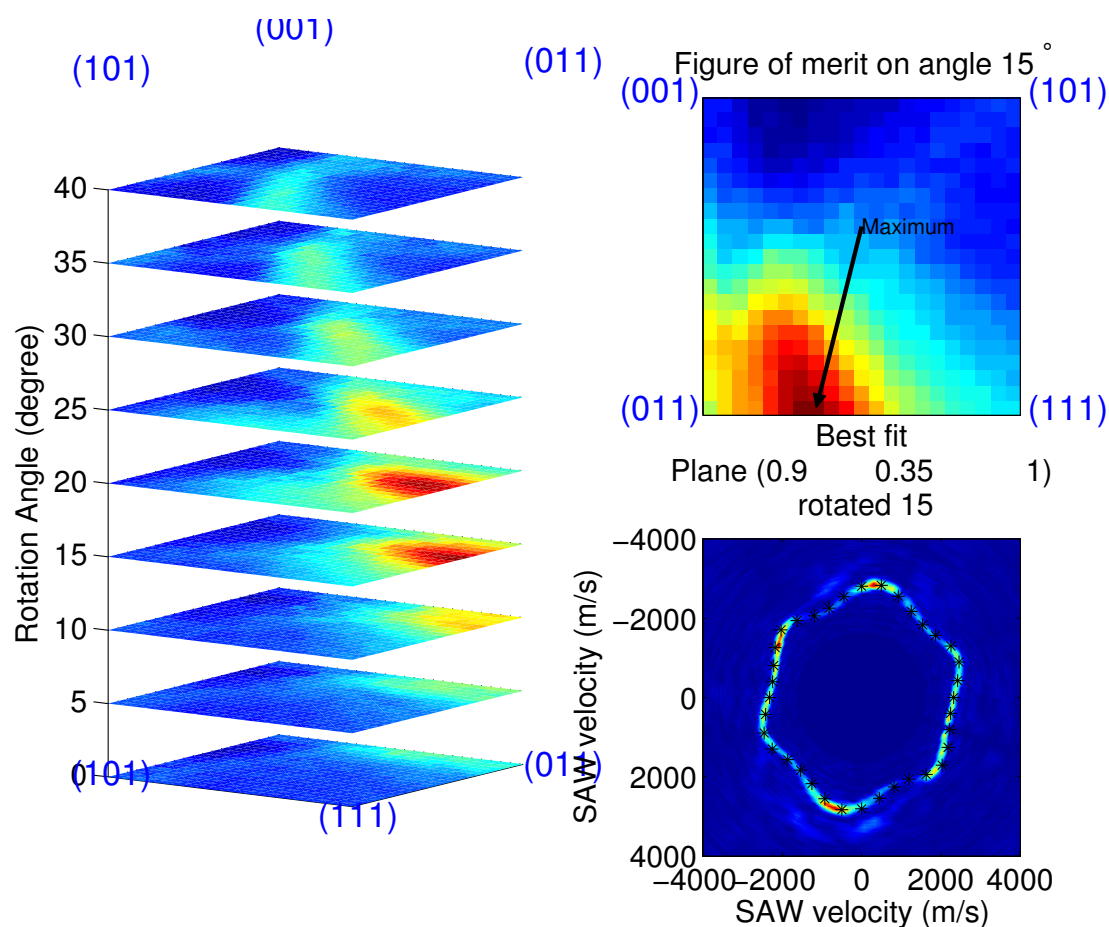
Figure 4.22: Curve fitting procedure. On the left is the figure of merit over all planes and rotation angles; the right top points out the maximum of the figure of merit is on the rotation of 15°; the right bottom shows the experimental data with the determined result (asterisks).

4.3.2   Method II: Use Experimental Data Fitted and Model on Gaussian Filter

The method II is still an overlap function but accomplished using the simulated data $A(h, k, l, \theta, v)$ based on the model, and swapping the position of experimental data and model in method I. A comparison of method I and method II is shown in Table 4.1.

Data Source	Method I	Method II
Experimental Data	Velocity Surface Spectrum $A(\phi, v_{(h,k,l,\phi)})$	Velocity Surface $v(\phi)$
Calculated Model	Velocity Surface $v(\theta)$	Velocity Surface Spectrum $A(h,k,l,\theta,v^e_{(\phi)})$ $A(h,k,l,\theta,v) = \begin{cases} D(h,k,l,\theta), \ v = v(h,k,l,\theta) \\ 0, \ v \neq v(h,k,l,\theta) \end{cases}$
Figure of Merit	$F(h,k,l,\theta) = \sum_{\phi=0}^{\phi=\frac{n-1}{n}\pi} A(\phi, v_{(h,k,l,(\phi-\theta))})$	$F(h,k,l,\theta) = \sum_{\phi=0}^{\phi=\frac{n-1}{n}\pi} A(h,k,l,(\phi-\theta),v^e_{(\phi)}) \times G(v),$ where $G(v) = \frac{1}{\sigma\sqrt{2\pi}}\exp\frac{(v-\mu)^2}{-2\sigma^2}$
	The Maximum of $F(h,k,l,\theta)$ Points to the Correct Orientation and Direction.	
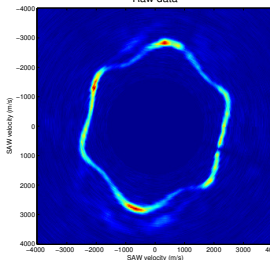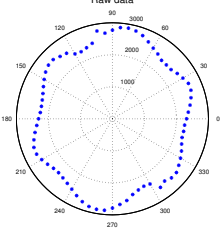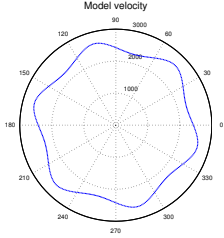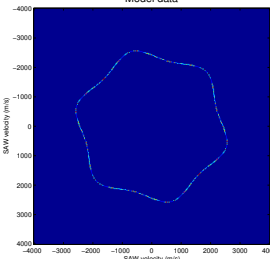
Table 4.1: Two different approaches of the overlap function.

As described in Chapter 2, SRAS results can be presented as a velocity surface $v^e(\phi)$. This is accomplished by selecting the model velocity $v(h, k, l, \theta)$ of an arbitrary plane (hkl) and converting this velocity curve into a velocity surface spectrum, with the peak of the spectrum at each direction θ equal to the displacement $D(h, k, l, \theta)$ which corresponds to $v(h, k, l, \theta)$. A Gaussian filter, which is defined as

$$G(x) = \frac{1}{\sigma\sqrt{2\pi}} \exp{-\frac{(x - \mu)^2}{2\sigma^2}} \tag{4.26}$$

where μ is the expected value and σ is the standard deviation of the Gaussian distribution, has been applied on the vertical direction of $A(h, k, l, \theta, v)$. And the figure of merit is

$$F(h, k, l, \theta) = \sum_{\phi=0}^{\phi=\frac{n-1}{n}\pi} A(h, k, l, (\phi - \theta), v^e_{(\phi)}) \times G(x) \tag{4.27}$$

As with method I, the maximum of $F(h, k, l, \theta)$ points to the correct orientation and direction.

The full width at half maximum (FWHM) of the Gaussian filter is given by

$$FWHM = 2\sqrt{2ln2}\sigma \tag{4.28}$$

and equals 240m/s in this figure. The FWHM is increased by increasing σ.

The method I is customised for SRAS results, which presents experimental data as velocity surface spectrum. However, for other techniques which obtain SAW velocity surface as raw data, the method II is appropriate. The least-squares method is not used here because it is not appropriate if the velocity curve is discontinuous either in measured data or predicted model. The random points would contribute a large error to the sum of the squares. In addition, at the certain angles of some planes, two modes can be observed simultaneously, and since the Gaussian curve fit on the velocity spectrum can only return one velocity

(an intermediate value of the peaks) at that angle, the least-squares method is not suitable in these cases.

4.3.3 R-value Assessment

The difference in orientation between the plane selected for the simulation and the output using the overlap function is assessed by a figure known as the 'R-value' [34]. It is an industry standard which has been used over the past 30 years to evaluate the disorientation between two adjacent grains. There are five common ways to calculate the R-value: single-angle cos, two-angle cos, two-angle root mean square (RMS), three-angle cos and three-angle RMS (see Appendix E). Here we have used the two-angle cos method (also known as REL or R-2cos), whereby the R-value is calculated using two angles

$$R = \arccos(\cos\phi\cos\tau) \tag{4.29}$$

where ϕ is the smallest angle to rotate grain A to the orientation of grain B, τ is the rotation angle needed to superpose grain A and B after the first step (see Appendix E). The R-value is presented in degrees with range from 0° to 62.8°.

Here the R-value is used as an indication of the error of the overlap function rather than the disorientation at the boundary of two adjacent grains. If only the plane (hkl) is required and the rotation angle of the plane is unimportant, ϕ alone is sufficient. Note that in the case of the basal (001) plane of hexagonal crystal structures where the SAW velocity is isotropic, it is not possible to determine τ by SRAS.

4.3.4 Interpolation of the Figure of Merit

When performing the overlap function on SRAS results, the rotation angle and plane were determined by the location of the maximum of the figure of merit

in Figure 4.22. The maximum of $F(h, k, l, \theta)$ matched plane (0.85 0.3 1) with the propagation direction of 15°. The top row in Figure 4.23 shows $F(0.85 \, k 1 \theta)$, $F(h \, 0.3 \, 1\theta)$ and $F(hk1 \, 15)$ respectively, which are the figures of merit near the maximum. None of them are smooth surfaces in the strictest sense of the word, although near the maxima the variation (spatial frequencies) are relatively low. Hence, interpolation is introduced to improve the accuracy of the search results.

The cubic spline interpolation is a common curve fitting method in engineering which uses piecewise polynomial function. It refers to the polynomial function but avoids the Runge's phenomenon which is the error caused by the high degree polynomial function. The cubic spline interpolation function is defined as follow:

$$S(x) = \begin{cases} s_1(x), \text{ if } x_1 \leq x < x_2 \\ s_2(x), \text{ if } x_2 \leq x < x_3 \\ \vdots \\ s_{n-1}(x), \text{ if } x_{n-1} \leq x < x_n \end{cases} \tag{4.30}$$

where $s_i(x)$ is a third degree polynomial defined as

$$s_i(x) = a_i(x - x_i)^3 + b_i(x - x_i)^2 + c_i(x - x_i) + d_i \tag{4.31}$$

for $i = 1, 2, ..., n - 1$.

All three figures are shown in the bottom row in Figure 4.23 plotted at smaller intervals using the interpolated results to produce smoothed curves. The interpolation is only applied to the area around the maximum value of the figure of merit in search algorithm because the interpolation does not change the location of the maximum value (which gives the orientation of the crystal), but does identify it more precisely. After interpolation, the example in Figure 4.23 gives an orientation of plane (0.91 0.35 1) and propagation direction of 16.75°; these differ from the uniterpolated results which gave the plane as (0.85 0.3 1) and the propagation direction as 15°.

(a) h=0.85.   (b) k=0.3.   (c) θ=15°.
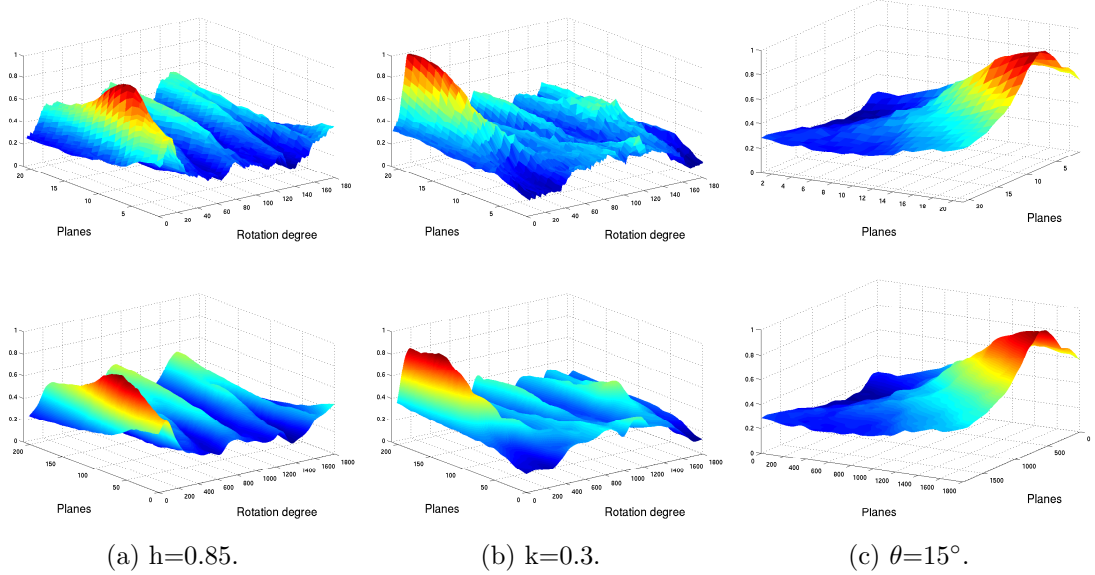
Figure 4.23: The maximum of $F(h, k, l, \theta)$ gave the matched plane (0.85 0.3 1) with rotation angle 15°. The top three figures illustrate $F(0.85\,k\,1\,\theta)$, $F(h\,0.3\,1\,\theta)$ and $F(h\,k\,1\,15)$ respectively; the bottom three figures are the same results after using cubic spline interpolation.

4.4   Search Algorithm Performance Evaluation

For evaluating the performance of the overlap function, a Gaussian filter and Gaussian white noise (GWN) are applied to a model velocity i.e., a model calculated for a given plane and direction, to simulate experimental data. The output of the overlap function is compared with the known plane and direction of the simulated data to evaluate its performance. This evaluation is demonstrated on both nickel and aluminium models in the following section.

These evaluation results can be applied to both overlap function methods. Since the major difference between the two methods is the FWHM of the velocity surface spectrum, this is one of the variables used in the evaluation.

4.4.1   Experimental Data Simulation

Table 4.2 describes the simulation procedure of an experimental velocity spectrum for evaluating the overlap function. Firstly, a velocity surface with a corresponding calculated displacement from an arbitrary orientation and direction is chosen. A scaling factor is multiplied by the velocity to simulate the velocity shift which is caused by the apparatus. Secondly, the velocity surface is then weighted according to its displacement and converted to a velocity surface spectrum. As described in the previous section, a Gaussian filter is used to customise the FWHM of the velocity spectrum. GWN has been chosen to be applied in the simulation data as it is a common type of signal noise within electronic systems. The GWN parameter of μ (mean) is set to 0 in this simulation procedure since it will otherwise raise the amplitudes of the signal levels therefore causing $F(h, k, l, \theta)$ to increase by values proportional to μ. μ has no effect on the maximum of $F(h, k, l, \theta)$. σ is the parameter which relates to the width of Gaussian distribution and has relationship with the SNR

$$SNR_{dB} = 10 log_{10} \frac{\mu}{\sigma} \qquad (4.32)$$

Steps	Description	Expression
1	Chooses an arbitrary velocity surface and its corresponding displacement from the model	$v(\phi)$ and $D(\phi)$
2	Applies a scaling factor on the velocity surface	$v'(\phi) = v(\phi) \times (1 + p)$, where p is the scaling factor
3	Converts the velocity surface to velocity surface spectrum	$A(\phi, v) = \begin{cases} D(\phi), \ v = v'(\phi) \\ 0, \ v \neq v'(\phi) \end{cases}$
4	Applies Gaussian filter	$A'(\phi, v) = A(\phi, v) \times G(v)$
5	Applies Gaussian noise	$A''(\phi, v) = A'(\phi, v) + GWN(\mu, \sigma)$

Table 4.2: Simulation of the Experimental Data.

Figure 4.24 shows a simulated example $A''(\phi, v)$ and a $A''(v)$ at a particular angle. The FWHM of the spectrum equals 240m/s and SNR is 17dB. After preparation of simulated experimental data, the overlap function is performed on this simulated data $A''(\phi, v)$.

Plane (0.45 0.75 1)
after added noise
SNR: 17 dB
std = 0.03%

(a) $A''(\phi, v)$.

(b) $A''(v)$.
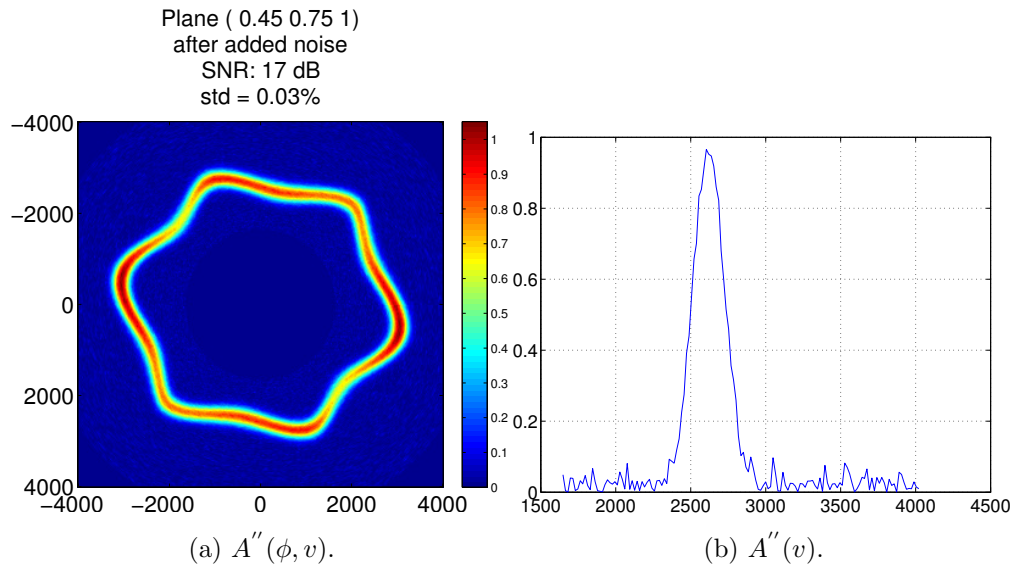
Figure 4.24: $A''(\phi, v)$ (left) and a $A''(v)$ at a particular angle (right) with noise have been added. In these two figures, the FWHM of the spectrum equals 240m/s and SNR is 17dB.

The evaluation is performed by varying the spectrum width, SNR and the velocity shift of the simulated velocity surface spectrum. The experimental data from k-SRAS and f-SRAS results in Table 4.3 show the average SNR and average spectrum width of both systems. These data give us approximate ranges of SNR and spectrum width, which are then used as the initial variables in the simulation. Hence, the evaluation results allow confirmation of how reliable the overlap function is under the parameters of the experimental conditions. The evaluation results also allow us to identify experimental parameters (FWHM of the spectrum and SNR) which minimise the R-value (which is described in the following section) for the overlap function.

Operation System	Average SNR(dB)	Average FWHM of the Experimental Spectrum
k-SRAS	16.90	243 m/s
f-SRAS	23.98	219 m/s

Table 4.3: Experimental parameters of two SRAS systems.

4.4.2   Nickel

A velocity surface of an arbitrary orientation and direction is chosen from the calculated model; the parameters: the spectrum width, SNR and the velocity scaling factor, are varied within a certain range and simulate the experimental velocity surface spectrum for performing the search algorithm. Figure 4.25 shows the evaluation results of nickel. The figure shows the R-value in slice image where x axis is the SNR from 5dB to 50dB, and y axis is the FWHM of the experimental spectrum from the simulated experimental data recorded from 50m/s to 700m/s, and z axis indicates the velocity shift from 0% towards 3% (assuming the average SAW velocity of nickel is 3000m/s, hence, the maximum velocity shift in this figure is ±90m/s). The industrial standard of 8° is typically set as a limit for the R-value [34]; any value larger than 8° is displayed here in dark red and the areas of yellow, green and blue colour indicate the acceptable ranges of SNR and width of spectrum in the experimental data.

It can be seen in the figure that if the experimental data has an identical velocity to the model for nickel and where the FWHM of experimental raw data spectrum is less than 250m/s with an SNR from 5dB to 50dB, then the correct plane can be determined by the overlap function without error (indicated in dark blue). Where the experimental data has a FWHM smaller than ca. 650m/s and with a SNR larger than 5dB, despite the velocity having a 2.4% shift, the correct plane can still be determined by the overlap function within the accepted maximum R-value.

Figure 4.25: The R-value evaluation of searching algorithm. Value range of system SNR and width of experimental spectrum are tested.

4.4.3 Aluminium

The evaluation of the overlap function on aluminium is illustrated in Figure 4.26. The figure shows the R-value in a slice image where x axis is the SNR from 5dB to 50dB, and the y axis is the FWHM of the spectrum from the simulated experimental data from 50m/s to 400m/s. The feasible range of velocity shift on

the z axis is smaller than that with the nickel model since aluminium is a weakly anisotropic material (its velocity variation is approximately ± 16m/s to ± 126m/s on each plane, rather than ± 176m/s to ± 353m/s of nickel), therefore a velocity shift of only 0.3% is permissible in the experimental data if the FWHM of the experimental spectrum is smaller than 150m/s. In the case of there being no velocity shift of the 'measured' results, the maximum FWHM of its spectrum is 300m/s for the overlap function to work efficiently i.e., having an error of less than 8°.

4.5 Summary

This chapter has explained the procedure for modelling the phase velocity of SAWs. Models of four crystals have been shown. A merit function with different approaches (methods I and II) were introduced to adapt the format of the velocity data obtained from different techniques. This merit function was evaluated based on the models of nickel and aluminium. Simulation results have confirmed this function is successful when the experimental data spectrum, system SNR and velocity shift are within a certain range. For practical applications the SRAS systems satisfy these requirements and the overlap function based on the SRAS results is reliable for crystal orientation determination.
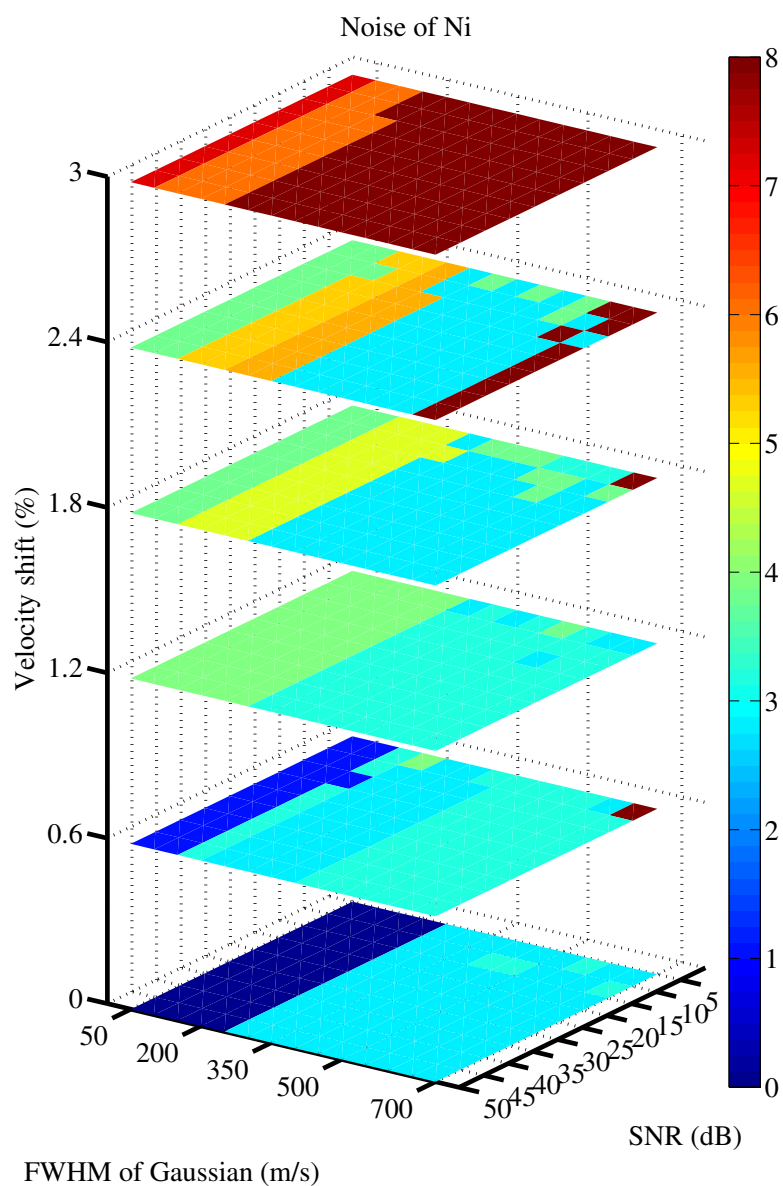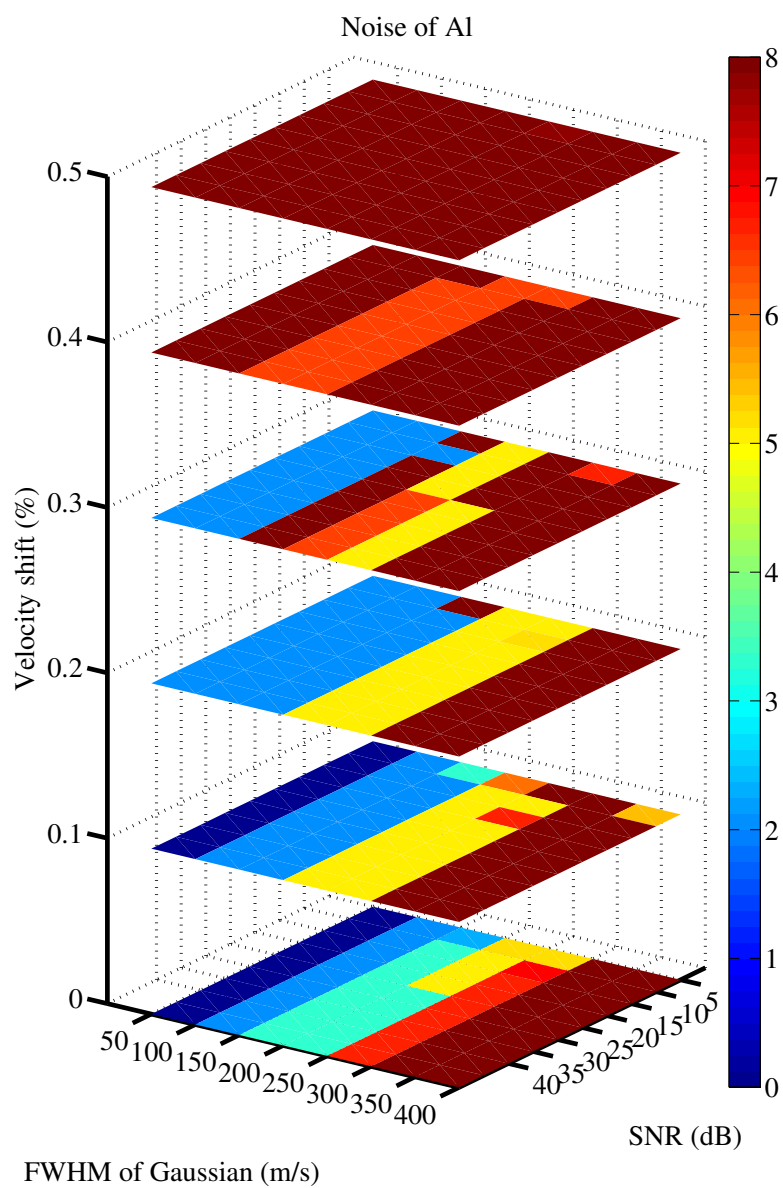
Figure 4.26: The R-value evaluation of searching algorithm. Value range of system SNR and width of experimental v curve are tested.

Chapter 5

Experimental Validation

This chapter describes the experimental measurement of grain orientation and compares these measurements with orientation measurements made using complimentary techniques such as LBR and EBSD.

The overlap function is performed on 3 aluminium and 12 nickel samples in two approaches; results are compared to LBR data. Since acquiring the data is relatively slow and the time required is proportional to the numbers of angles measured, experiments were compared to determine the minimum numbers of angles required. Results of three samples are illustrated when 36, 9 and 6 directions of experimental data are used. Error analysis of 12 single crystal nickel samples with known orientations are used to demonstrate and assess the inversion algorithm. Finally, the inspection procedure for samples with multiple grains is demonstrated, the results of SRAS scanning and orientation determination are shown.

As both k-SRAS and f-SRAS record the experimental data as velocity surface spectrum, samples may be measured using either system; both were used to collect data presented in this chapter.

5.1   System Accuracy

Comparing the SRAS results on single grain (which was obtained in Chapter 3), with the calculated model from Chapter 4, the orientation of the grain can be determined. The SAW velocity model is calculated based on the elastic constants and mass density of the material; any error in these parameters could cause significant error and prevent the inversion algorithm from working. Furthermore, the system efficiency and systematic error need to be considered practically. Finally, the system noise must be considered.

The following factors may influence the accuracy of the SAW inversion procedure:

- SRAS system generating/detecting efficiency

  In the cases where several wave modes are found in the model calculations, the modes which are most efficiently generated and detected with the experimental set-up should be selected. The experimental results of samples with known orientation are compared with the calculated wave modes to confirm the system efficiency.

- Feature tolerance of mask

  Chapter 2 gave details of how a mask is used to generate a grating pattern in the SRAS system. As the grating spacing is a significant parameter in data processing, the precision of the mask does effect the experimental results to a certain extent. According to the mask manufacturer's technical report, the feature tolerance of the super high resolution design of chrome on soda lime glass, which is the customisation mask in the f-SRAS system, is $\pm 0.8 \mu$m [38]. The mask, which has been used to obtain the single grain results in Chapter 3, has a grating spacing of 43.5μm, which means the feature tolerance of the mask can cause a 1.8% velocity shift of f-SRAS experimental results at most.

- Demagnification ratio

In the SRAS systems the mask is refocused by optics on to the sample surface, hence, the pattern is also demagnified. The focus of image of the mask needs to be adjusted manually, which may cause a demagnification error. Under typical experimental parameters in f-SRAS, the demagnification ratio is 2.67, hence, the fringe spacing on the sample surface is 2.67 times smaller, and a systematic error in the velocity measurement can be introduced.

- Operating temperature

  The SAW velocity is sensitive to the operating temperature, for instance as the temperature decreases the velocity on aluminium rises by approximately 3.7m/s/°C between 22.5°C and 27.5°C [26]. The laboratories have their air conditioner set at 20°C for several hours up to and including during inspection. Accordingly, the parameters of the elastic constants of nickel and silicon are measured at 20°C; however, the models of aluminium and titanium α are calculated based on the elastic constants which were obtained at 298K (see Appendix B), and this leads the experimental data faster than the calculated model.

Overall, the first factor relates to the efficiency difference of generated modes, while the last three could cause scale factor errors in the experimental data.

5.1.1   Demagnification of Mask

A calibration test is first performed on an ideal sample which has a calibrated velocity of 2933 m/s on the f-SRAS system at 20°C; the results of which are shown in Table 5.1. The first column shows the fringe spacing on the mask and the second column shows the frequency of waves which have the same wavelength as the fringe spacing on the sample. The spacing of the fringe pattern which is projected on the sample surface is calculated by the wave frequency and SAW velocity; it is different from the value in column five, which equals the mask spacing divided by the demagnification ratio 2.67. The true demagnification ratio varies as the

different mask is used, and does not have either a fixed or linear relationship to the mask spacing.

Mask Spacing (μm)	Frequency Generated (MHz)	Calculated Spacing on Sample (μm)	Demagnification Ratio	Theoretical Spacing on Sample (μm)
116	67	43.77	2.59	43.5
145	53	55.33	2.63	54.4
203	38	77.18	2.62	76.1
304	26	117.31	2.65	114

Table 5.1: Calibration of f-SRAS system.

Figure 5.1 shows the experimental results of a single crystal aluminium (001) plane with the blue solid line, which was measured in the f-SRAS system; the curves in blue, green and red are the calculated results using material constants from three different sources [32] [33] [39] respectively; the specific values are listed in Appendix B. These three references were measured at temperatures of 20°C, 25°C and 24°C respectively; hence the calculated results in the figure have been calibrated to the experimental room temperature 20°C according to the velocity variation of 3.75m/s/°C between 22.5°C and 27.5°C [26].

Figure 5.1 shows that the calculated SAW velocity curves follow the same variation pattern with the experimental data. The experimental velocity curve of aluminium is shown by a blue solid line and is well matched to the calculated SAW velocity curve (green dots) using constants from Anderson [33]. The calculated result (in red dots) has only a 4m/s difference, and the result shown by blue dots is approximately 17m/s slower. The reason why the measured data in the figure is continuous and not discrete will be explained in next section.

In the right hand figure the experimental data are shown with a manually added velocity shift of 3% faster than the calculated results. The experimental

curve is far from the three calculated curves and has no intersection at all; it is impossible to locate the correct plane by the overlap function in such situations. This scaling error could be caused by 3μm difference on the mask, or a 0.01 error of the demagnification ratio. In reality, such a velocity shift must be considered when performing the overlap function.

(a) Without offset.　　　　　　　　(b) With offset.
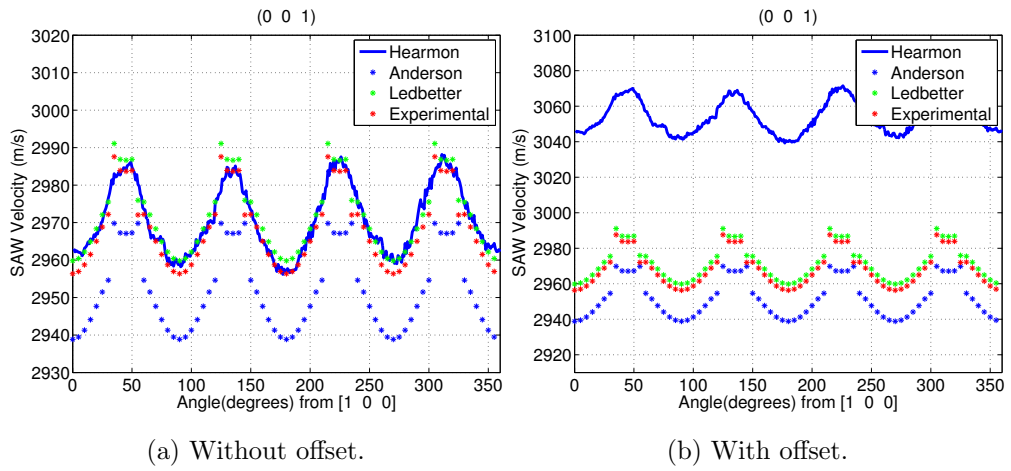
Figure 5.1: Experimental SAW velocity curve on aluminium (100) with three calculated results whose parameters were given by Hearmon [32], Anderson [33] and Ledbetter [39]. The correct experimental SAW velocity curve are on the left, and the experimental data on the right are manually added 3% velocity shift.

Figure 5.2 presents the calculated velocity on nickel plane (001) with elastic constants and density based on three different references respectively. All the curves follow the same pattern but are different numerically.
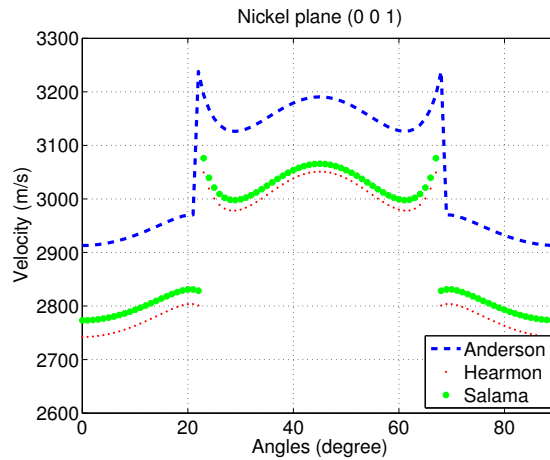
Figure 5.2: The calculated velocities of nickel plane (001); the elastic constants and density are based on three different references [33] [32] [40]. The parameters can be found in Appendix B.

In order to minimise the effect of a systematic error in the SAW velocity measurement (i.e., calibrate), a series of scaling factors were applied to the model before performing the merit function as shown in Figure 5.3. The curve of the maximum of the figure of merit is obtained as a function of the scaling factors. The peak of this curve shows the systematic error, which is 99% in this case. The velocity model is multiplied by this error value before performing the merit function on this calibrated model, which determines the grain/crystal orientation.
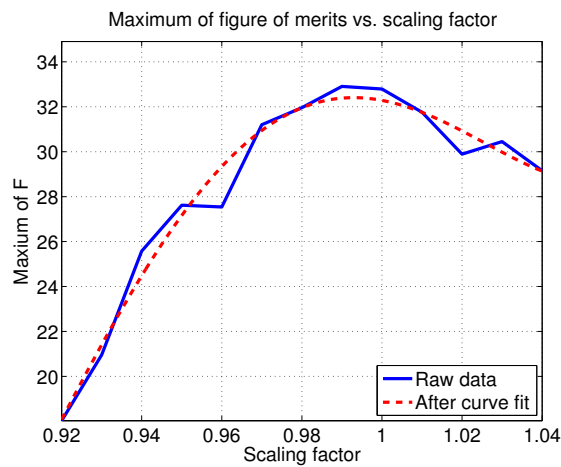
Figure 5.3: Maximum of F vs. scaling factor.

5.2   Overlap Function: Curve Fitting Results

The overlap function can be operated in two different ways which were discussed in Chapter 4; fitting to results measured from single crystal nickel and aluminium samples are shown in the following sections. 3 aluminium wafers and 12 nickel samples, all of them with known orientations, were tested. The minimum number of directions required to perform the search successfully is discussed and fitting results using various numbers of directions are presented. Finally, an R-value assessment is performed between all the SRAS fitting results and LBR results to determine the overlap functions accuracy.

5.2.1   Measured Results of Aluminium vs. Model

Figure 5.4 illustrates the experimental results from three planes—(001), (011) and (111)—on a single crystal aluminium sample, and then matches their calculated SAW velocities. The experimental data are taken every 1° over 360° using the f-SRAS system.
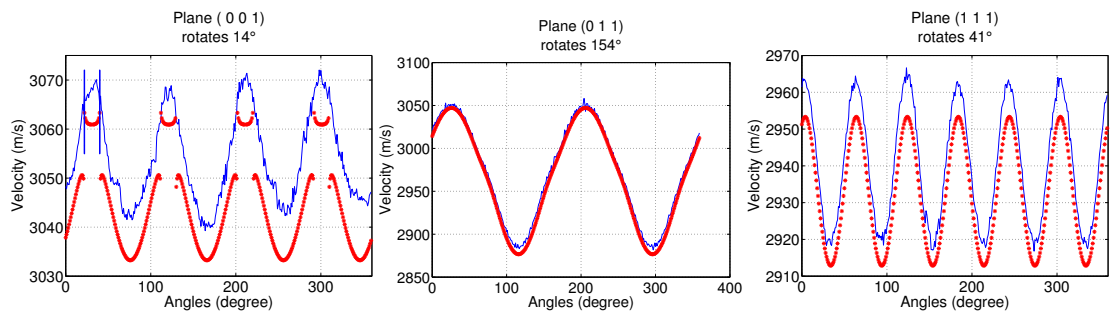
(a) Plane (001), rotated 14 de-(b) Plane (011), rotated 154 de-(c) Plane (111), rotated 41 de-
gree.   gree.   gree.

Figure 5.4: SAW velocity curves for all directions on three cuts of single crystal aluminium. The rotated angle is due to the randomly selected starting propagation direction. Experimental data are plotted as blue solid lines, and the calculated results are in red asterisks. In each graph, experimental data are plotted as blue solid lines, and the calculated results are in red asterisks [25].

In Figure 5.4a, at 22 degrees from [100] on plane (001), the wave mode at certain angles, where it transforms between SAW and PSAW, causes a mismatch between 22° to 40° (between two straight lines). The velocity variation on this plane is approximately ±14m/s; the displacements of SAW and PSAW around these angles are equally strong and dominate alternately. Due to these two factors, between these angles there are two peaks—corresponding to SAW and PSAW—appear in the experimental velocity spectrum. The Gaussian curve fit of the experimental data returns the weighted average value of SAW and PSAW, which is approximately 15m/s slower than the calculated value at these angles in the figure. The experimental data of plane (011) and (111) are in good agreement with the calculated SAW velocities except for a minor scale difference, which causes the mismatches at the extrema on plane (011) and (111). Note the calculated results in Figure 5.4 are manually shifted on the plane to match the angle of experimental data because the inspection starts at a random direction.

Results of the Overlap Function

The overlap function is performed on experimental data from 3 single aluminium wafers with known orientation; the searching results are shown in Table 5.2 and also illustrated in Figure 5.5. In method II, the FWHM of the velocity spectrum has been set as 100m/s. The R-value is used as a metric to present the disorientation between searched outputs and the known orientation of the samples.

Table 5.2 shows the R-value is smaller than 5° between the searched results and the reference of plane (001) and (111) using both methods. The R-value of plane (011) is slightly larger but still less than 9°. The ϕ component, which is the angle between two planes in the R-value calculation is the main contributor to the large R-value on plane (001) and (011) by method II and τ, which is the propagation angle to the reference direction on the plane, is larger than ϕ in the other results shown.

Samples	Overlap Function I				Overlap Function II			
	Results	R	ϕ	τ	Results	R	ϕ	τ
sample 1: (001) 14°	(0 0 1) 14.09°	0.09°	0°	0.09°	(0 0.05 1) 14°	2.86°	2.86°	0°
sample 2: (011) 154°	(1 0.1 1) 67.67°	6.70°	4.04°	5.35°	(0.95 0.2 1) 70°	8.77°	8.38°	2.6°
sample 3: (111) 41°	(0.9 0.95 1) 43.76°	4.19°	2.46°	3.39°	(1 1 1) 40°	1°	0°	1°

Table 5.2: R-value of the two types of overlap functions results of 3 aluminium samples.

The experimental velocity surface of three planes and searched results are plotted against each other in Figure 5.5. It can be seen the results by both methods on plane (001), (011) and (111) are all well matched.

(a) Method I: sample 1.   (b) Method II: sample 1.

(c) Method I: sample 2.   (d) Method II: sample 2.

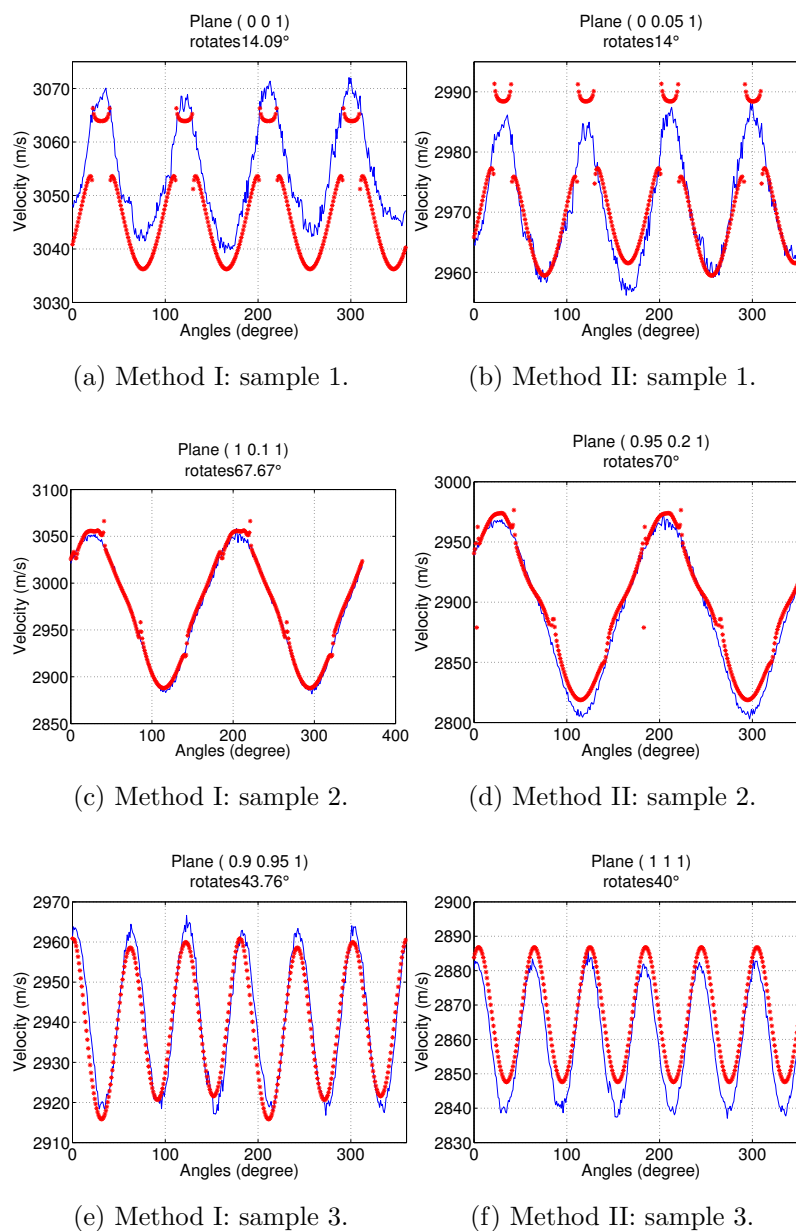(e) Method I: sample 3.   (f) Method II: sample 3.

Figure 5.5: Curve fitting results of 3 aluminium samples by two types of overlap function. The left column is from method I and the right column shows the results of method II. The red asterisks, which represent the searched output, are plotted to match the experimental velocity surface (blue lines) in each figure.

5.2.2   Curve Fitting of Nickel

The results for 12 samples of nickel tested by the k-SRAS system are shown. The experimental data are taken every 5° over 180° and all of the velocities on these angles are applied in the searching algorithm.

Table 5.3 gives the R-value between the LBR results (see Appendix G) and the two methods used to perform the overlap functions of the 12 samples. The R-value of method I varies between 0.5° and 6.54°, while method II varies between 3.02° and 16.93°. The vast majority of the R-values were found to be within the industrial acceptable standard of 8° [18].

The mismatch of method II results are larger than method I. Comparing either the R-value, or ϕ or τ components, only two of those R-values when using method II are smaller than using method I. Method I was found to have a better fit than method IIas indicated by the lower R-values. As defined in Chapter 4, ϕ and τ represent the differences between planes and the reference direction respectively; the larger of these two values, the more it contributes relatively to the R-value.

No.	Overlap Function I				Overlap Function II			
	Results	R	ϕ	τ	Results	R	ϕ	τ
1	(0.045 0.155 1) 30.1°	5.79°	1.49°	5.6°	(0.1 0 1) 24.28°	3.23°	3.22°	0.22°
2	(0.125 0.2 1) 45°	4.5°	0.2°	4.5°	(0.35 0.2 1) 131.59°	10.66°	10.6°	1.09°
3	(0 0.245 1) 70.45°	2.56°	2.17°	1.35°	(0.2 0.2 1) 166.63°	9.67°	6.08°	7.53°
4	(0.1 0.045 1) 149.35°	6.54°	1.94°	6.25°	(0.3 0.15 1) 148.53°	12.73°	11.53°	5.43°
5	(0.2 0.095 1) 138.95°	4.07°	3.33°	2.35°	(0.35 0.05 1) 139.70°	11.28°	11.17°	1.6°
6	(0 0.05 1) 87.35°	4.36°	0.96°	4.25°	(0.1 0 1) 87.96°	7.55°	5.78°	4.86°
7	(0.15 0.105 1) 17.9°	0.8°	0.77°	0.2°	(0.3 0.2 1) 103.35°	11.56°	10.72°	4.35°
8	(0.045 0.045 1) 74.1°	3.85°	3.77°	0.8°	(0.05 0.1 1) 75.46°	6.28°	6.26°	0.56°
9	(0.145 0 1) 19.25°	3.11°	2.96°	0.95°	(0.2 0.15 1) 111.84°	3.02°	2.54°	1.64°
10	(0.22 0 1) 20.6°	0.5°	0°	0.5°	(0 0 1) 26.52°	16.93°	15.7°	6.42°
11	(0.04 0.09 1) 125.1°	0.31°	0.29°	0.1°	(0 0.2 1) 124.06°	5.69°	5.61°	0.94°
12	(0.28 0.1 1) 17.95°	6.2°	5.71°	2.41°	(0.3 0.1 1) 18.09°	7.23°	6.77°	2.55°

Table 5.3: R-value of LBR results and the two types of overlap functions results of 12 nickel samples.

Figure 5.6 show the fitting results of two types of overlap function. In all figures showing both of these methods, the determined plane is plotted as black asterisks over the experimental velocity surface spectrum. It can be observed that the method I has better fit (the black asterisks fall on the brightest part of the velocity surface spectrum) of determined plane to the experimental data than method II.

(a) Method I: sample 10.

(b) Method II: sample 10.

(c) Method I: sample 11.

(d) Method II: sample 11.
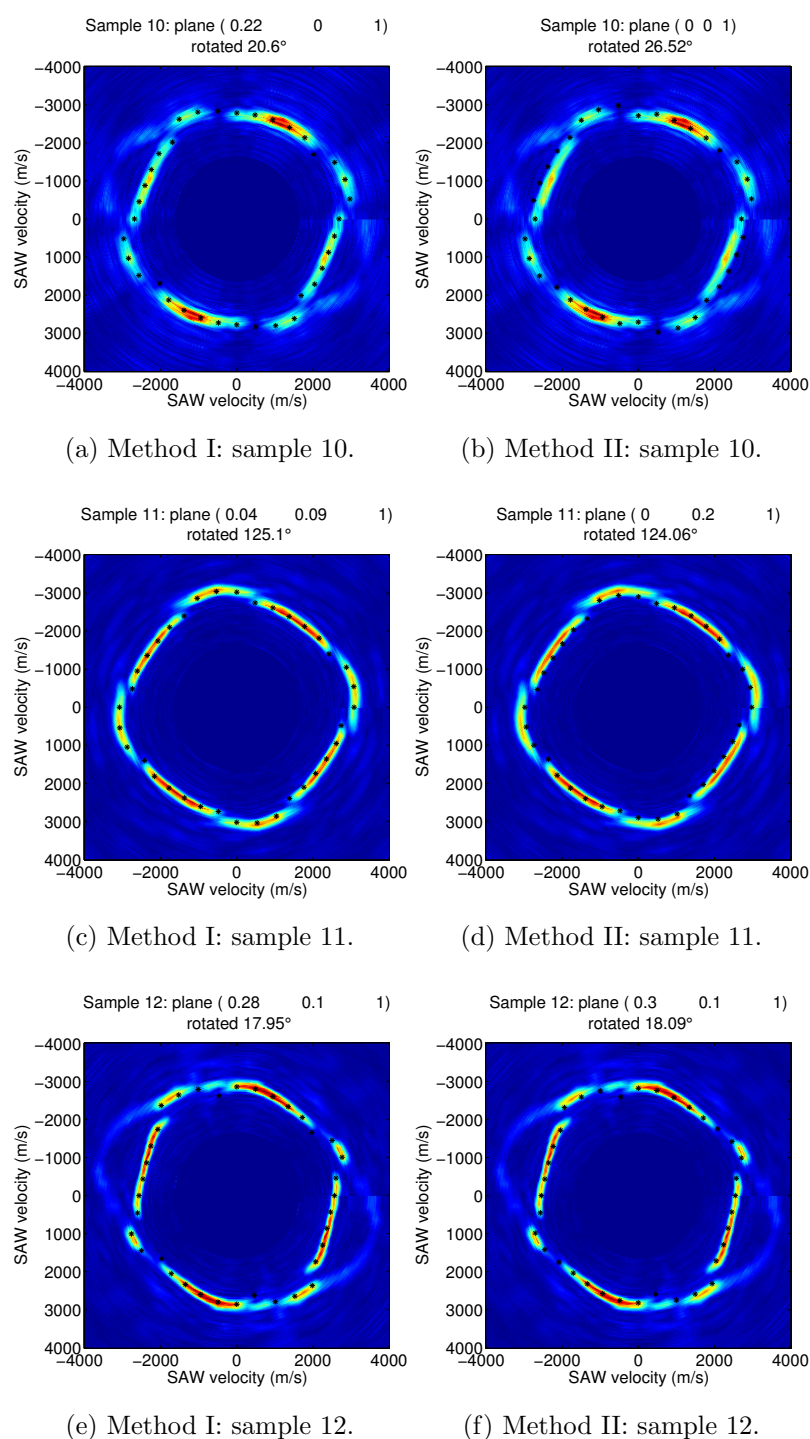
(e) Method I: sample 12.

(f) Method II: sample 12.

Figure 5.6: Curve fitting results of 3 nickel samples by two types of overlap function. The left column is from method I and the right column shows the results of method II. The black asterisks, which represent the searched output, are plotted to match the experimental velocity surface spectrum in each figure.

5.3 Search Algorithm Performance vs. Numbers of Measured Angles

To increase the efficiency of the system we determined the minimum number of directions needed to find the crystallographic orientation. The search algorithm results of the nickel samples when varying the number of directions measured are discussed in the following section.

Only the overlap function I is implemented since the previous results shown have indicated that method I has a superior performance in orientation determination. In addition, if two modes appear in the experimental result—especially when they are equally strong in some cases—the average velocity of the two modes rather than the strongest one is applied in method II, hence, the information may be distorted, while method I prevents this error. This is the same reason why the least-squares method is not used as a search algorithm.

Figure 5.7 shows the velocity surface spectrum measurements around 360° with 5° spacing on 3 single crystal nickel samples with corresponding curve fitting results (using method I) which are determined by Equation 4.25. The curve fitting results in the figure are based on the experimental data using either 36 (Figure 5.7b), 9 (Figure 5.7c) or 6 (Figure 5.7d) directions over 180°. All searched planes are in agreement with the experimental data. The searching results based on 9 and 6 directions are also very close to the LBR results.

(a) Experimental data

(b) 36 directions
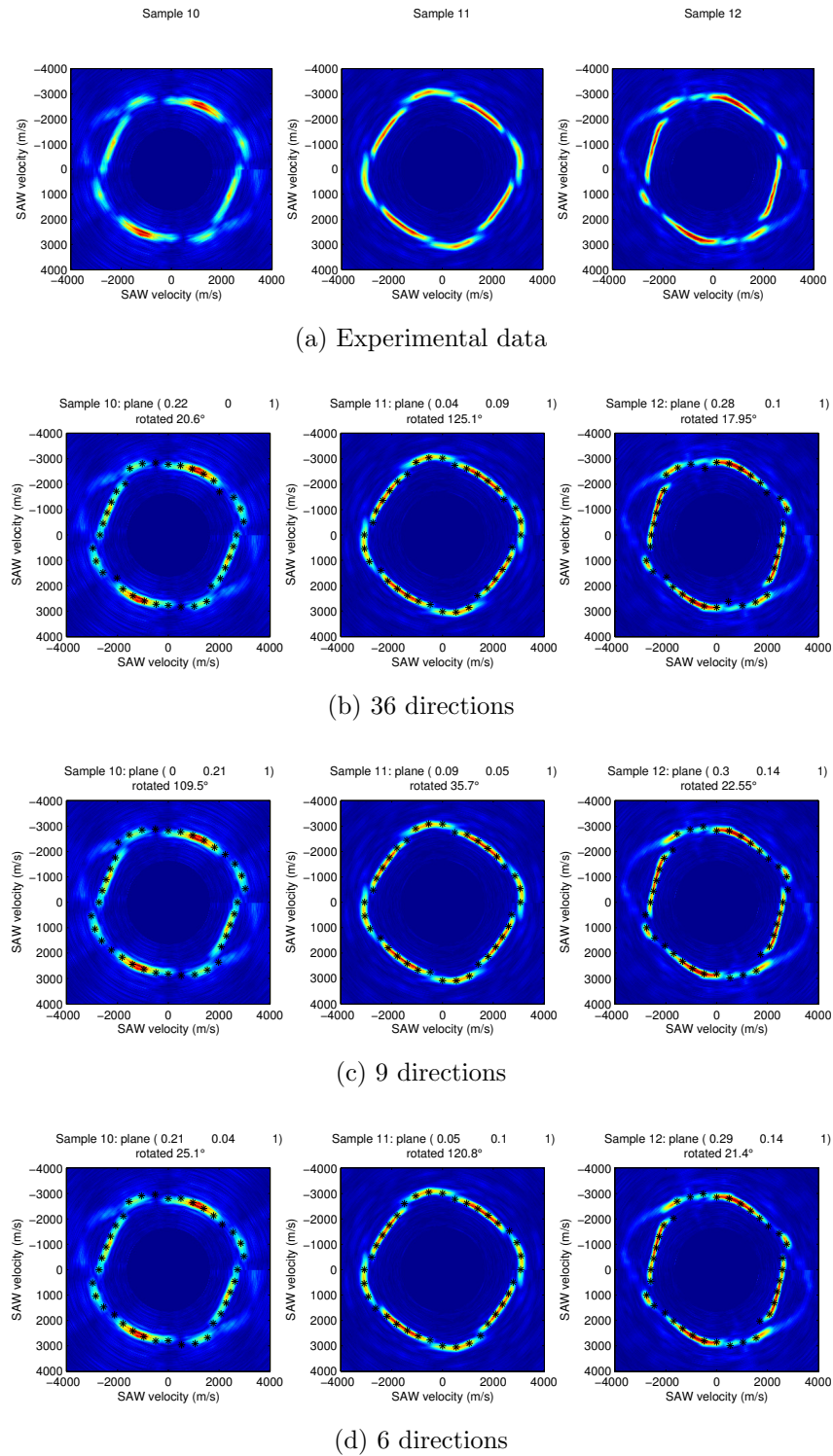

(c) 9 directions

(d) 6 directions

Figure 5.7: Curve fitting results of single crystal nickel. Three columns represent three samples; first row is the experimental data by SRAS technique, second strongest mode vaguely appears in sample 10 and 12; the second to forth row are the matching results (asterisks) when 36, 9 and 6 directions are used respectively.

Sample's Name and LBR Results	Number of Directions	SRAS Results	R-value	ϕ	τ
10: γ=-10.9°, δ=-11.4°, κ=18.2°.	36	(0.22 0 1) 20.6°	0.5°	0°	0.5°
	9	(0 0.21 1) 109.5°	3.89°	3.84°	0.6°
	6	(0.21 0.04 1) 25.1°	5.02°	0.48°	5°
11: γ=-5.7°, δ=0.5°, κ=34.9°.	36	(0.04 0.09 1) 125.1°	0.31°	0.29°	0.1°
	9	(0.09 0.05 1) 35.7°	1.9°	1.77°	0.7°
	6	(0.05 0.1 1) 120.8°	4.36°	1.16°	4.2°
12: γ=-14.0°, δ=1.7°, κ=15.5°.	36	(0.28 0.1 1) 17.95°	6.2°	5.71°	2.41°
	9	(0.3 0.14 1) 22.55°	10.09°	7.28°	7.01°
	6	(0.29 0.14 1) 21.4°	8.95°	6.77°	5.86°

Table 5.4: R-value of the LBR and SRAS results of 3 nickel samples in different numbers of directions.

Table 5.4 shows the R-value of 3 SRAS results compared to the LBR results, with ϕ and τ indicating the difference between the planes and reference directions. Where only 9 and 6 directions are used (with 20° or 30° intervals), only sample 12 have an R-value larger than the typical industrially accepted standard 8°.

5.4 Error and Uncertainty Analysis

The R-value analysis of 12 single crystal nickel samples, where the number of directions of the experimental data measured being 36, 9 or 6, are shown in Figure 5.8. LBR results are used for reference. The graph shows the statistical variation of the R-values when fewer propagation directions are used in the experiment. When 36 directions of data are used 98% of the R-values are less than 8°, which is the 'industry acceptance limit' of this material. When 9 directions are applied this drops to 86% of the R-values being less than 8°. In the case of 6 directions with a 30° interval, only 79% of the results have R-value less than 8°.

These statistics are based on the curve fitting results of the overlap function method I. The 36-direction curve fitting results of all 12 samples can be found in Appendix F.
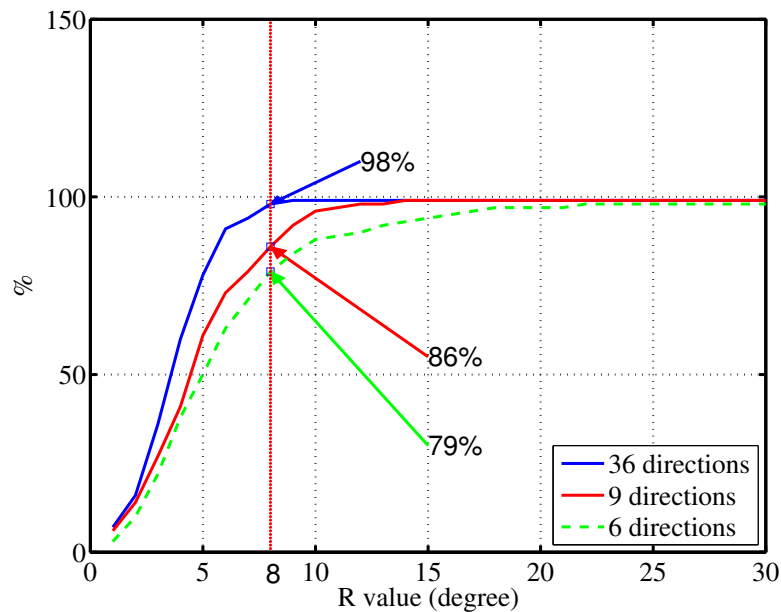

Figure 5.8: Error of curve fitting strategy. The blue solid line, red solid line and green dash line display the percentages when 36, 9 and 6 directions of data are used respectively.

It deserves note that, on certain planes there may be some angles where two wave modes jump and these may have velocity information missing. When the 9
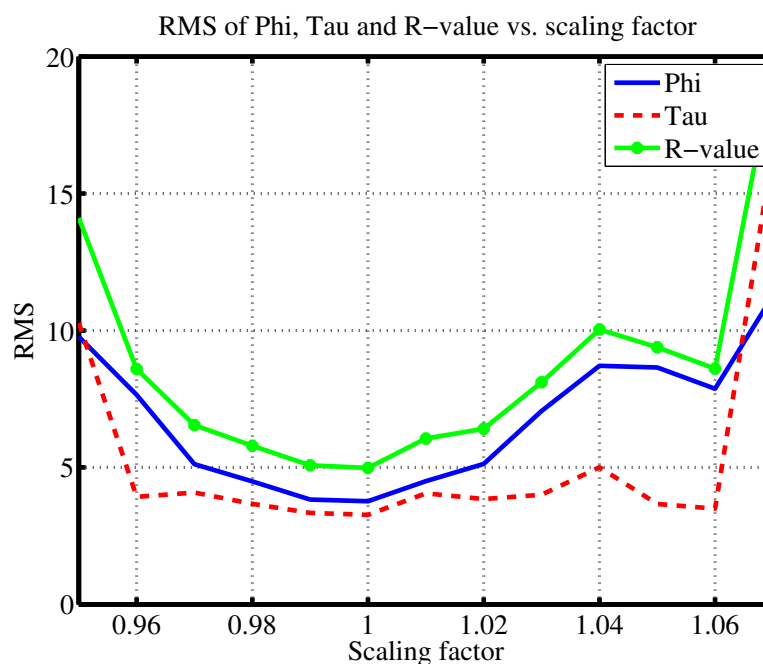
Figure 5.9: A serials of scaling factors are multiplied with the SAW model before performing the search algorithm; the RMS of ϕ, τ and R-value of 12 samples are shown as a function of the scaling factor.

or 6 directions searching algorithm is performed, the accuracy of the curve fitting results degenerate if such directions are selected and no effective information is provided.

As discussed in the previous chapter, a scaling factor is used in the merit function to reduce or eliminate the systematic error (i.e., calibrate the model); it also described how miscalibration can influence the search algorithm. The RMS of ϕ, τ and R-value of all samples as a function of the scaling factor are illustrated in Figure 5.9; comparing ϕ to τ we find τ is less sensitive to the velocity shift of the experimental data. The RMS of the R-value gradually increases if the scaling factor shifts from its minimum (a scaling factor of 1). If the scaling factor shift by approximately $\pm 3.5\%$ from its minimum, then the RMS of R-value will be larger than $8°$. This scaling factor analysis matches the performance of the search algorithm evaluation described in Chapter 4.4.2 which was $\pm 3\%$.

5.5 Orientation Determination on Multigrain Materials

The previous section on both nickel and aluminium were performances on single crystals with known orientation. However, for the orientation determination of multigrain materials, only one additional step needs to be performed. This process will be detailed for a multigranular nickel sample. Firstly, two standard SRAS velocity images are acquired on the nickel sample, whose grain orientations are unknown, to locate the grains and determine their size. This is essential because the SAW velocity of two or more adjacent grains might be similar, hence, they may be treated as one grain. Such coincidences are eliminated by scanning over two direction. Secondly, we perform SRAS again on the directions with an interval of $5°$ over $360°$ (or $180°$) on specific grains. Thirdly, we use an overlap function to determine the orientation of grains.

Figure 5.10b illustrates the SRAS results over the whole surface of a nickel sample with $360°$ results. The velocities maps show the sample to have two large grains A and B of different orientations in this case. The velocity surface spectrum of these two grains are shown in Figure 5.10a and Figure 5.10c, along with their corresponding curve fitting analysis. Grain A is determined to be plane (0.1 0.25 1) rotated $34.61°$ from its reference direction [1 -0.01 -0.1]; grain B is the plane (0.15 0.2 1) rotated $44.14°$ from the reference direction [0.99 -0.01 -0.15]. SRAS results distinguish the individual grains and the R-value shows the disorientation to be $9.86°$, which is over the industry limit $8°$ [18] of nickel, meaning they would be considered as grains with 'different' orientation.
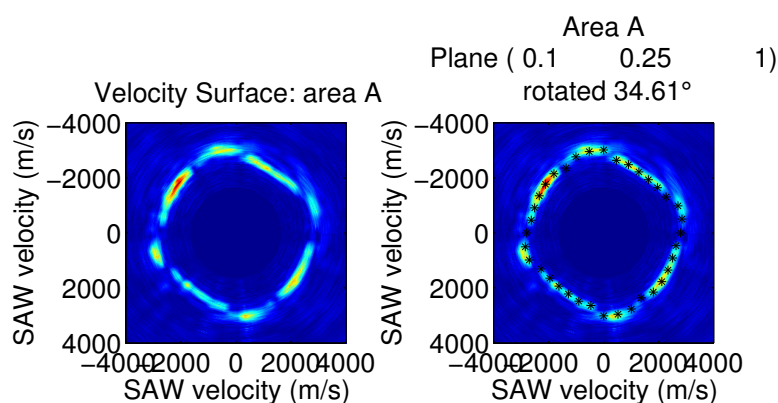
(a) Area A with curve fit result (asterisks).
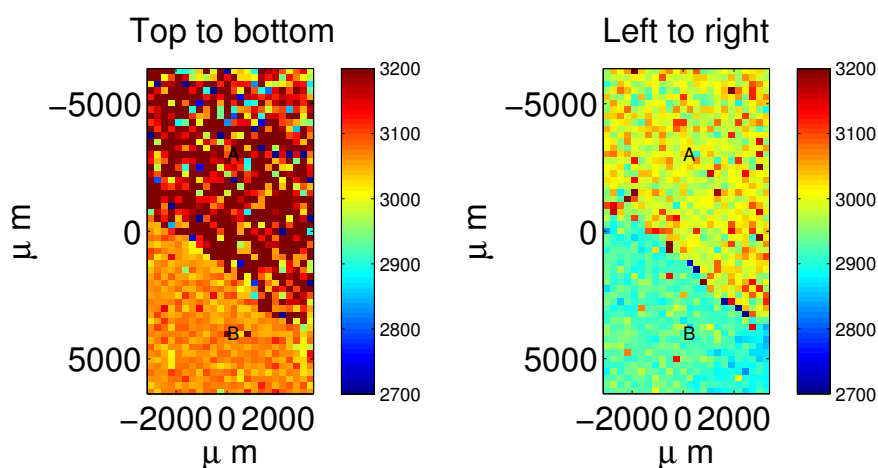
(b) Nickel Sample: pixel size 250μm.
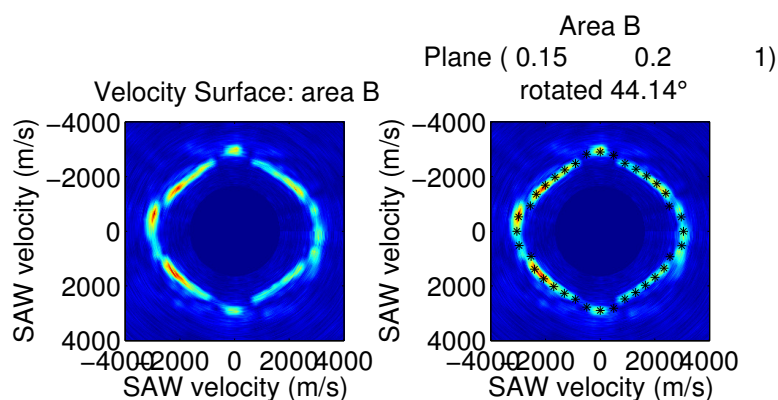
(c) Area B with curve fit result (asterisks).

Figure 5.10: Middle: SRAS on nickel sample indicates there are two grains. Top: Velocity surface spectrum on area A with curve fit result. Bottom: Velocity surface spectrum on area B with curve fit result.

5.6 Titanium α Model vs. Ti-685

K-SRAS scanning has been applied over 12 directions on a Ti-685 sample over $180°$ with a $15°$ interval; the velocity maps are shown in Figure 5.11. 12 large grains on the sample surface are selected and labelled in the Figure 5.12a. The velocity of each grain at each direction is calculated as the average velocity value for all pixels of the image of the corresponding grain.
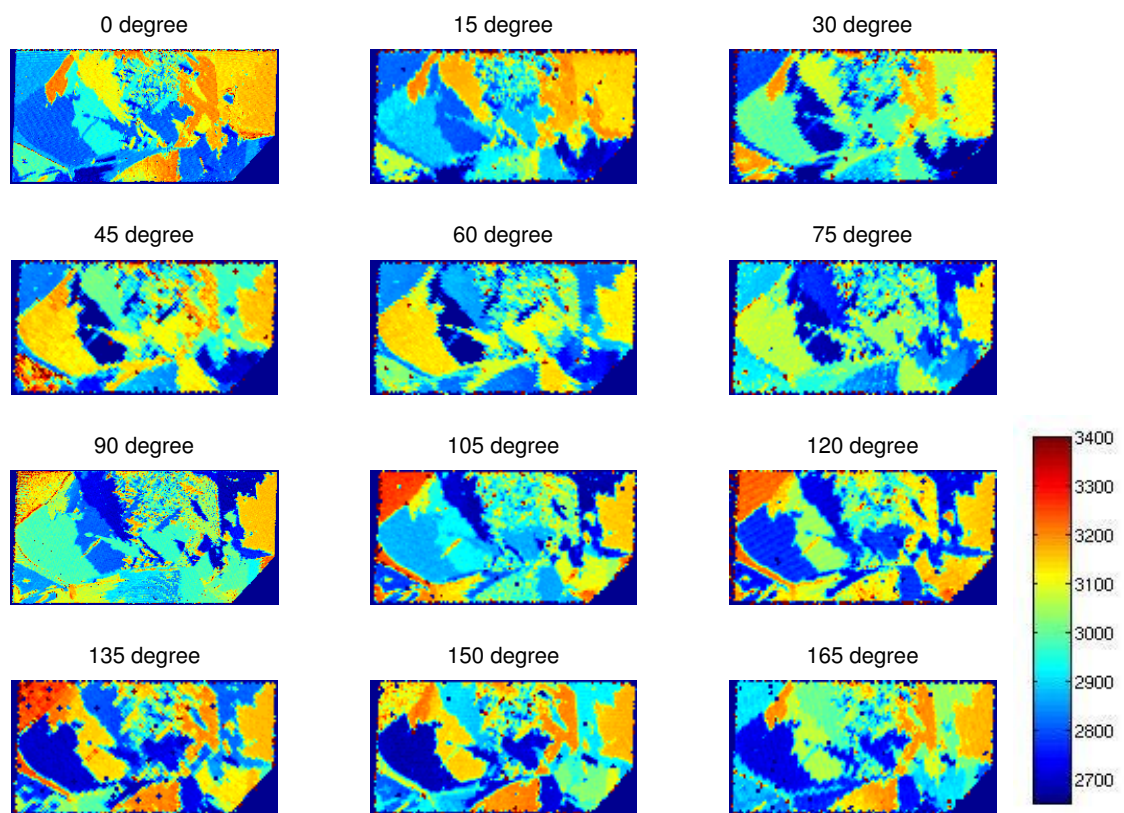

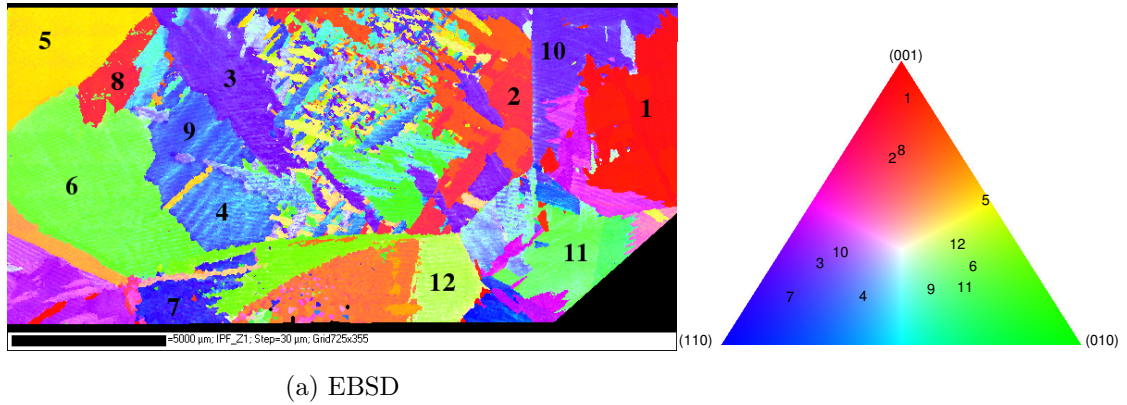Figure 5.11: Velocities of 12 directions of Ti-685 sample by k-SRAS.

(a) EBSD

Figure 5.12: EBSD scan result of Ti-685 sample.

Figure 5.12 shows an EBSD (which gains crystallographic information by impinging electrons on to the sample and analysing diffraction patterns [22]) orientation image for this sample. Because the original EBSD data from which the orientation image is derived is not available (the EBSD scan was conducted by researchers at the University of Swansea and only this RGB picture was available), the orientation of the 12 grains are estimated based on the EBSD image and the IPF alone.

Grain Number	Orientation in Miller Index	Grain Number	Orientation in Miller Index
1	(0.03 0.08 1)	2	(0.17 0.32 1)
3	(0.82 1 0.60)	4	(0.57 1 0.31)
5	(0 0.92 1)	6	(0.17 1 0.47)
7	(0.88 1 0.30)	8	(0.13 0.28 1)
9	(0.41 1 0.45)	10	(0.72 1 0.85)
11	(0.20 1 0.32)	12	(0.20 1 0.71)

Table 5.5: The orientation of 12 grains of Ti-685 sample are estimated according to the RGB value of EBSD image.

The experimental SRAS velocity data from each grain are fitted to the predicted model velocities—based on the EBSD-derived orientations—in Figure 5.13 and

Figure 5.14. To be clear: the orientations were not derived from the SAW velocity data; the measured SAW velocities are compared to the predicted SAW velocities based on the known orientations derived from EBSD. They share similarity with one of the modes or partially of both modes; this can be observed clearly on grains 4, 10 and 12. On grains 1, 2 and 8, experimental velocities follow the variation pattern of the model with a velocity scaling error of less than 3% in Figure 5.13. Two modes appear at certain angles simultaneously on the velocity surface spectrum of grain 9, hence, two peaks occur in the velocity spectrum. In this case the calculated velocity is determined as the peak of the Gaussian curve on the velocity spectrum and the intermediate value of the peaks is returned. Therefore, at certain angles of grain 6, 9 and 11, the experimental velocity is the average value of the two calculated velocities in Figure 5.13.

Velocity mode jumping occurred frequently over all 12 grains and can be observed in Figure 5.14. The discontinuity of the velocity spectrum at the middle right of each figure indicates the direction where the measurements start.

Ti-685 is an α/near-α titanium alloy which is mainly hexagonal in structure but contains a small amount of β phase crystal, thus the elastic constants which are used to calculate the model are not 100% correct. Furthermore, without considering the SAW generation and detection mechanisms in detail, the velocity model is not established maturely; the uncertainty in the calculated 'dominant' mode/modes is the main reason for the mismatch. Also the interval between the calculated model planes is 2.5°. The closest plane to the EBSD results is shown in both figures rather than the actual planes derived from the EBSD results.

This section obviously is an uncompleted study, but it highlights some of the challenges involved in predicting the acoustic velocity response on some materials, which will be discussed further in the next chapter.
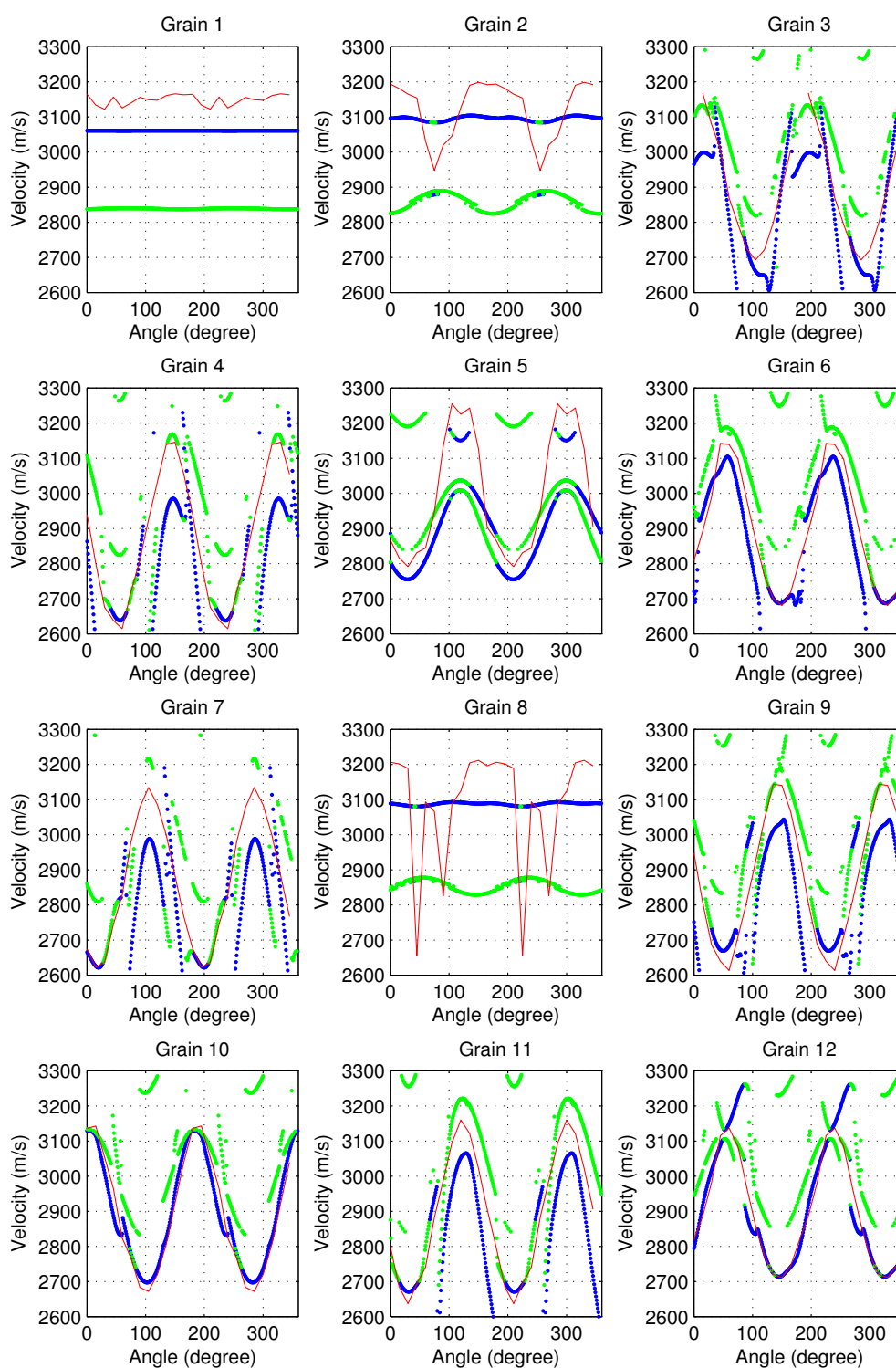
Figure 5.13: The SAW velocity surface of the 12 grains of Ti-685 (red solid line) are plotted against the Ti-α model. The calculated first and second 'dominant' modes of the Ti-α model are plotted as blue and green dots respectively.
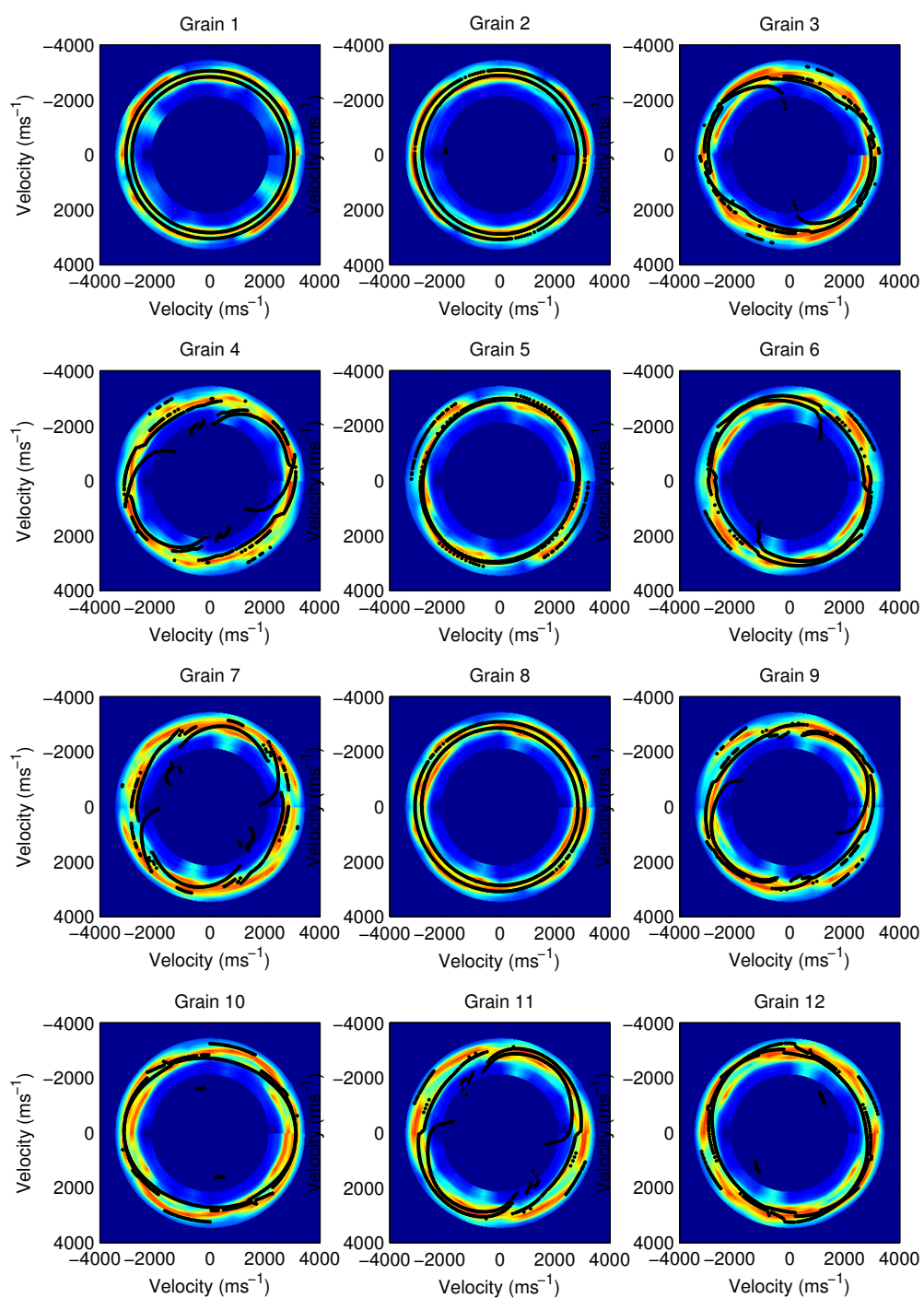
Figure 5.14: The SAW velocity surface spectrum of the 12 grains of Ti-685 are plotted against the Ti-α model (black asterisks).

5.7 Summary

The SRAS results of known planes of nickel and aluminium samples are in good agreement with the calculated model velocity. Three planes of aluminium crystals were determined by the overlap function with an error of less than 8.77°. Both methods of the searching algorithm also work efficiently on nickel samples, with error close to 8° compared to the LBR results.

The velocities of 36 directions over 180° of each sample plane were applied in the above searching algorithm. 98% of these results have an R-value of less than 8° compared to the LBR results. If the number of directions measured is reduced to 9, 86% of the reaching results have an error of less than 8°. The figure of error of less than 8° drops to 79% when 6 directions are applied. There is no significant change between 36-directions and 9-directions, but considerable degeneration appears when only 6-directions are measured.

A fundamental demonstration of how to determine the crystallographic orientations of a multigranular sample has been illustrated. Nickel and titanium α samples were examined. For cubic nickel samples the surface grains and their orientations were determined and illustrated. For the results on Ti-685 sample, which has a primarily hexagonal structure, the experimental data were plotted against the predicted Ti-α model; the similarity of modes' behaviour can be observed between them. However, because of the complexity of SAW behaviour for this type of crystals, further work needs to be conducted to elucidate how we may determine the 'dominant' mode/modes, and thus permit the inverse problem to be solved.

Chapter 6

Discussion and Future Work

The previous chapter confirmed that the crystallographic orientation determination using SRAS gave better than 10° accuracy at 95% repeatability, when 36 or 9 SAW propagation directions are used in the search algorithm. This is a higher measurement uncertainty of the R-value compared to the Laue back-reflection technique, which at 95% confidence level is $\pm 1.5°$ [18]. In this regard, there is still room for improvement in the SRAS technique and specifically the search algorithm. So far the application and analysis has mainly focused on single crystal nickel, this technology should be expanded to other materials. Hence, several issues are highlighted for discussion, first on the modelling and then the data processing.

6.1 Modelling

6.1.1 Generation/Detection Model

As stated in the previous chapter, Rayleigh waves are excited with great efficiency by a laser working in the thermoelastic regime, thus the displacements in the vertical and longitudinal directions are considered in the modelling. Sinclair [41] described the calculation of the surface displacement by a point source, Dike [42] and Royer [13] also investigated the SAW displacements which are excited by a

pulse laser. Computer programs which are used to simulate the wave generation and propagation are described by Spicer [43] and Sanderson [44]. This research would provide a solid foundation to more accurately predict which wave modes are efficiently excited by the SRAS instrumentation, improving the accuracy of the model and by implication the inversion to determine the orientation.

The displacement amplitude is proportional to the incident optical energy if a point-source works in the thermoelastic regime; and the directivity pattern of duraluminum is given as an example in Figure 6.1 [13]. The longitudinal waves radiate as a lobe and reach a maximum at approximately 65° away from the normal of the surface. The shear waves have a maximum at approximately 31° and a small 'maximum' at 62°. Hence the displacements on vertical, longitudinal and transverse directions can be simulated if the laser working condition and the power level are known. We can predict how many modes are generated, the behaviour of the propagation of these waves, also how many of them can be observed efficiently by the different possible detection techniques.

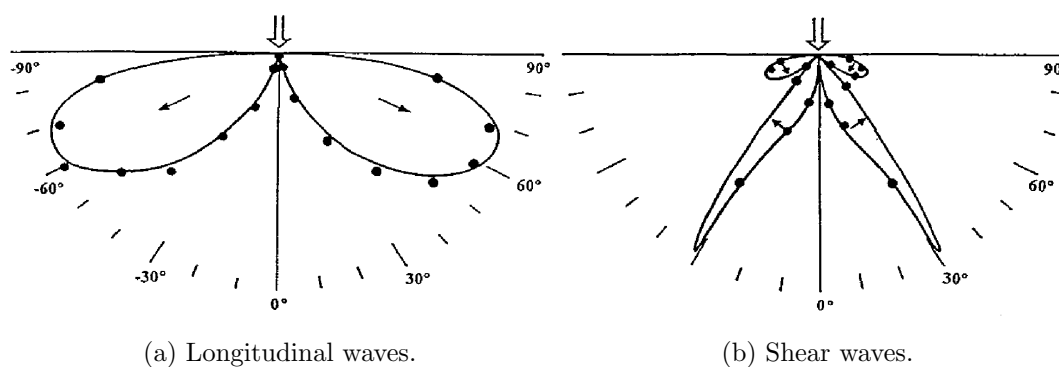(a) Longitudinal waves.   (b) Shear waves.

Figure 6.1: The directivity pattern of laser generation in thermoelastic regime of duraluminum [13].

6.1.2 Multiple Modes

Figure 6.2 shows the SRAS results on a grain of titanium α sample. It can clearly be seen there are two modes at several SAW propagation angles, with approximately

equal signal level. The modes match the predictions in the model, however at this point we can not confirm in what conditions more than one mode can be observed. As described in the previous section, on the one hand the system response relates to the efficiency with which the different SAW modes are excited using thermoelastic laser generation, and the motion that the optical detection technique is sensitive to, which is generally out-of-plane motion. On the other hand, it relates to the model calculations: all the calculated modes satisfy (or nearly satisfy) the boundary conditions, but the different acoustic modes have different amplitudes of particle motion. By predicting more accurately the response of the measurement system as a whole, it should be possible to use more than the most dominant mode (as determined by the model) to match against the measured acoustic spectra. This will make the inverse problem more deterministic, as the uniqueness of each plane is increased.
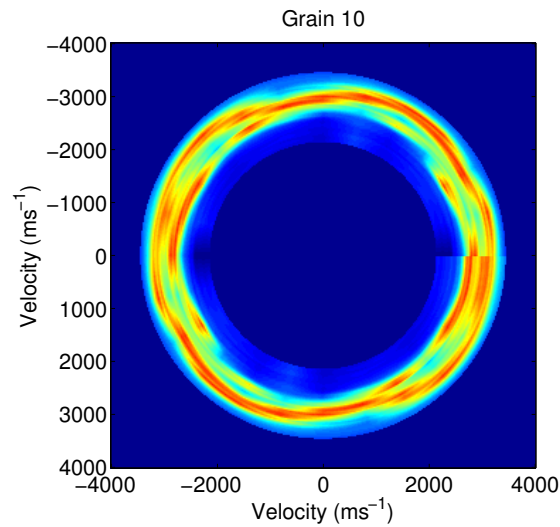

Figure 6.2: The experimental results of titanium α grain. Two modes are observed at several angles and equally strong.

6.1.3 Higher Precision of Model

The angle between the normals of two adjacent planes in our model is 2.5°. The model can be recalculated in a finer intervals, to 1° or perhaps 0.5° between planes

in order to increase the accuracy of the merit function. There is no technical problem for this issue, only the processing time required, which depends on the computer capability. Note that the forward model is a one-time calibration, so the processing time limitation is particularly non-critical.

6.2 Data Processing: Multiple Modes

This is the same issue mentioned earlier but needed to be solved from a different point of view. In overlap function method II, the experimental velocity was determined by either by applying a Gaussian curve fit on the raw data spectrum, or by finding the highest peak of the whole spectrum. In the case of two modes detected in the spectrum $A(v)$ shown in Figure 6.3, the Gaussian curve fit would give the weighted average velocity of both modes, and the single peak detection method would only return the velocity of the highest mode. Least square or polynomial curve fitting could be used to to smooth the curve and determine the maxima corresponding to the modes velocities to determine two or more 'dominant' modes. The technique needs to be *robust* enough to determine $v_n(\theta)$, where $n \geq 1$ i.e. an unknown number of peaks. In fact, there is an argument for permitting $n = 0$ where, because of the measurement system response, in certain propagation directions the measured acoustic spectrum has a very low energy content.
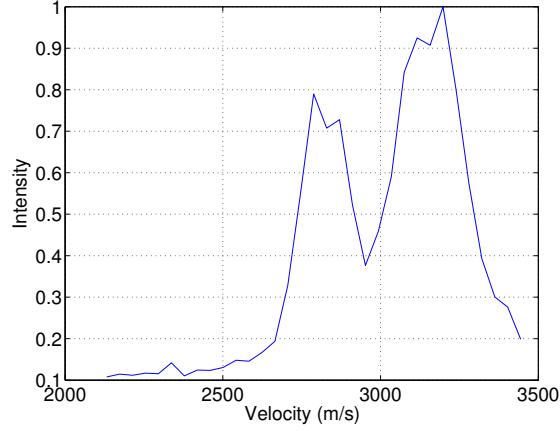
Figure 6.3: Two wave modes appear in the experimental spectrum $A(v)$. The signal intensities are plotted as a function of velocities.

6.2.1 Search Algorithm of Strongly Isotropic Materials

The least-squares method was not utilised in the search algorithm because of the discontinuous nature of the wave modes (in different propagation directions of the same plane) in either the calculated model and the measured results. After the velocity models are well established by considering the generation efficiency and detection sensitivity, if the velocities appear without random mode jumping, a least-squares function is given

$$F'(h, k, l, \theta) = \sum_{\phi=0}^{\phi=\frac{n-1}{n}\pi} (v_{(\phi)}^e - v_{(h,k,l,(\phi-\theta))})^2, \ (n = 1, \, 2, \, 3, \, ...) \tag{6.1}$$

where $v^e(\phi)$ is the velocity measured experimentally, and $v(h, k, l, \theta)$ is the calculated velocity. The minimum of this function will point out the matched plane. By combining the function 4.25 and function 6.1, the modified overlap function III can be developed as

$$F(h, k, l, \theta) = \sum_{\phi=0}^{\phi=\frac{n-1}{n}\pi} \frac{A(\phi v_{(h,k,l,(\phi-\theta))})}{(v_{(\phi)}^e - v_{(h,k,l,(\phi-\theta))})^2}, \ (n = 1, \, 2, \, 3, \, ...) \tag{6.2}$$

The location of the maximum of this overlap function III would give the matched plane.

The modified function would be useful for reducing the error of the search algorithm. The accuracy and reliability of this new search algorithm needs further investigation. New search algorithms also should be discussed besides the improvement of the overlap function.

Chapter 7

Conclusions

This thesis introduced a crystallographic orientation determination method based on a laser ultrasonics technique termed SRAS. SRAS is non-contact and non-destructive to samples, and uses lasers to generate and detect SAWs; the phase velocity of these SAWs changes depending on the crystal orientation and the characteristics of material.

Two slightly different approaches to performing SRAS measurements have been described in Chapter 2. One approach, K-SRAS, works by firing a laser beam with a fixed intensity modulation frequency through an SLM, this forms a fringe pattern with even spacing on the sample surface. SAWs are generated by the pattern which also works as a filter: as the fringe spacing is changed, the detected SAWs have the highest amplitude if the their wavelength matches the fringe spacing. Another method, f-SRAS, uses a broadband laser instead; a chrome coated photomask is imaged onto the sample surface producing a fixed grating pattern, which again works as a filter. The generated SAWs, which have a wavelength determined by the grating spacing, are detected and the velocity of SAW is determined by the peak frequency of the acoustic spectrum. Both SRAS methods show 0.03% standard deviation in velocity variation by testing isotropic aluminium coated glass. Velocity measurements in two orthogonal directions on titanium alloy and aluminium samples have been presented as velocity maps and compared with EBSD;

the results are shown in Chapter 3. The lateral resolution of k-SRAS is $150\mu m$, the scan speed is 11 pixels/second. F-SRAS scans at a speed of 238 pixels/second have been presented; the spatial resolution for these measurements is of the order of $400\mu m$, and can be significantly reduced by using different masks with fewer lines at shorter wavelengths. Both methods are capable of producing high quality quantitative images of SAW phase velocity, and hence reveal the material microstructure with grain sizes down to a few hundred microns, providing excellent contrast for differently orientated grains.

A SAW velocity model is calculated according to the elastic constants and mass density of the material, and is described in Chapter 4, in sections 4.1 and 4.2. An iterative search algorithm is performed to determine the solutions which satisfy the wave equation and the boundary condition simultaneously when the propagation direction of SAW is defined. These solutions correspond to the wave modes which possible exist on the half-infinite surface of the medium. The corresponding displacement of each mode in three principal particle oscillation directions—longitudinal, transverse in-plane and vertical—are calculated. By considering the laser ultrasonic SAW generation mechanism and the SRAS system detection sensitivity, the strongest wave mode is selected according to the largest amplitude of the vector sum of longitudinal and vertical displacements. For different crystal symmetries, the velocity surface of all the planes that do not contain redundant information are calculated using the SAW velocity model. The model of aluminium, nickel, Ti-β and Ti-α are demonstrated in this chapter.

In later sections of Chapter 4, an overlap function is introduced as an inversion algorithm to link the SRAS results and the SAW velocity model. Two implementations/methods of this overlap function are demonstrated, for use under the different circumstances. Method I is specially designed for SRAS results—or velocity measurements from other techniques—which present the tested outcome as a velocity map over 360°. In the case where only a velocity surface, rather than an acoustic spectrum, is available—for example by other inspection techniques—method II is

more appropriate for orientation determination. This search algorithm has been evaluated on simulated experimental results; the R-value is introduced as a indicator to show the difference between the simulated plane and the plane as determined by the algorithm. The simulation parameters—SNR, FWHM of the Gaussian filter, and velocity shift/scaling error—are varied within a certain range to locate the best combination of the smallest error below a common industrial limit of 8° disorientation. Within the typical SNR and FWHM of the SRAS spectrum, the velocity shift would have to be less than 1.2% for nickel to achieve the correct results with errors smaller than 4°. Due to the strong isotropy of aluminium, this figure is down to 0.3% to maintain the error less than 3°.

Orientation determination has been demonstrated on aluminium and nickel single crystal samples with known orientations by the overlap function, and has been presented in Chapter 5. The orientation of two of the aluminium samples with planes (001) and (111) were correctly determined by better than 4.19° error. The calculated plane of the third sample (011) had a larger error (but still smaller than 8.77° by both overlap function methods) because of its common 2-fold symmetry and the low anisotropy of aluminium. The results for 12 nickel samples are compared to LBR; the statistics show that 98% and 86% of the differences between SRAS and LBR orientation measurements are less than 8° when 36 or 9 SAW propagation directions are used in the search algorithm. Multiple-grain samples of nickel and titanium α have been tested, and the search results broadly agree with the calculated model. However, further work is still needed to solve the case when multiple modes are 'dominant' in certain crystal cuts.

Finally, some thoughts and issues are brought up in Chapter 6 in order to improve this orientation determination technique. They are discussed in both aspects of modelling and data processing. Even though a few problems still need to be solved, SRAS has great potential for complimentary measurements or even for replacing established orientation determination and imaging techniques.

Appendix A

Elastic Stiffness Matrices of Crystal Systems

Elastic stiffness matrices of different crystal systems [45]:

1. Cubic crystal

$$
(C_{ij}) = \begin{bmatrix}
c_{11} & c_{12} & c_{12} & 0 & 0 & 0 \\
c_{12} & c_{11} & c_{12} & 0 & 0 & 0 \\
c_{12} & c_{12} & c_{11} & 0 & 0 & 0 \\
0 & 0 & 0 & c_{44} & 0 & 0 \\
0 & 0 & 0 & 0 & c_{44} & 0 \\
0 & 0 & 0 & 0 & 0 & c_{44}
\end{bmatrix}
$$

2. Hexagonal crystal

$$
(C_{ij}) = \begin{bmatrix}
c_{11} & c_{12} & c_{13} & 0 & 0 & 0 \\
c_{12} & c_{11} & c_{13} & 0 & 0 & 0 \\
c_{13} & c_{13} & c_{33} & 0 & 0 & 0 \\
0 & 0 & 0 & c_{44} & 0 & 0 \\
0 & 0 & 0 & 0 & c_{44} & 0 \\
0 & 0 & 0 & 0 & 0 & 2(c_{11} - c_{12})
\end{bmatrix}
$$

3. Trigonal crystal (six constants)

$$(C_{ij}) = \begin{bmatrix} c_{11} & c_{12} & c_{13} & c_{14} & 0 & 0 \\ c_{12} & c_{11} & c_{13} & -c_{14} & 0 & 0 \\ c_{13} & c_{13} & c_{33} & 0 & 0 & 0 \\ c_{14} & -c_{14} & 0 & c_{44} & 0 & 0 \\ 0 & 0 & 0 & 0 & c_{44} & c_{14} \\ 0 & 0 & 0 & 0 & c_{14} & 2(c_{11}-c_{12}) \end{bmatrix}$$

4. Trigonal crystal (seven constants)

$$(C_{ij}) = \begin{bmatrix} c_{11} & c_{12} & c_{13} & c_{14} & c_{15} & 0 \\ c_{12} & c_{11} & c_{13} & -c_{14} & -c_{15} & 0 \\ c_{13} & c_{13} & c_{33} & 0 & 0 & 0 \\ c_{14} & -c_{14} & 0 & c_{44} & 0 & -c_{15} \\ c_{15} & -c_{15} & 0 & 0 & c_{44} & c_{14} \\ 0 & 0 & 0 & -c_{15} & c_{14} & 2(c_{11}-c_{12}) \end{bmatrix}$$

5. Tetragonal crystal (six constants)

$$(C_{ij}) = \begin{bmatrix} c_{11} & c_{12} & c_{13} & 0 & 0 & 0 \\ c_{12} & c_{11} & c_{13} & 0 & 0 & 0 \\ c_{13} & c_{13} & c_{33} & 0 & 0 & 0 \\ 0 & 0 & 0 & c_{44} & 0 & 0 \\ 0 & 0 & 0 & 0 & c_{44} & 0 \\ 0 & 0 & 0 & 0 & 0 & c_{66} \end{bmatrix}$$

6. Tetragonal crystal (seven constants)

$$(C_{ij}) = \begin{bmatrix} c_{11} & c_{12} & c_{13} & 0 & 0 & c_{16} \\ c_{12} & c_{11} & c_{13} & 0 & 0 & -c_{16} \\ c_{13} & c_{13} & c_{33} & 0 & 0 & 0 \\ 0 & 0 & 0 & c_{44} & 0 & 0 \\ 0 & 0 & 0 & 0 & c_{44} & 0 \\ c_{16} & -c_{16} & 0 & 0 & 0 & c_{66} \end{bmatrix}$$

7. Orthorhombic crystal

$$(C_{ij}) = \begin{bmatrix} c_{11} & c_{12} & c_{13} & 0 & 0 & 0 \\ c_{12} & c_{22} & c_{23} & 0 & 0 & 0 \\ c_{13} & c_{23} & c_{33} & 0 & 0 & 0 \\ 0 & 0 & 0 & c_{44} & 0 & 0 \\ 0 & 0 & 0 & 0 & c_{55} & 0 \\ 0 & 0 & 0 & 0 & 0 & c_{66} \end{bmatrix}$$

8. Monoclinic crystal

$$(C_{ij}) = \begin{bmatrix} c_{11} & c_{12} & c_{13} & 0 & 0 & c_{16} \\ c_{12} & c_{22} & c_{23} & 0 & 0 & c_{26} \\ c_{13} & c_{23} & c_{33} & 0 & 0 & c_{36} \\ 0 & 0 & 0 & c_{44} & c_{45} & 0 \\ 0 & 0 & 0 & c_{45} & c_{55} & 0 \\ c_{16} & c_{26} & c_{36} & 0 & 0 & c_{66} \end{bmatrix}$$

Appendix B

Elastic Constants of Crystals

Medium	Moduli (unit: GPa)											Density	Tem.	Ref.
	c_{11}	c_{12}	c_{13}	c_{14}	c_{22}	c_{23}	c_{33}	c_{44}	c_{55}	c_{66}		(gm/cm^3)	(K)	
Ni	247	153	-	-	-	-	-	122	-	-		8.912	293	[32]
Ni	261	151	-	-	-	-	-	131	-	-		8.912	4	[33]
Ni	251.6	154.4	-	-	-	-	-	122	-	-		8.912	298	[40]
Al	107.3	60.9	-	-	-	-	-	28.3	-	-		2.699	298	[33]
Al	108	62	-	-	-	-	-	28.3	-	-		2.698	293	[32]
Al	106.75	60.41	-	-	-	-	-	28.34	-	-		2.699	297	[39]

Si	165	64	-	-	-	-	79.2	-	2.328	293	[32]
Ti-β	97.7	82.7	-	-	-	-	37.5	-	4.581	298	[36]
Ti-α	163.6	92.3	67.92	-	185.2	47.05	-	4.429	1273	[37]

Table B.1: Elastic Constants of Crystals.

Appendix C

Rotation Matrix

The rotation matrix is defined as

$$
R = \begin{bmatrix}
x^2(1-cos\theta)+cos\theta & xy(1-cos\theta)-zsin\theta & xz(1-cos\theta)+ysin\theta \\
yx(1-cos\theta)+zsin\theta & y^2(1-cos\theta)+cos\theta & yz(1-cos\theta)-xsin\theta \\
zx(1-cos\theta)-ysin\theta & zy(1-cos\theta)+xsin\theta & z^2(1-cos\theta)+cos\theta
\end{bmatrix}
$$

where [x y z] is the rotation axis from (001) plane to the target plane, θ is the angle between the [001] and the target plane normal.

Appendix D

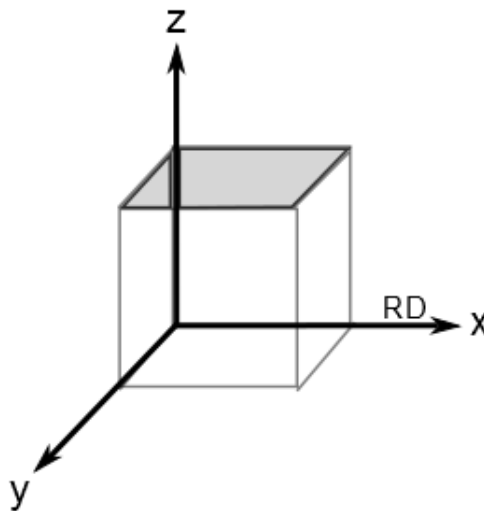# Definition of Primary Angles

Definition of primary angles γ, δ, κ, θ and α [34].

Figure D.1: The reference plane (in grey) and direction (RD).
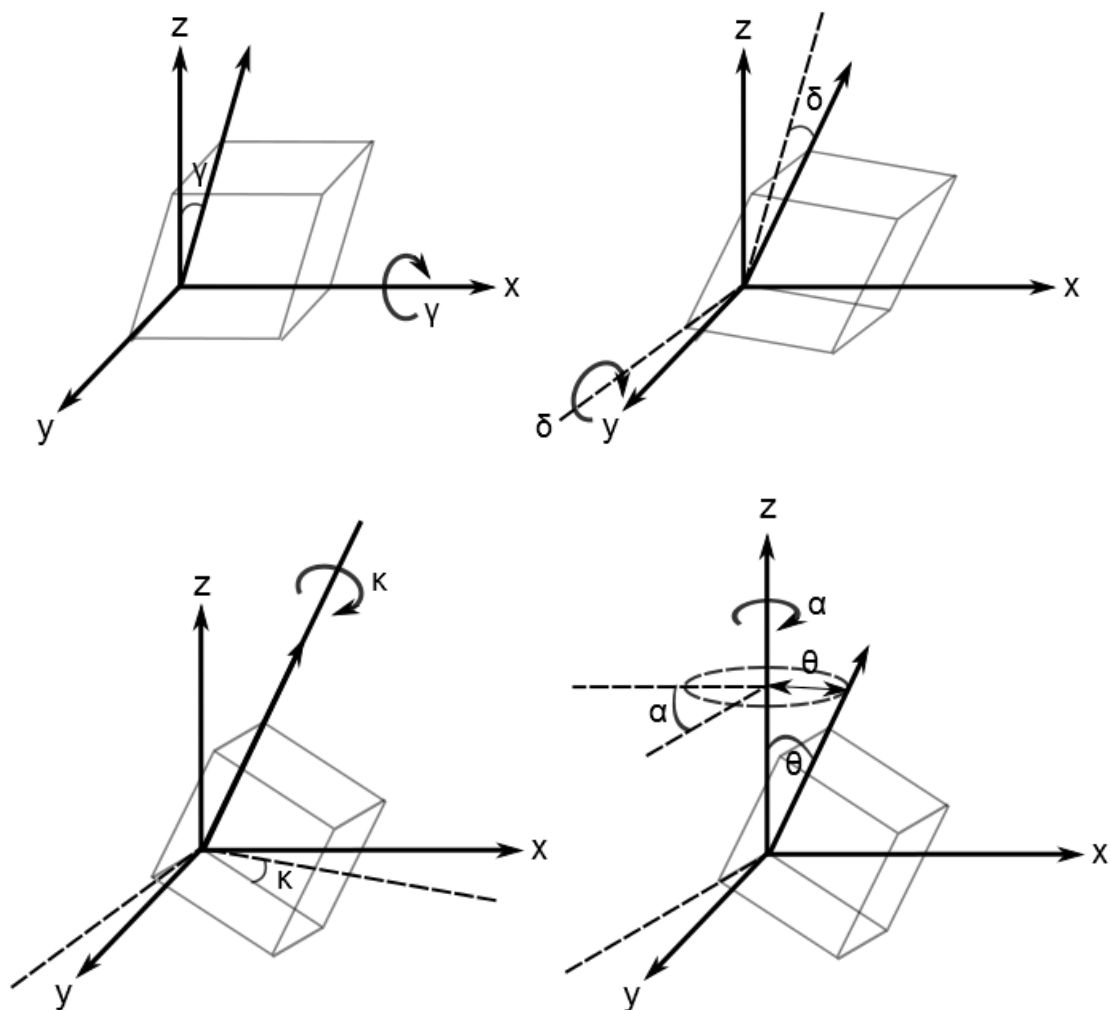
Figure D.2: Definition of γ, δ, κ, θ and α.

Appendix E

Definition of R-value

E.1 R-value Definitions

The table shows five R-value definitions [34].

Name	Formula
Single-angle cos (R-1cos)	$R = Minimum\ of\ 24\ single\ rotations$
Two-angle cos (REL or R-2cos)	$R = arccos(cos\phi cos\tau)$
Two-angle RMS (R-2RMS)	$R = \sqrt{(\phi^2 + \tau^2)}$
Three-angle cos (R-3cos)	$R = arccos(cos(\gamma_A - \gamma_B)cos(\delta_A - \delta_B)cos(\alpha_A - \alpha_B))$
Three-angle RMS (R-3RMS)	$R = \sqrt{(\gamma_A - \gamma_B)^2 + (\delta_A - \delta_B)^2 + (\alpha_A - \alpha_B)^2}$

Table E.1: Definitions of R-value.

E.2 Definition of ϕ and τ for R-value Calculations

The figure represents the rotation angle ϕ and τ visually [34].

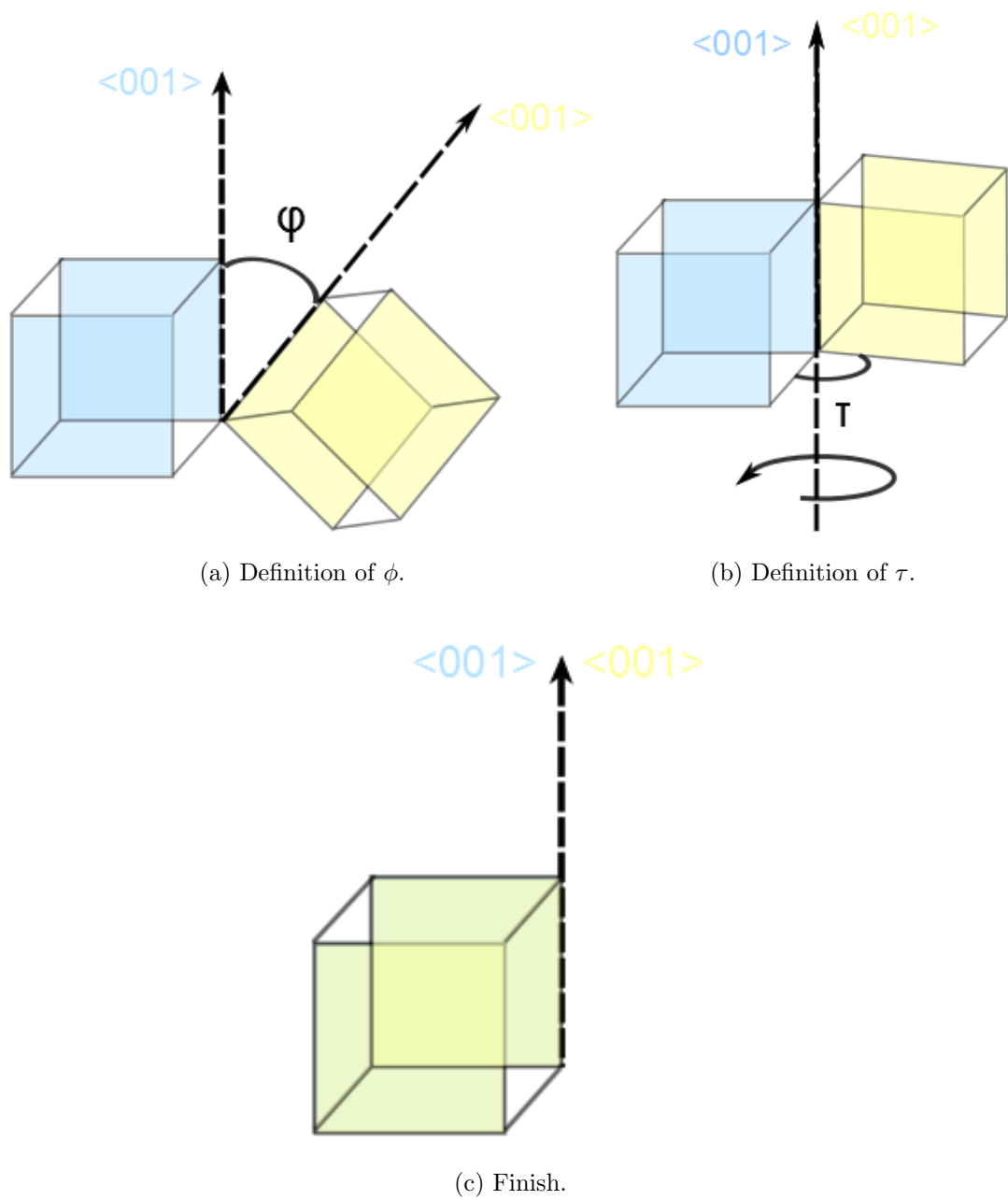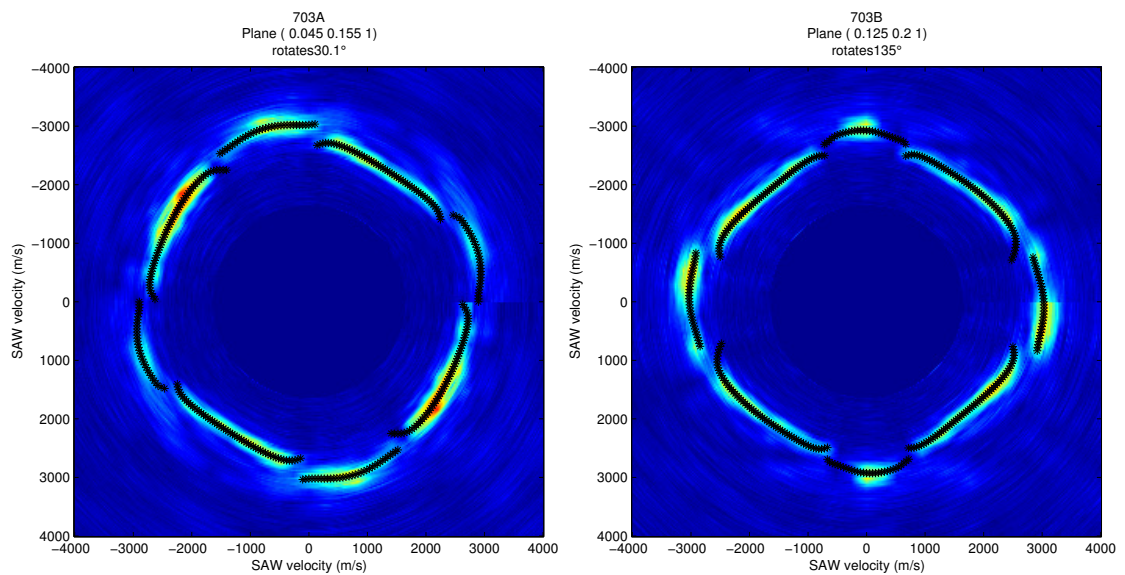(a) Definition of ϕ.

(b) Definition of τ.

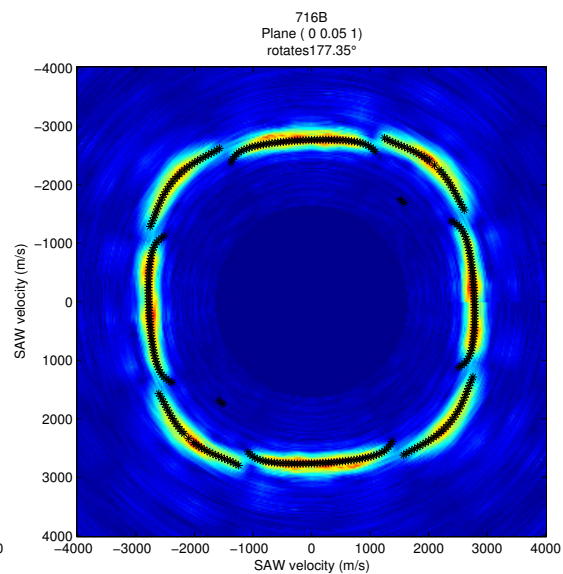(c) Finish.

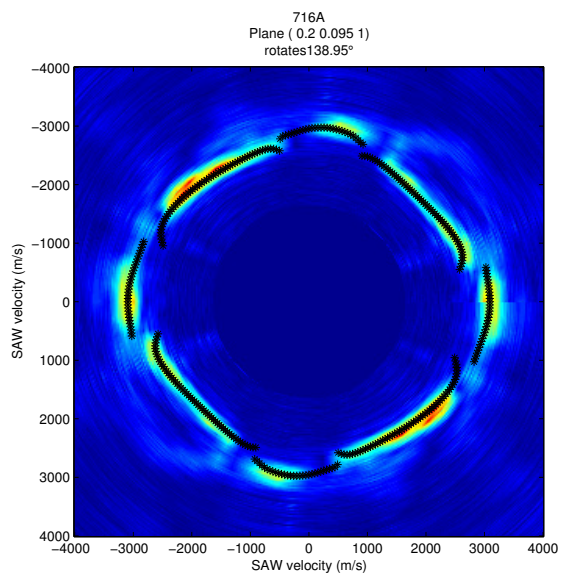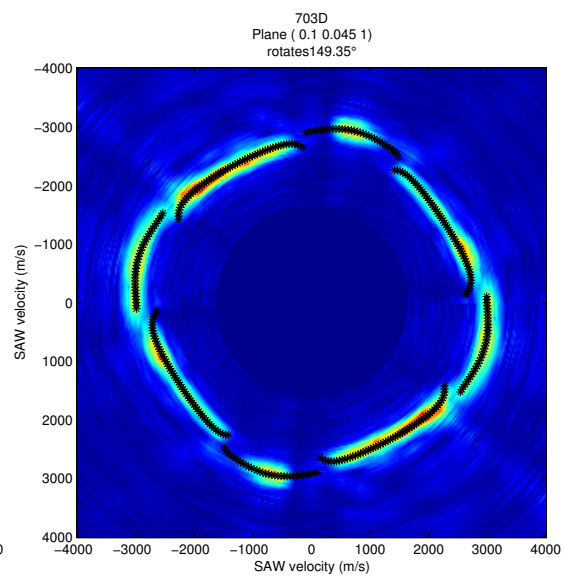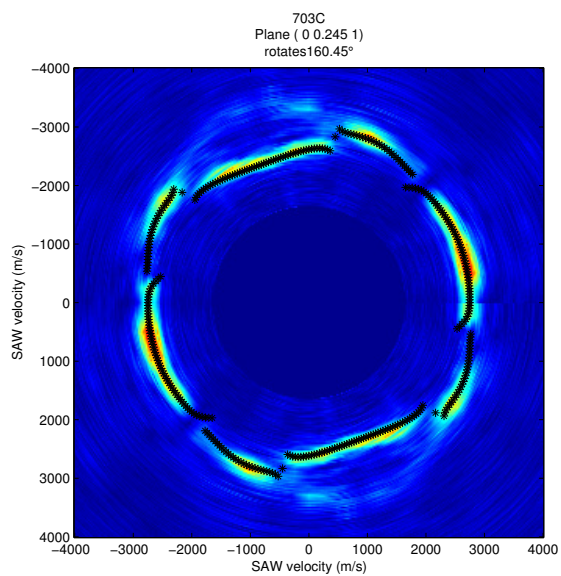Figure E.1: Definition of two angles of R-value.

Appendix F

Results of Overlap Function: 13 Nickel Samples

F.1   By Method I

703A
Plane (0.045 0.155 1)
rotates30.1°

703B
Plane (0.125 0.2 1)
rotates135°

703C
Plane (0 0.245 1)
rotates160.45°

703D
Plane (0.1 0.045 1)
rotates149.35°

716A
Plane (0.2 0.095 1)
rotates138.95°

716B
Plane (0 0.05 1)
rotates177.35°

716C
Plane (0.15 0.105 1)
rotates107.9°

716D
Plane (0.045 0.045 1)
rotates74.1°

721A
Plane (0.145 0 1)
rotates19.25°

721B
Plane (0.22 0 1)
rotates20.6°

zero
Plane (0.04 0.09 1)
rotates125.1°

twenty
Plane (0.28 0.1 1)
rotates17.95°

unknown
Plane (0.85 0.3 1)
rotates15.99°

F.2 By Method II

716A
Plane (0.35 0.05 1)
rotates139.7°

716B
Plane (0.1 0 1)
rotates87.96°

716C
Plane (0.3 0.2 1)
rotates103.35°

716D
Plane (0.05 0.1 1)
rotates75.46°

721A
Plane (0.2 0.15 1)
rotates111.84°

721B
Plane (0 0 1)
rotates26.52°

zero
Plane (0 0.2 1)
rotates124.06°

twenty
Plane (0.3 0.1 1)
rotates18.09°

unknown
Plane (0.85 0.3 1)
rotates15.99°

Appendix G

Laue back-reflection (LBR) Results of 12 Nickel Samples

Samples	γ	δ	κ
Sample 1	-0.3°	-0.5°	74.9°
Sample 2	10.4°	5.4°	16.6°
Sample 3	11.3°	-3.6°	51.1°
Sample 4	-0.6°	-1.8°	83.1°
Sample 5	-9.5°	3.0°	52.9°
Sample 6	10.6°	4.8°	68.7°
Sample 7	7.2°	-8.2°	25.4°
Sample 8	-13.3°	-4.7°	39.2°
Sample 9	-10.9°	-11.4°	18.2°
Sample 10	-9.7°	-9.8°	18.7°
Sample 11	-5.7°	0.5°	34.9°
Sample 12	-14.0°	1.7°	15.5°

Table G.1: LBR Results of 12 Nickel Samples.

Bibliography

[1] S. D. Sharples, *All-optical scanning acoustic microscope.* PhD thesis, Electrical and Electronics Engineering, May 2003.

[2] S. Tayabji and E. Lukanen, *Nondestructive testing of pavements and back-calculation of moduli: Third volume.* ASTM special technical publication, ASTM, 2000.

[3] L. Rayleigh, "On waves propagated along the plane surface of an elastic solid," *Proceedings of the London Mathematical Society*, vol. s1-17, no. 1, pp. 4–11, 1885.

[4] G. W. Farnell, *Physical Acoustics – Principles and Methods*, vol. VI, ch. 3, pp. 109–166. New York and London: Academic Press, 1970.

[5] V. R. Velasco and F. Garcia-Moliner, "Theory of surface waves in anisotropic cubic crystals," *Solid State Physics*.

[6] A. E. H. Love, *Some problems of geodynamics.* Cambridge University Press, 1911.

[7] W. Soboyejo, *Mechanical properties of engineered materials.* Mechanical engineering, Marcel Dekker, 2003.

[8] D. Morgan, "History of saw devices," in *Frequency Control Symposium, 1998. Proceedings of the 1998 IEEE International*, pp. 439 –460, may 1998.

[9] J. Monchalin, C. Néron, J. Bussière, I. M. I. (Canada), and I. des matériaux industriels (Canada), *Laser-ultrasonics: from the laboratory to the shop floor.* IMI (Series), Industrial Materials Institute, National Research Council of Canada, 1994.

[10] S. J. Davies, C. Edwards, G. S. Taylor, and S. B. Palmer, "Laser-generated ultrasound: its properties, mechanisms and multifarious applications," *Journal of Physics D: Applied Physics*, vol. 26, no. 3, pp. 329–348, 1993.

[11] R. G. White and D. C. Emmony, "Active feedback stabilisation of a michelson interferometer using a flexure element," *Journal of Physics E: Scientific Instruments*, vol. 18, no. 8, p. 685, 1985.

[12] H. Sontag and A. Tam, "Optical detection of nanosecond acoustic pulses," *Ultrasonics, Ferroelectrics and Frequency Control, IEEE Transactions on*, vol. 33, pp. 500–506, sep 1986.

[13] Royer, D., Noroy, M.-H., and Fink, M., "Optical generation and detection of elastic waves in solids," *J. Phys. IV France*, vol. 04, no. C7, pp. C7–673–C7–684, 1994.

[14] A. S. Murfin, R. A. J. Soden, D. Hatrick, and R. J. Dewhurst, "Laser-ultrasound detection systems: a comparative study with rayleigh waves," *Measurement Science and Technology*, vol. 11, no. 8, p. 1208, 2000.

[15] R. J. Dewhurst and Q. Shan, "Optical remote measurement of ultrasound," *Measurement Science and Technology*, vol. 10, no. 11, p. R139, 1999.

[16] P. Atkins and L. Jones, *Chemical Principles: The Quest for Insight.* W H Freeman & Co, 2007.

[17] A. Greninger, "A back-reflection laue method for determining crystal orientation," *dans Zeitschrift f. Kristallographie.*

[18] K. Clay, K. Mingard, R. Morrell, and P. Quested, "R value measurement issues for grain boundaries in nickel single crystal casting," *Materials Science and Technology*, vol. 26, no. 7, pp. 781–786, 2010.

[19] O. Engler and V. Randle, *Introduction to Texture Analysis: Macrotexture, Microtexture and Orientation Mapping*. CRC Press, 2010.

[20] J. B. Burns, A. R. Hanson, and E. M. Riseman, "Extracting straight lines," *IEEE Trans. Pattern Anal. Mach. Intell.*

[21] N. C. Krieger Lassen, D. Juul Jensen, and K. Conradsen, "Image processing procedures for analysis of electron back scattering patterns," *Scanning Microscopy*.

[22] V. Randle, *Microtexture Determination and Its Applications*. London, UK: Maney Publishing, 2003.

[23] S. D. Sharples, M. Clark, and M. G. Somekh, "Spatially resolved acoustic spectroscopy for fast noncontact imaging of material microstructure," *Optics Express*, vol. 14, no. 22, pp. 10435–10440, 2006.

[24] S. D. Sharples, M. Clark, and M. G. Somekh, "Fast noncontact imaging of material microstructure using local surface acoustic wave velocity mapping," in *Ultrasonics Symposium, 2005 IEEE*, pp. 886–889, IEEE, 2005.

[25] W. Li, S. D. Sharples, M. Clark, and M. G. Somekh, "Frequency spectrum spatially resolved acoustic spectroscopy for microstructure imaging," in *Journal of Physics: Conference Series*, vol. 278, IOP, 2011.

[26] I. J. Collison, *Measurement of Material Nonlinearity using Laser Ultrasound*. PhD thesis, Electrical and Electronics Engineering, July 2008.

[27] W. Li, S. D. Sharples, M. Clark, and M. G. Somekh, "Frequency spectrum spatially resolved acoustic spectroscopy for microstructure imaging," in *2009 IEEE International Ultrasonics Symposium*, pp. 791 – 794, IEEE, 2009.

[28] S. D. Sharples, W. Li, M. Clark, and M. G. Somekh, "Microstructure imaging using frequency spectrum spatially resolved acoustic spectroscopy (f-sras)," in *The Review of Progress in Quantitative Nondestructive Evaluation (QNDE)*, pp. 279–286, American Institute of Physics, 2009.

[29] E. A. Ash and A. A. Oliner, *Acoustic surface waves / edited by A. A. Oliner ; with contributions by E. A. Ash ... [et al.].* Springer-Verlag, Berlin ; New York :, 1978.

[30] J. F. Nye, *Physical Properties of Crystals: Their Representation by Tensors and Matrices.* Oxford University Press, USA, 1985.

[31] I. A. Viktorov, *Rayleigh and Lamb Waves: Physical Theory and Applications.* New York: Plenum Press, 1967.

[32] R. Hearmon, "The elastic constants of anisotropic materials — ii," *Advances in Physics*, vol. 5, no. 19, pp. 323–382, 1956.

[33] O. L. Anderson, *Physical Acoustics – Principles and Methods*, vol. IIIB, ch. 2, p. 79. New York and London: Academic Press, 1965.

[34] K. Clay, J. Jackson, P. Quested, and R. Morrell, "Improving single-crystal orientation determination for advanced nickel-based alloys," in *Measurement Good Practice Guide*, 112, (Teddington, UK), National Physical Laboratory, 2009.

[35] V. A. Joshi, *Titanium Alloys: An Atlas of Structures and Fracture Features.* CRC Press, 2006.

[36] H. Ledbetter, H. Ogi, S. Kai, S. Kim, and M. Hirao, "Elastic constants of body-centered-cubic titanium monocrystals," *Journal of Applied Physics*, vol. 95, pp. 4642 –4644, may 2004.

[37] H. Ogi, S. Kai, H. Ledbetter, R. Tarumi, M. Hirao, and K. Takashima, "Titanium's high-temperature elastic constants through the hcp-bcc phase transformation," *Acta Materialia*, vol. 52, no. 7, pp. 2075 – 2080, 2004.

[38] *The Photo-Mask Guide.* Meridian Centre, King Street, Oldham, UK, 2010.

[39] H. M. Ledbetter and S. D. Kim, "Monocrystal elastic constants and deprived properties of the cubic and the hexagonal elements," *Handbook of Elastic Properties of Solids, Fluids, and Gases, Four-Volume Set*, vol. 2, pp. 97–106, January 2001.

[40] K. Salama and G. Alers, "The third-order elastic moduli of pure nickel and some dilute copper-nickel alloys," in *1968 IEEE Ultrasonic Symposium*, IEEE, 1968.

[41] J. E. Sinclair, "Epicentre solutions for point multipole sources in an elastic half-space," *Journal of Physics D: Applied Physics*, vol. 12, no. 8, p. 1309, 1979.

[42] J. J. Dike and T. M. Sanderson, "Simulations of surface waves generated using laser ultrasonics," in *Review of Progress in Quantitative Nondestructive Evaluation*, (Snowbird, USA), US Department of Energy, 1998.

[43] J. B. Spicer, *Laser Ultrasonics in Finite Structures: Comprehensive Modelling with Supporting Experiment.* PhD thesis, THE JOHNS HOPKINS UNIVERSITY., 1991.

[44] T. Sanderson, *Thermoelastic modeling of laser generated ultrasound for non-destructive materials testing.* PhD thesis, Georgia Institute of Technology, 1997.

[45] L. Wheeler and C. Y. Guo, "Symmetry analysis of extreme areal poissons ratio in anisotropic crystals," *Journal of Mechanics of Materials and Structures*, vol. 2, no. 8, pp. 1471–1499, 2007.